Master Thesis

Synthesis and Characterization of Nanostructured Metal Oxides and Metal-Organic Frameworks

Author
H.A.A. Al-Kutubi

Supervisor
Dr. Liza Rassaei

February 2015

Organic Materials and Interfaces
Chemical Engineering Department

Abstract

The field of metal oxides is as large as it is fascinating. Whereas the amount of metal oxides in the world are finite, their potential applications are seemingly endless. This thesis aims to explore the synthesis of metal oxides using two different approaches: Electrochemical deposition of a metal oxide as a method for the indirect electrosynthesis of a metal-organic frameworkand thermal oxidation of templated novel metal oxide structures.

Metal-organic frameworks (MOFs) are a versatile class of porous materials. A high surface area, remarkable stability and seemingly endless tunability has led to various synthesis methods as well as a vast number of applications. Chapter 1 presents a literature review into the electrosynthesis of MOFs through direct as well as indirect means. It provides an introduction into the field of MOFs and an explanation of the most important concepts.

Chapter 2 discusses the indirect electrosynthesis of the well-known ZIF-8. By using a new method that relies on zinc oxide as a nucleation site as well as a reactant source, the formation of a nanostructured hybrid material was achieved in a fast and simple manner. First, the electrodeposition of zinc oxide nanorods on FTO glass was optimized in order to obtain a well-defined, homogenous nanorod arrays. A thin layer of linker was then deposited onto these rods and heated. The result is the formation of a ZIF-8 thin film. The effect of synthesis conditions were investigated for both zinc oxide synthesis as well as thin film formation using XRD and SEM.

Finally, chapter 3 discusses the use of polymers of intrinsic microporosity (PIMs) as templating materials for the synthesis of praseodymium and cerium oxides through thermal oxidation. These metal oxides were formed using two different PIMs (PIM-EA-TB and PIM-1). Each PIM yields a pure oxide with a novel, unique porous structure. The composition, oxidation state and the electrochemical properties of these oxides were studied using CV, SEM, XPS and Raman spectroscopy.

Acknowledgement

First and foremost, I would like to thank the universe, without whose existence none of this would be possible. Almost as vast as the universe is my gratitude to my family and friends. Thank you for always being there for me. I cannot thank you enough.

I would also like to thank my supervisor for giving me such great opportunities. Your constant encouragement and positivity have inspired me to see the world in a different way and I will never forget what I have learned from you.

Thank you to Professor Ernst Sudhölter for advice in both science and life.

From Catalysis Engineering, thank you Professor Jorge Gascon for your knowledge on MOFs and thank you Alla Dikhtiarenko for your help with understanding XRD.

I would like to thank Professor Frank Marken for his valuable insight and his group for making me feel welcome in Bath.

Thank you Hamid and Duco for the SEM images and your insight into all things SEM and non-SEM.

Finally, I would like to thank my friends and colleagues for their help, their wisdom and above all, their company.

Table of Contents

List of Figures

List of Tables

List of Abbreviations

MOFs	Metal-organic Frameworks
ZnO	Zinc Oxide
PIM	Polymer of intrinsic microporosity
H_3BTC/BTC	Trimesic acid
Hmin	2-Methyl imidazole
H_2BDC/BDC	Terephthalic acid
MTBS	Methyltributylammonium methylsulfate
TBATFB	Tetrabutylammonium tetrafluoroborate
HMT	Hexamethylenetetramine
DMF	*N,N*-Dimethylformamide
DEF	*N*,*N*-Diethylformamide
NMP	1-Methyl-2-pyrrolidone
BMIM	1-butyl-3-methylimidazole
FTO	Fluorine-doped tin oxide glass
ITO	Indium-doped tin oxide glass
Et_3NH^+	Triethylammonium
Et_3N	Triethylamine
$TBAPF_6$	Tetrabutylammonium hexafluorophosphate
BTDA	Benzophenone-3,3',4,4'-tetracarboxylic dianhydride
$BPTC^{4-}$	Benzophenone-3,3',4,4'-tetracarboxylate
XRD	X-ray diffraction
SEM	Scanning electron microscopy
FE-SEM	Field emission scanning electron microscopy
XPS	X-ray photoelectron spectroscopy
SCE	Saturated calomel electrode

1 Electrosynthesis of Metal Organic Frameworks: Challenges and Opportunities

Accepted for publication in ChemElectroChem.

Hanan Al-Kutubi, Jorge Gascon, Ernst Sudhölter, Liza Rassaei,

DOI: 10.1002/celc.201402429

1.1 Introduction

Metal-organic frameworks (MOFs) as crystalline, porous solid materials are formed *via* coordination bonds between organic linkers and metal ions or clusters. The chemical moieties within the framework can be spatially controlled *via* this bottom-up synthesis approach [1]. These frameworks stand out through their surprisingly high porosity [2] and fascinating versatility [3]. MOFs, or more widely speaking, coordination polymers are known from the late 1950s[4] and early 1960s [5-9], although it was not until the end of the last century when the field was re-launched thanks to the efforts, among others, of Robson and co-workers [10, 11], Kitagawa *et al*. [12, 13], Yaghi and coworkers [14], Lee and Moore [15], and Férey *et al*. [16]. Since then, MOFs keep breaking surface area records, with recently NU-110E surpassing 7000 m^2/g [17].

The microporous channels of MOFs can be tuned *via* the proper selection of linkers and are typically smaller than 2 nm in diameter. Tuning the size and affinity of these pores allows for the formation of selective molecular sieves that allow certain molecules to pass, while keeping others out [18, 19]. Combined in some cases with a surprising stability [20, 21], MOFs are mostly viewed as very promising materials in the areas of catalysis [22, 23], electrocatalysis [24], molecular separation [25], and storage [26]. Furthermore, by choice or design of a specific metal or a functionalized linker, one can add new properties to the framework for a variety of applications such as the sequestration of CO_2 or ion exchange [27-30]. The addition of light harvesting linkers results in the formation of photoactive MOFs [31-33]. Incorporating bio-based linkers yields bio-mimicking MOFs [34] and addition of magnetic metals or linkers leads to magnetic MOFs [35, 36]. Even their traditionally electrically insulating nature can be altered by the use of conductive linkers to form conductive MOFs [37, 38]. Incorporation of guest molecules into MOF pores can increase catalytic activity and storage capacity [39-41]. Finally, post-synthetic metalation or modification allows for the alteration and enhancement of many framework properties [1, 42, 43]. Such versatility has led to a growing increase of MOF research in the areas of catalysis [23, 44, 45], sensing [46-48], light harvesting, photocatalysis [31, 49], solar cells, [50] biomedicine [51, 52], fuel cells [53], electrochemistry [54-56], and many more.

Ahn *et al.* have recently summarized the common methods for the synthesis of MOFs [57], while Gascon *et al.* discussed the degree of rational design during MOF synthesis [58]. The most conventional method used to synthesize the first MOFs, is the hydrothermal method in which linker, metal salt and optional templating agents are dissolved in an organic solvent or in water and placed in an autoclave. This autoclave is then heated to above the boiling point of the organic solvent under elevated pressure for a certain number of hours and even days, allowing the formation of the desired MOF. Solvothermal syntheses are carried out at lower temperatures and atmospheric pressure, allowing i.e. easy diffusion controlled synthesis with promising applications in crystal engineering [59]. Other methods include the microwave-assisted [60], mechanochemical [61], liquid-phase epitaxy [62], sonochemical [63], and recently electrochemical methods. The electrochemical method holds several advantages, such as shorter synthesis times and milder synthesis conditions [64]. They also provide the possibility to influence the reaction directly in real time, offering both more control and the ability to perform the synthesis in a continuous fashion [65]. Furthermore, the localized nature of electrochemical methods allows the formation of directed thin films without the need to pre-treat the surface as is usually the case [66]. The mild temperatures used during synthesis also reduce the effects of thermally induced film cracking, which is often a problem in solvothermal methods [67].

Although various synthesis methods (mentioned above) have been developed for MOFs [57, 66, 68-70], electrosynthesis of MOFs is still a niche. Most current applications of MOFs rely on the use of bulk solid materials prepared following one of the other conventional methods. However, expanding the use of MOFs either into other applications such as membranes and sensors, or their integration with electronic devices requires thin films of these materials be prepared on a solid substrate [71]. In this regard, this review aims to summarize and critically assess the research on the electrosynthesis of MOFs and to provide a full picture of the developments within this field. The various ways electrochemistry has contributed to the synthesis of MOFs are explained and their strengths and shortcomings are discussed while an outlook for future research is provided.

1.2 The state of the art electrosynthesis of MOFs

1.2.1 Direct electrosynthesis of MOFs

Direct electrosynthesis relies on the use of electrochemistry to directly synthesise a metal-organic framework. Unlike indirect methods, where electrochemistry is only a step in an overall synthesis procedure, direct electrosynthesis allows direct control of synthesis rate by electrochemical means.

1.2.1.1 Anodic dissolution

Pioneered and patented by BASF in 2005, anodic dissolution is the most well-known electrosynthesis method [72]. This method employs a metal electrode as a source of metal ions. The electrode is placed in the solution of the linker, often also containing an electrolyte. Upon applying an appropriate voltage or current, the metal dissolves and the metal ions required for the MOF formation are released near the electrode surface (in the double layer) (See Figure **1.2**A). The metal ions then immediately react with the linkers present in the solution and the MOF is formed close to the electrode surface. Thus, unlike the other synthesis methods, the metal ion is not supplied by a salt precursor but by the oxidation of the electrode. Therefore, the variation in kinetics of MOF formation related to the source of metal precursor (for example $Cu(NO_3)_2$ *vs.* $Cu(OAC)_2$) can be avoided [73, 74]. Another advantage of this method is the possibility to control the oxidation state of the metal by simply applying either the appropriate voltage (amperometry mode) or current (potentiometry mode) to the electrode. Both modes can be employed continuously or in the form of wave or square functions.

Anodic dissolution is normally carried out in a two electrode set-up in absence of a reference electrode. Thus, the cell geometry and maintenance of a constant distance between the electrodes are crucial to ensure uniform current distribution during electrosynthesis [75, 76]. The use of protic solvents ensures evolution of hydrogen and not the reduction of metal ions at the counter electrode. Thus, it is recommended to use a counter electrode with a suitable overpotential for hydrogen evolution or to add a sacrificial compound to be reduced instead of the metal ions [72].

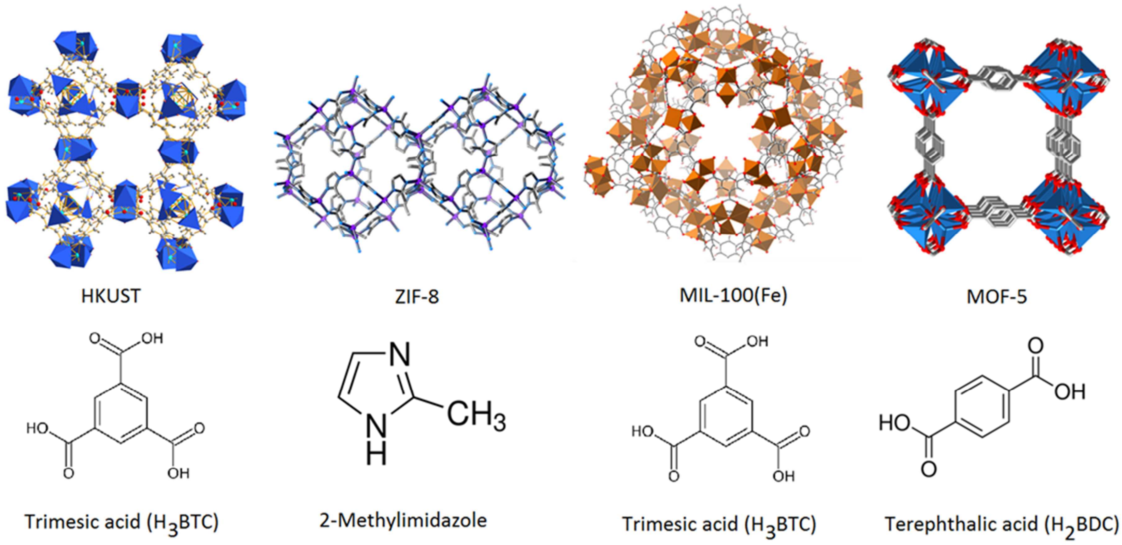

Figure 1.1. Schematic representation of several MOFs mentioned in this chapter and their corresponding linkers.

The most often synthesized MOF using this method is $Cu_3(BTC)_2$, also known as HKUST-1. First published in 1999, this MOF consists of copper centres, connected *via* trimesic acid (H_3BTC) linkers and possesses a paddle-wheel structure [77]. Its chemical stability, ease of synthesis and versatility have made $Cu_3(BTC)_2$ one of the most popular MOFs. By applying an oxidation potential or current, the copper electrode is oxidized to Cu^{2+} ions in the vicinity of the electrode. These ions then react with the BTC linker to form HKUST-1. By controlling the current density or the applied voltage, the amount of Cu^{2+} concentration in the electrode double layer can be controlled. Electrosynthesis parameters such as applied potential, current density, distance between the electrodes, pulse time (in case of square functions), synthesis time, solvent, linker and electrolyte concentrations all play important roles in the quality of resulting MOF.

Mueller *et al.* investigated the properties of HKUST-1 prepared *via* anodic dissolution [78]. They used two copper plates in a solution of BTC in methanol and applied a voltage of 12–19 V between them (a current of 1.3 A) for 150 min. The properties of the obtained MOF was compared with those obtained *via* solvothermal and hydrothermal methods [77, 79, 80]. The electrosynthesized MOF was shown to possess a much larger surface area of 1820 m^2g^{-1} *vs.* 917 m^2g^{-1} for the other samples. The lower surface area of samples synthesized solvothermally was attributed to the presence of nitrates moieties (from the precursor) which block the pores.

Hartmann *et al.* studied the effect of solvent and synthesis procedure (solvothermal, reflux, and anodic dissolution) on separation properties of HKUST-1 for isobutene and isobutane [81]. They synthesized the samples by applying a voltage of 15 V and a current of 0.05 mA between two copper electrodes for 2 hours in a solution of BTC and methyltributylammonium methylsulfate (MTBS) as an electrolyte in either ethanol or ethanol/water (50/50 v/v) mixtures. Synthesis in ethanol resulted in HKUST-1 with higher specific surface area compared to those of ethanol/water mixtures. Electrosynthesized HKUST-1 had a smaller pore volume and surface area, attributed to the presence of conducting salt in its pore structure.

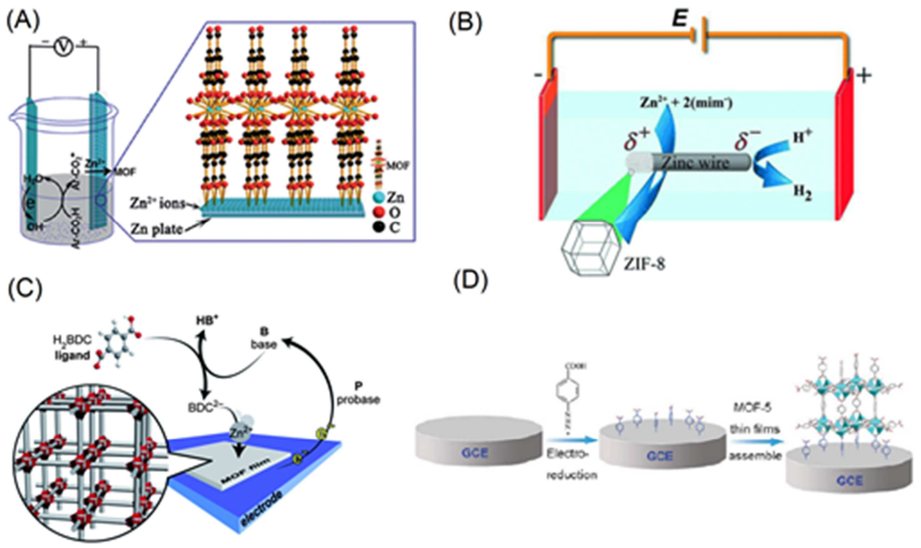

Figure 1.2. Schematic diagram of selected methods for electrosynthesis of MOFs. (A) anodic dissolution (reprinted from [60] with permission from the Royal Society of Chemistry), (B) indirect bipolar electrodeposition (reprinted from [73] with permission from Wiley (C) probase electroreduction (reprinted from [76] with permission from the Royal Society of Chemistry), and (D) anchoring a linker (reprinted from [79] with permission from the Royal Society of Chemistry).

Kulandainathan *et al.* studied the effect of supporting electrolyte concentration and current density on the particle size of HKUST-1 for application as catalyst for the reduction of *p*-nitrophenol to *p*-aminophenol by $NaBH_4$ [82]. Electrosynthesis was performed by applying a constant voltage of 10-20 V between the two copper electrodes (the current was varied to keep the voltage constant) for 15 min in a methanol solution containing BTC as a linker and tetrabutylammonium tetrafluoroborate (TBATFB). The effects of electrosynthesis conditions such as concentration of supporting electrolyte, applied voltage, and reaction time were investigated with respect to yield, crystallinity, surface area, and process control. While electrosynthesis yield depended mainly on the synthesis time, an increase in applied voltage and concentration of supporting electrolyte resulted in a higher yield. However, an applied potential of 15 V and TBATFB concentration above 0.02 M resulted in agglomeration and collapse of the crystal cubic shape, indicating that a high anodic dissolution rate may have an adverse effect. The electrosynthesis at ambient temperature resulted in a pure HKUST-1 without any trace of copper oxide impurities, often known to occur at high synthesis temperature [73] or conducting salt in the pores of the structure. The surface area of HKUST-1 in this work was higher (1498 m^2g^{-1}) than the value obtained by Hartmann *et al.* (1309 m^2g^{-1} for ethanol as solvent) for electrosynthesis [81].

De Vos *et al.* also investigated the effect of electrosynthesis conditions on the formation of HKUST-1 dense films [64]. They used two copper electrodes at a distance of 1 cm in a solution of BTC and MTBS in various mixtures of ethanol and water at the temperature of 55 ° C. The effects of applied potential, synthesis time, and water-to-ethanol ratio on the thickness and density of the resulting HKUST-1 were studied. For example, by varying the synthesis conditions, the crystal size was tuned over a wide range (2-50 µm). Increasing the applied potential between the two electrodes from 2.5 V to 25 V resulted in the formation of smaller crystals, in agreement with nucleation theory. A higher potential resulted in a higher dissolution rate; thus, a higher concentration of metal ions near the electrode surface and accordingly, a higher nucleation rate and smaller crystals. Increasing the amount of water resulted in larger crystals, as water lowers the nucleation rate by hydrating the metal ions in solution [83]. Longer synthesis times resulted in more dense and intergrown films.

The advantage of formation of a dense film without piling up the crystals together with relatively much shorter synthesis times and milder conditions allows the integration of MOFs into delicate electronics. For example, HKUST-1 was grown on copper electrochemically deposited on a quartz microbalance to measure the humidity by adsorption of water in the metal-organic framework[64]. More recently, electrochemically synthesized HKUST-1 allowed the preparation of a micro-separator[84]. The solution conductivity (due to the presence of the electrolyte) influenced the density of HKUST-1 on the mesh. A higher solution conductivity results in a higher dissolution rate, and subsequent damage to the mesh structure. This results in poor adhesion of the crystals, whereas without a conducting salt, a more controlled synthesis was obtained. The ratio of ethanol to water was also found to have a profound effect on crystal morphology (See Figure **1.3**A-D). For water contents between 10 to 35%, the average crystal size was shown to increase from 2 to 11 µm in 30 min, allowing the fine tuning of crystal size. A water content of 50% resulted in the detachment of crystals, whereas a higher water content caused the formation of a non-porous structure (Figure **1.3**E-F).

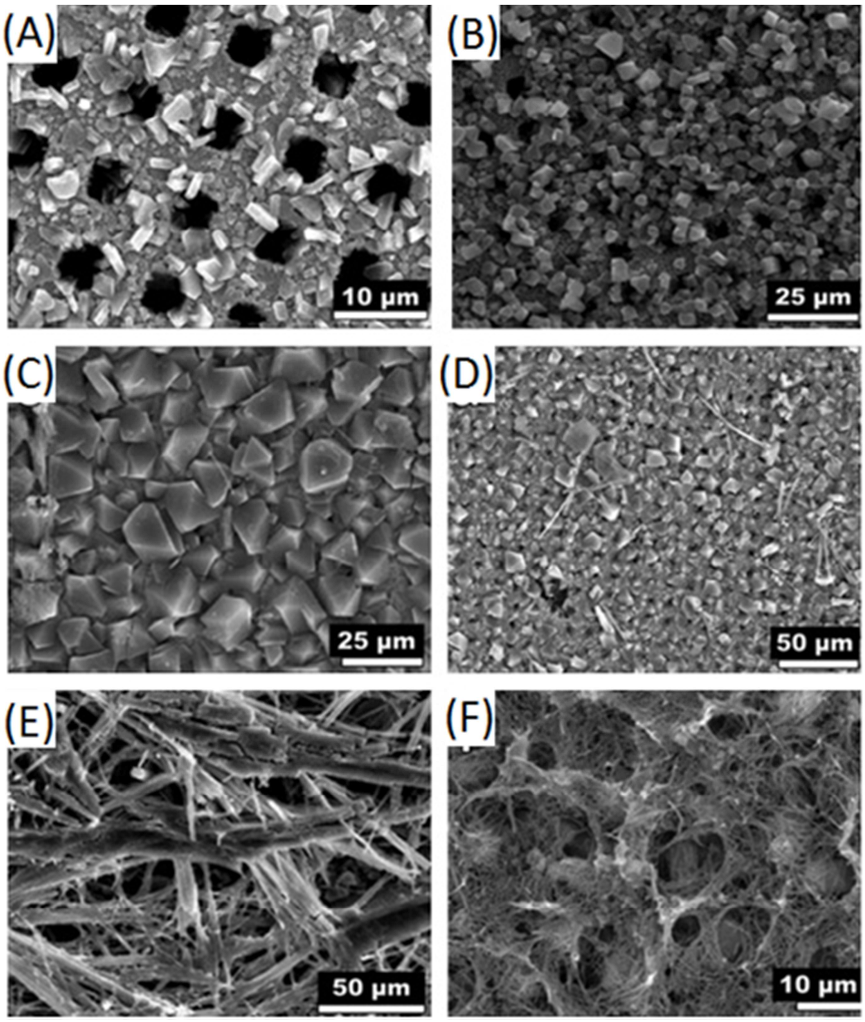

Figure 1.3. SEM images showing the effect of variation in solvent content (water-ethanol ratio) on morphology of HKUST-1 on a copper mesh. (A) 10, (B) 25, (C) 35 (D) 50 and (E-F) higher wt% water (Potential 2.7 V, 20-30 min). (Reprinted from 54 with permission from Elsevier)

Even though it was not confirmed, the structure was assumed to show similarities with the catena-triaque-mu-(1,3.5-benzene-tricarboxylate)-copper(II) [85] reported by Gascon *et al.* when they attempted to synthesize HKUST-1 in only water [86]. This structure consists of BTC bound *via* two carboxylic acid groups (instead of three) to copper centres due to the incomplete de-protonation of the linker and the low local pH caused by hydrogen evolution. The frequency of the applied potential was found not to have any impact.

Table 1.1. Comparison of anodic dissolution electrosynthesis conditions for different MOFs

MOF[a]	Applied Potential (V)	Applied Current	Solvent/ Electrolyte	Advantages/ Disadvantages
HKUST-1 [78]	12-19	1.3 A (surface area not mentioned)	Methanol/ Not mentioned	No nitrate moieties in pores
HKUST-1 [81]	15	0.05 mA	50-50 v/v% Water-Ethanol/ MBTS	Conducting salt in pores
HKUST-1 [82]	10-20	Not mentioned	Methanol/ TBATFB	High yield, no copper oxide
HKUST-1 [64]	2-25	Not mentioned	Water-Ethanol/ MTBS	Thin film formation, control of crystals
HKUST-1 [87]	0-5	Not mentioned	Water-Ethanol/ None	Thin film formation, control crystal size
HKUST-1 [65]	Not mentioned	10	Water-Ethanol/ MTBS	Thin film formation
MIL-100(Fe) [88]	Not mentioned	2-20		
Li-doped MIL-100 (Fe) [48]	Not mentioned	38	Methanol/ MTBS	Able to dope MOF
ZIF-8 [65]	Not mentioned	10	DMF, Water Water-Acetonitril, Methanol, Water-methanol/ MTBS,KCl	Able to obtain MOF at 0 °C
ZIF-8 [89]	5-7 V	Not mentioned	Water/ $NaSO_4$	Able to form thin film selectively on one side
MIL-100 (Al) [65]	Not mentioned	10	25-75 v/v% Water-Ethanol/ None	MOF formed, but not very crystalline and in low yield
MIL-53 (Al) [65]	Not mentioned	2-20	90-10 v/v% Water-DMF/ MBTS,KCl	Phase pure MOF, pore opening occurs. Not very crystalline
NH2-MIL-53 (Al) [65]	Not mentioned	2-20	Water-DMF/ KCl	No breathing, degree of openness can be controlled
MOF-5 [90]	Not mentioned	2.5	DMF/ BMIN bromine	Novel flowerlike morphology created
MOF-5 [91]	0.5-2 V	Not mentioned	Water/ NH_4F	Possible to control morphology. Zinc oxide formed as well
Gd-BTC [92] Tb-BTC [92] Tb/Gd-BTC [92] ZnO(Tb)-BTC [92]	Not mentioned	1	50-50 v/v% Water-Ethanol/ MTBS	Possible to grow luminescent MOF thin films

Gascon *et al.* investigated the effect of solvent, electrolyte, voltage–current density, and temperature on the electrosynthesis of HKUST-1, ZIF-8, MIL-100(Al), MIL-53(Al), and NH$_2$-MIL-53(Al) [65]. In general, an increase in temperature led to a small variation in surface area but similar yields were obtained in all cases. Alteration of water-ethanol-ratios had similar effect as reported by Denayer *et al.* for the formation of a dense film of HKUST-1 at high water content [87]. However, here, the effect was explained by the intrinsically lower solubility and lower degree of de-protonation of the linker in water as compared to ethanol. Although the magnitude of the applied current did not influence the crystal size, it affected the rate of reaction. Contrary to the results obtained by Denayer *et al.*[87] the application of square wave current influenced the crystal formation, leading to a higher deposition rate. Finally, a higher conductivity by addition of an electrolyte and thus, a lower ohmic drop resulted in a higher yield and production rate of MOFs.

ZIF-8 is well-known for its remarkable stability, even when boiling in alkaline solution for 24 hours [93] and ease of synthesis under ambient conditions in both organic solvents as well as in water [94, 95]. However, the formation of ZIF-8 thin films is difficult and often require a seed layer or lengthy crystal growth under elevated temperatures [96-98]. The same applies for electrosynthesis of ZIF-8 particles, as they were mainly formed in solution, with almost none bound to the electrode. This was attributed to the crystallisation kinetics, the need for an incubation time before nucleation and the diffusion of metal ion from the surface [99]. Gascon *et al.*, studied the effect of temperature and the choice of solvent for electrosynthesis of ZIF-8 [65]. Surprisingly, ZIF-8 crystals were obtained at temperatures as low as 0 °C with an even higher production rate. The high solubility of the linker (2-methylimidazole) also allows the use of a variety of solvents and supporting electrolytes (which have different conductivities). Synthesis in water yields less crystalline products and requires a larger excess of linker compared to other solvents [100, 101]. This results in doubts as to whether the effect of solvent and conductivity can be sufficiently separated.

Gascon *et al.* also investigated the effect of electrosynthesis conditions on three MIL materials [65]. Named after the Materials Institute Lavoisier, the selected MILs consist of carboxylate linkers and aluminium as metal nodes [102-104]. Known as a light and relatively cheap metal, aluminium-based MOFs are interesting for industrial applications. However, aluminium's low reactivity once oxidized can make these MOFs difficult to synthesize [105]. MIL-100(Al) is known as one of the 'giant pore MOFs' as its structure consists of 25-29 Å mesocages connected through 5-9 Å pores with BTC as a linker. While other MOFs can be synthesized under comparatively diverse synthesis conditions, MIL-100(Al) is formed only in an aqueous mixture of linker and nitric acid at 210 °C for 3.5 h. The electrosynthesis of MIL-100(Al) is difficult with products only being formed in a solution with a water-ethanol ratio of 3:1, temperatures above 60 °C, and a current density of 10 mA/cm^2 [65]. The hydrogen evolution in the electrochemical cell results in a pH increase which complicates the electrosynthesis of MIL-100 that requires low pH. MIL-53(Al) utilizes a terephthalic acid linker, crystalizing into a structure with diamond-shaped pores. The amino-version of MIL-53, NH_2-MIL-53 is an isoreticular MOF, having the same structure as MIL-53(Al) but employing a different linker, in this case amino-terephthalic acid. Terephthalic acid and especially amino- terephthalic acid have a higher solubility in water compared to trimesic acid. Gascon *et al.* synthesized MIL-53(Al) in a mixture of water and DMF with KCl as supporting electrolyte [65]. Of special interest was that electrochemically synthesized MIL-53s did not display any breathing properties and that the degree of openness in the final structured could be controlled by changing the solvent used during synthesis. This effect was attributed to the formation of defective lattices and very small intergrown particles composed mostly of grain boundaries.

Thin films of both HKUST-1 and MIL-100(Fe) were electrosynthesized at high temperatures and pressures in a specialized high pressure cell in presence of a 2:1 ethanol-water solution of BTC and MTBS using either copper or iron electrodes [88]. Dense MOF films were obtained in absence of MTBS electrolyte whereas the addition of MTBS electrolyte resulted in the formation of more MOF crystals both in solution and partially on the electrodes. Fully intergrown films were formed under a temperature range of 110 to 190 °C and current densities of 2 to 20 mA/cm^2 (See Figure **1.4**). At 100-130 °C, crystals with a wide size distribution were formed whereas higher temperatures resulted in more monodisperse crystals of smaller sizes. This is mainly due to an increase in nucleation rate at increasing temperature. Due to the high temperature and acidity of the solution (pH 3), some MIL-100(Fe) crystals were formed even without applying a voltage.

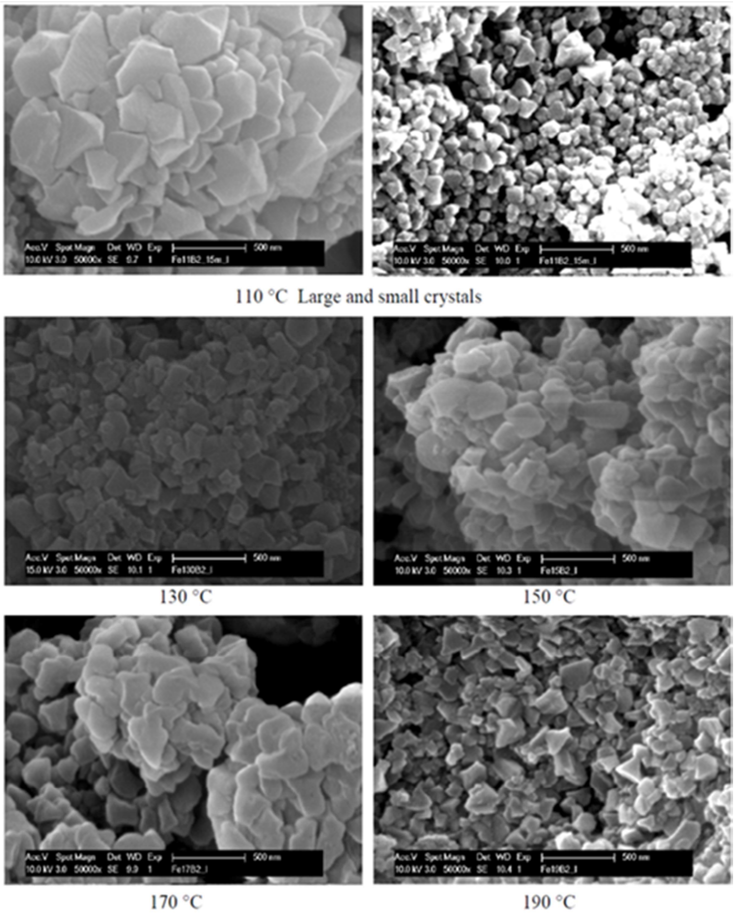

110 °C Large and small crystals

130 °C

150 °C

170 °C

190 °C

Figure 1.4. SEM images shows MIL-100(Fe) synthesized at different temperatures (reprinted from [58] with permission from The Royal Society of Chemistry).

MOFs can be doped with different ions for various applications after they are electrosynthesized. For example, Li^+ doped Fe-BTC was obtained by first electrosynthesis of Fe-BTC in a methanol solution of BTC and MTBS (using an iron anode and a steel cathode within a distance of 1 cm[48] . The electrolysis was performed at 32 °C and applying a current of 3.8 A/dm^2 for 55 min. Then, $LiPF_6$ was added to the resulting brown suspension and stirred for 12 hours. Although very little information was provided regarding the structure of the product, this MOF was used for impedimetric detection of gas molecules.

Ionothermal synthesis using ionic liquids as solvents can also be applied in electrosynthesis of MOFs [106]. Ionic liquids contain organic anions and cations. In contrast to conventional solvents for electrosynthesis of MOFs such as water, DMF, methanol, and ethanol, ionic liquids are a diverse group of non-flammable, tuneable solvents with very low vapour pressure, a high thermal stability, and a wide electrochemical window. These advantages allow for the design and use of ionic liquids for various applications [107]. As a medium (solvent and electrolyte) for the electrosynthesis of MOFs, ionic liquids affect the structure and morphology of the product. In general, the cations function as templates and direct the framework structures, whereas the anions interact with the metal cations [108]. For example, Liang *et al.* prepared a particular flower-shaped MOF-5 by *in situ* electrosynthesis in a tuneable ionic liquid [90]. They selected BMIM (1-butyl-3-methylimidazole) bromine as a template for the electrosynthesis of MOF-5. The electrical conductivity increased in presence of the ionic liquid. Due to the interactions between BMIM and the linkers, they obtained a novel flower-like morphology. In spite of the poor stability of MOF-5, the authors applied the obtained material in the electrochemical hydrogen evolution reaction.

The high flexibility in electrosynthesis of thin films of MOFs allows the deposition of MOF layers with different metal nodes. MOFs can also be doped by the addition of the dopant to the synthesis solution. For example, Fransaer *et al.* electrosynthesized Gd-BTC and Tb-BTC *via* anodic dissolution for the detection of explosives such as DNT (a side product in the TNT-production) [109]. They doped Gd-BTC with Tb by addition of $Tb(NO_3)_3$ to the synthesis solution. The ratio of Gd to Tb was tuned by changing the amount of $Tb(NO_3)_3$. To lower the costs associated with lanthanides, zinc oxide doped with Tb was electrosynthesized on zinc plate and then turned into ZnO(Tb)-BTC. The morphology of zinc oxide completely changed from hexagonal structure into a layer of intergrown needles.

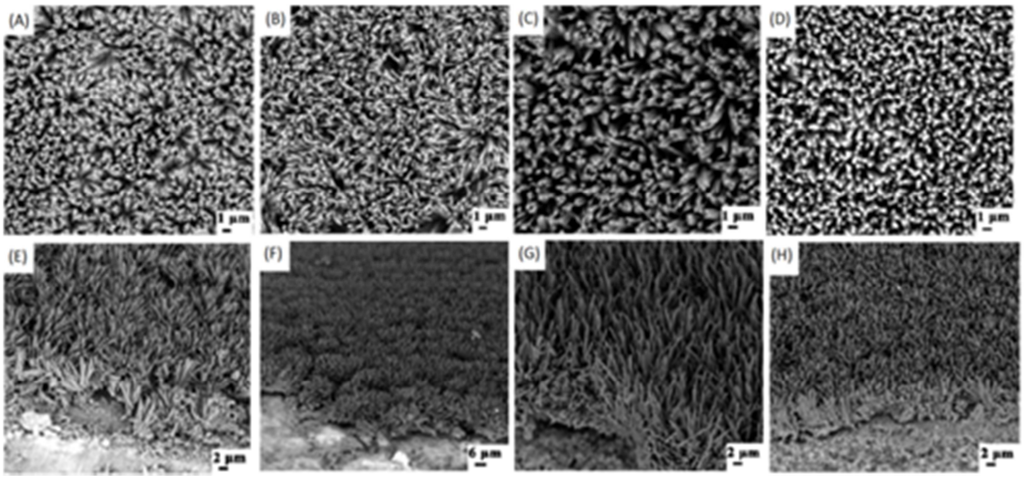

Figure 1.5. SEM images showing MOF-5 electrosynthesized at different applied potentials: (A) 0.5 V, (B) 1.0 V, (C) 1.5 V, and (D) 2.0 V for 60 s with a cross-section view at 45° (E-H) (reprinted from 60 with permission from the Royal Society of Chemistry).

Cao *et al.* electrosynthesized thin films of rod-like MOF-5 as a fluorescent sensing element for detection of aromatic nitro explosives [91]. MOF-5 was electrosynthesized using two zinc electrodes in an aqueous solution of BDC and ammonium fluoride (supporting electrolyte) at 65 °C. The influence of applied potential and synthesis time was studied to optimize the detection of various nitrobenzenes. An increase in the applied voltage resulted in the formation of denser, rougher and thicker films with less defects (See Figure **1.5**). Increase of synthesis time led to not only thicker and rougher films but also to a preference of epitaxial growth of the synthesized rods. The most compact and uniform film was obtained at 2 V for 40 s synthesis and was used for the detection of various nitrobenzenes.

Anodic dissolution can also be triggered wirelessly for the deposition of MOFs on a floating conductive object in a solution *via* indirect bipolar electrodeposition. This method, which has been previously used for the synthesis of Janus particles, is based on the positioning of a conducting object in an electric field between two electrodes; thus, both ends of the objects are polarized giving rise to different redox reactions (See Figure **1.2**B). Kuhn *et al.* recently demonstrated the application of this method for the synthesis of MOFs [110]. They employed a zinc wire as both metal source and substrate for selective deposition. The zinc wire was then floated between the two electrodes. By applying a voltage between the electrodes, the zinc wire was polarized at both ends, leading to zinc dissolution in one end and hydrogen evolution at the other end. The Zn^{2+} ions dissolved at the positively polarized side of the wire react with the 2-methylimidazole linker to form ZIF-8. Surprisingly, in this case films of ZIF-8 could be synthesized. The influence of applied voltage, concentration and synthesis time were examined and optimized. They also extended this approach to electrosynthesis of HKUST-1 on a copper sphere.

As shown above, electrochemical methods allow for the formation of a highly localized concentration of metal ions near the electrode surface, offering the possibility to form thin films of MOFs on the electrode. Although the use of electrosynthesis methods for the formation of MOFs are growing rapidly, little is known about the mechanism of electrosynthesis process, the nucleation and growth mechanisms, and the adhesion or lack of adhesion of the MOFs to the electrode surface. More fundamental research is thus required to uncover the different chemical processes at both the anode and the cathode during the formation of MOFs. As an early study, Campagnol *et al.* divided the mechanism of growth of HKUST-1 thin film into four phases [111]: nucleation, growth of islands, intergrowth, and detachment; Nucleation occurs when a critical concentration is reached near the electrode surface. These newly formed crystals offer nucleation sites for other crystals, resulting in the formation of the crystal islands that continue to grow until a dense film is formed. The porosity of the MOF allows ions to diffuse through the thin film, allowing growth of the thin film. Finally, the substrate under the crystals (the electrode) dissolves further, causing detachment.

1.2.1.2 Reductive de-protonation

Reductive de-protonation is a relatively new electrosynthesis method for direct formation of MOFs on a conductive substrate. The concept relies on the use of an electrochemical method to cause in a rise in pH and subsequent de-protonation of the linker. Like anodic dissolution, this causes the nucleation of MOF crystals near the electrode surface and consequent formation of a thin MOF layer. This method was first introduced and patented by Dinca *et al.* to grow a MOF-5 thin film on FTO electrode **[112, 113]**.The electrosynthesis was carried out in DMF/water solution containing $Zn(NO_3)_2$ (source of the metal) and $(NBu_4)PF_6$ (as electrolyte) using an FTO working electrode and $Ag/Ag(cryptand)^+$ as reference electrode. They took advantage of an increase in pH upon electroreduction of oxoanions such as NO_3^-. The linker (H_2BDC: 1,4-benzene-dicarboxylic acid) is then deprotonated in such alkaline condition and accordingly reacts with the metal precursor:

$$NO_3^- + H_2O + 2e^- \rightarrow NO_2^- + 2OH^- \qquad (1)$$

$$H_2BDC + OH^- \rightarrow HBDC^+ + H_2O \qquad (2)$$

Even though a MOF-5 thin film was synthesized, the potential required to reduce NO_3^- (-1.75 V *vs*. $Ag/Ag(cryptand)^+$) was higher than the reduction potential of zinc (-1.00 V *vs*. $Ag/Ag(cryptand)^+$). Thus, zinc metal was deposited alongside the MOF thin film. This problem was later overcome by using triethylammonium (Et_3NH^+) as a probase **[114]** as it requires a less negative reduction potential (onset potential for reduction of proton: -0.5 V *vs.* $Ag/Ag(cryptand)^+$) at a Pt electrode. The reduction of this probase results in the formation of the base triethylamine (Et_3N) and H_2, which is inert and does not interfere with the formation of MOF (See Figure **1.2**C). The formed base can then deprotonate the linker :

$$2R_3NH^+(R = alkyl) + 2e^- \rightarrow 2R_3N + H_2 \quad (3)$$

$$2H_2BDC + 2e^- \rightarrow H_2 + 2HBDC^- \qquad (4)$$

The Et_3NH^+/Et_3N buffer pair also allows for more control over the electrosynthesis conditions and was credited for the absence of zinc deposition on the electrode. By modulating the electrode potential and Et_3NH^+ concentration, heterostructures of MOF-5 and bilayer structures of MOF-5 and $(Et_3NH)_2Zn_3(BDC)_4$ were also obtained from a solution of $Zn(NO_3)_2$ and H_2BDC in DMF and $TBAPF_6$ as electrolyte.

Yang *et al.* synthesized thin films of Eu-HBPTC MOF on FTO electrode in the mixture of benzophenone-3,3',4,4'-tetracarboxylic dianhydride (BTDA) and $Eu(NO_3)_3.6H_2O$ in DMF **[115]**. The electroreduction of NO_3^- at FTO electrode produced OH^- that catalyses the hydrolysis of the anhydride groups of BTDA and generate benzophenone-3,3',4,4'-tetracarboxylate ($BPTC^{4-}$) and its different protonation products ($HBPTC^{3-}$, H_2BPTC^{2-}, and H_3BPTC^-), dependening on the solution pH. Eu-HBPTC was formed upon reaction with Eu^{3+} and was employed as luminescent sensor for the detection of carbonate.

This second method for the direct electrosynthesis of MOFs has the advantage that it allows the formation of MOF thin films on a broader variety of conductive substrates. Furthermore, through clever selection of the probase, the need for extreme voltages and unwanted side reactions can be avoided. However, the need for fairly negative potentials, even with the use of triethylammonium means that this method is not suited for frameworks containing easily reduced metals such as copper. In such cases, one may currently opt for the anodic dissolution method.

1.2.2 Indirect electrosynthesis of MOFs

Even though not strictly considered as electrosynthesis methods, electrochemical methods can be employed as one of a series of steps in the synthesis of MOFs. In such cases, the method is called indirect electrosynthesis of MOFs.

1.2.2.1 Anchoring of a linker

One of the methods used to form thin films of MOFs is the anchoring of a linker or a similar moiety to the substrate surface. This linker then acts as a nucleation site for the formation of MOF crystals (Figure **1.2**D). On conductive surfaces, linkers can be attached chemically or electrochemically. Telfer *et al.* developed two methods for formation of HKUST-1 on glassy carbon electrode [116]. The first method was based on grafting 4-carboxyphenyl radicals to the electrode by reduction of 4-carboxybenzenediazonium cations. The grafted substrate was then immersed in an ethanol solution of $Cu(NO_3)_2$ and BTC at an elevated temperature. In the second method, the glassy carbon electrode surface was roughened by using SiC abrasive paper. This results in formation of oxygenic functional groups such as carboxylic groups which may act similar to the grafted group in the first method. The growth of HKUST-1 was then induced by repetitive cyclic voltammetry in $Cu(NO_3)_2$ and BTC solution. Afterwards, the electrode was transferred to the precursor solution at 85 ° C. In both methods, HKUST-1 was formed at glassy carbon electrode; however, in the first method, an open but not continuous and in second method a dense, intergrown and continuous network of HKUST-1 crystals was obtained. Using the first approach indicated above, Hu *et al.* electrosynthesized MOF-5 on a glassy carbon electrode [117] except that after pre-treatment of the electrode, they transferred the electrode to a solution of $Zn(NO_3)_2 \cdot 6H_2O$ and terephthalic acid in DMF at 120 °C for 48 hours (See Figure **1.2**D).

1.2.2.2 Galvanic displacement

Galvanic displacement occurs when more noble metal ions are in contact with a less noble metallic substrate. The difference in reduction potential results in the reduction of the more noble metal on the metallic substrate and the oxidation of the metallic substrate. This results in the release of metal ions and formation of MOFs. Thus, in this method, metal ions are locally supplied without the need for an external power source and electrical contact. De Vos *et al.* developed this method for growing patterns of HKUST-1 on glass [118]. They first patterned a glass substrate by metallic Cu. After a solution of silver nitrate and H_3BTC in DMF was spin-coated on top, the sample was heated at 80 °C. Here, the silver ions were reduced and Cu (II) ions were released, leading to the formation of HKUST-1.

1.2.2.3 Electrophoretic deposition

Traditionally used for the processing of ceramics [119], electrophoretic deposition relies on the use of an electric field to deposit charged, colloidal particles onto a conducting surface. The great advantage of this technique comes from its versatility as was highlighted by Hupp *et.al* who applied this method for the deposition of metal-organic frameworks[120]. Besides the synthesis of well-known HKUST-1, they also succeeded in the formation of thin films consisting of MIL-53 and the zirconium-based UiO-66 and NU-1000. Intrinsic surface defects present in the MOF particles leave them with a negative net surface charge in solution. Using two identical FTO plates, a thin film was formed from a suspension of pre-made MOF particles in toluene. With an applied potential of 90 V, a full coverage of the FTO surface was obtained after 3 hours. Furthermore, the strengths of this technique were shown by the deposition of MOFs onto a patterned conducting surface and depositing two different MOFs consecutively on the same electrode. Finally, the reversible electrochromism of the pyrene moieties present in the linker of NU-1000 were investigated. The finding showed that even though some MOF particles were not in direct contact with the FTO electrode, they were still able to participate in the electrochemical reaction. This led the authors to assume that particle-particle redox communication was possible.

Whereas most techniques for thin films formation depend on the properties of MOFs such as crystallisation kinetics and require well-defined synthesis conditions[121], this technique allows the facile deposition of a variety of MOFs. However, they must form a stable colloidal suspensions, and organic solvents must be used to ensure no side reactions take place[122]. Furthermore, even though this method is not used for the direct electrosynthesis of MOFs, it does show that the presence of an electric field has an effect on charged moieties in solution, an effect which has not mentioned in the electrosynthesis of other MOFs.

1.2.2.4 Self-template synthesis based on metal oxides /hydroxide nanostructures

Finally, metal-oxides can be employed as metal source as well as nucleation site for the formation of MOFs [69]. In this method, metal oxides are first prepared by an electrochemical method and consequently turn into MOFs in the presence of related linkers. The morphology of the metal oxide is controlled by the reaction conditions and electrochemical parameters. The metal oxide morphology can subsequently affect the morphology of the resulting MOFs.

An interesting example is the growth of a ZIF-8 on zinc oxide nanorods formed *via* electrodeposition [123]. Here, ZnO nanorods act both as the template and the source of Zn^{2+} for the synthesis of ZIF-8. ZnO nanorod arrays were grown on FTO electrode *via* galvanostatic electrodeposition in an aqueous solution of $Zn(NO_3)_2.6H_2O$ and hexamethylenetetramine (HMTA- as an electrolyte additive) for 50 min. Then, the FTO modified with ZnO nanorod arrays was placed in an autoclave together with 2-methylimmidazol and a mixed solvent of H_2O/DMF at 70 °C for 24 hours, yielding ZnO/ZIF-8 nanorod arrays. These arrays were later used for the photocatalytic sensing of hydrogen peroxide in presence of ascorbic acid. By acting as a sieve, ZIF-8 was able to let hydrogen peroxide penetrate through the pores while keeping ascorbic acid out, allowing for a selective electrochemical sensor. Costly metals such as europium can also be deposited as an oxide before being converted into a MOF. Yang et al. first electrodeposited $Eu(OH)_2$, afterwards turning it into a thin MOF layer through a subsequent solvothermal step [124]. This film was then used for the luminescent detection of lead ions.

1.3 Discussion

Several key points have to be carefully considered in synthesis of MOFs. Synthesis conditions, such as pH, temperature, solvent, and additives play important roles in synthesis of MOFs as they mainly influence the solubility of the linker, diffusion rate, and the level of linker de-protonation [58]. Thus, alteration of the synthesis conditions greatly influences the reaction rate as well as the quality of the product and may affect coordination of the metal. On the other hand, linkers can only form bonds with the metal ions upon de-protonation. Alteration of linkers solubility or their level of de-protonation and, therefore, the way linker and metal bind, allows for the formation of different structures [125].

Solvents and additives also affect porosity, particle shape and size of the synthesized MOFs. In most cases, a different activation procedure than that used after solvothermal or hydrothermal synthesis will be required to avoid structure collapse [68, 126, 127]. The synthesis temperature also plays a large role in MOFs structure, porosity and kinetics of formation. A higher synthesis temperature increases the linker solubility and, at the same, time may reduce the amount of defects. Higher temperatures allow for the constant forming and reforming of bonds, allowing defects to be healed [128]. Synthesis conditions also influence the behaviour of metal ions. Although some MOFs require metal-oxide clusters instead of metal-ions centres [129], metals that do not form oxides often have corresponding MOFs which are easier to synthesize [130]. The use of an aprotic solvent or alteration of pH can eliminate oxide formation and, therefore, facilitate the synthesis. The nature of the metal, linker, and their interactions dictate which synthesis conditions are optimal, with subtle changes resulting in the formation of different structures, especially when it comes to MOFs based on tri and tetra valent cations [58]. Some MOFs can easily be made under ambient conditions [131], whereas others require specific pH, solvents, and temperatures to be formed at all [132].

As shown above, the use of electrochemical methods adds additional dimensions to the choice of synthesis conditions. First of all, the electrochemical synthesis conditions such as applied potential or current directly influence the rate of synthesis and crystal nucleation. These parameters, along with the choice of solvent and electrodes can also determine which reactions take place during synthesis. Furthermore, the conductivity of the solvent and the choice of the electrolyte have large impact. Most common solvents for the synthesis of MOFs are DMF, DEF (*N*,*N*-diethylformamide), NMP (1-methyl-2-pyrrolidone), water, and ethanol (all with a limited electrical conductivity). A very non-conductive solvent may result in a large ohmic drop and influence the diffusion rate of the ions. Thus, the addition of an electrolyte to the reaction media is often required to enhance the charge transport in the solution. Although the type of supporting electrolyte for electrosynthesis of MOFs has yet to be optimized, the most common salt currently used is MTBS. As in other electrochemical measurements, a counter electrode with a larger surface area should be employed to ensure the reactions at counter electrodes do not limit the processes at the working electrode. Stainless steel gauze electrodes are common counter electrodes in electrosynthesis of MOFs.

Currently, most electrosynthesis methods rely on a two electrode system without a reference electrode. A reference electrode allows more control over the applied potential and more uniformity in the applied potential values reported and thus, more concrete procedure for follow-up research. However, standard commercial reference electrodes such as Ag/AgCl or calomel electrodes contain saturated KCl solutions which are not soluble in most organic solvents. Leakage from the reference electrode and the presence of Cl^- can also affect the MOF morphology or result in contamination of the framework. One way to overcome this limitation is to use a glass frit or a Luggin capillary electrode that allows slow diffusion of water or solvent molecules. However, prolonged application of this approach leads to a high junction potential difference. Currently, $Ag/Ag(cryptand)^+$ is the most common reference electrode in electrosynthesis of MOFs. Another limitation is the use of a reference electrode at elevated temperatures (>60 °C) in organic solvents. Therefore, development of new reference electrodes, applicable under MOF electrosynthesis conditions, needs further research attention. The presence of an electric field and side reactions occurring at certain potentials can also influence the synthesis. These include water splitting in case of aqueous solvents, but also oxidation or reduction of linkers, organic solvents and even different oxidation states of metal ions. Furthermore, the effects of side reactions occurring during electrosynthesis on MOFs stability has not been duly examined. Most MOFs that have currently investigated are either the only possible phase for a given linker-metal combination or the thermodynamically stable structure in different topologies, and the effect of changes in pH or solvent chemistry during electrosynthesis have not been examined for more sensitive MOFs.

Finally, the quality of the obtained MOFs is also very important. For MOF powders, this quality is usually assessed by measurement of the surface area and pore volume per gram of MOF. From this method, one can ascertain that MOF powders synthesised electrochemically have a quality similar to those synthesised hydrothermally. Anodic dissolution eliminates the use of metal salts, preventing their entrapment in the MOF pores. However, the use of conducting salts can result in entrapment and care must be taken to remove them. For thin films of MOF, these measurements are challenging because of the small amount of MOF obtained. Even though XRD data can be used to assess their crystallinity, care must be taken when using this data to compare the quality of MOF thin films. The conditions used when obtaining the data, such as scanning speed and thickness can affect these results. Thus, more research is necessary in order to ascertain if the porosity is indeed retained when using electrochemical synthesis methods for the formation of MOF thin films.

1.4 Conclusion

Electrochemical synthesis of MOFs provides many advantages, such as milder synthesis conditions, shorter synthesis times and the ability to control the rate of synthesis as it is occurring. Recent literature has shown that electrochemistry provides a strong tool for the synthesis of thin films in particular and allow for the fine tuning of crystal morphology.

Even though most literature has dealt with the formation of HKUST-1, a MOF that is relatively easy to synthesize, research into the formation of other MOFs seems to be growing. Most notably, electrosynthesis methods are used for the formation of MOFs for sensing applications. However, electrochemical synthesis is still in a young stage and more research needs to be done into the effects of various synthesis conditions and their effect on each other as well as the synthesis of a larger variety of MOFs. This is particularly difficult as the individual role of certain synthesis conditions such as solvent properties and conductivity conditions are hard to separate and such conditions vary for different MOFs.

Finally, a better understanding on the effect of side reactions is needed. This would allow for easier insight into the appropriate synthesis parameters as well as whether certain MOFs can be synthesized using electrochemical synthesis methods. Water splitting can affect the pH of the solution and lead to the formation of less or unwanted products, as was shown for the synthesis of MIL-100 and HKUST-1. Oxidation or reduction of the linker and organic solvent as well as formation of metallic species and their effect on synthesis should also be thoroughly investigated.

1.5 References

1. J. D. Evans, C. J. Sumby and C. J. Doonan, *Chemical Society Reviews*, 2014, 43, 5933-5951.
2. H. Furukawa, N. Ko, Y. B. Go, N. Aratani, S. B. Choi, E. Choi, A. Ö. Yazaydin, R. Q. Snurr, M. O'Keeffe, J. Kim and O. M. Yaghi, *Science*, 2010, 329, 424-428.
3. W. Lu, Z. Wei, Z.-Y. Gu, T.-F. Liu, J. Park, J. Park, J. Tian, M. Zhang, Q. Zhang, T. Gentle Iii, M. Bosch and H.-C. Zhou, *Chemical Society Reviews*, 2014, 43, 5561-5593.
4. Y. Kinoshita, I. Matsubara, T. Higuchi and Y. Saito, *Bull. Chem. Soc. Jpn.*, 1959, 32, 1221-1226.
5. A. A. Berlin and N. G. Matveeva, *Russ. Chem. Rev.*, 1960, 29, 119-128.
6. B. P. Block, E. S. Roth, C. W. Schaumann, J. Simkin and S. H. Rose, *J. Am. Chem. Soc.*, 1962, 84, 3200-&.
7. F. W. Knobloch and W. H. Rauscher, *Journal of Polymer Science*, 1959, 38, 261-262.
8. M. Kubo, M. Kishita and Y. Kuroda, *Journal of Polymer Science*, 1960, 48, 467-471.
9. E. A. Tomic, *J. Appl. Polym. Sci.*, 1965, 9, 3745-&.
10. S. R. Batten, B. F. Hoskins and R. Robson, *J. Am. Chem. Soc.*, 1995, 117, 5385-5386.
11. B. F. Hoskins and R. Robson, *J. Am. Chem. Soc.*, 1990, 112, 1546-1554.
12. S. Kitagawa, S. Kawata, Y. Nozaka and M. Munakata, *J. Chem. Soc., Dalton Trans.*, 1993, DOI: 10.1039/dt9930001399, 1399-1404.
13. S. Kitagawa, S. Matsuyama, M. Munakata and T. Emori, *J. Chem. Soc., Dalton Trans.*, 1991, DOI: 10.1039/dt9910002869, 2869-2874.
14. O. M. Yaghi and H. L. Li, *J. Am. Chem. Soc.*, 1995, 117, 10401-10402.
15. G. B. Gardner, D. Venkataramani, J. S. Moore and S. Lee, *Nature*, 1994, 374, 792-795.
16. D. Riou and G. Ferey, *J. Mater. Chem.*, 1998, 8, 2733-2735.
17. O. K. Farha, I. Eryazici, N. C. Jeong, B. G. Hauser, C. E. Wilmer, A. A. Sarjeant, R. Q. Snurr, S. T. Nguyen, A. Ö. Yazaydın and J. T. Hupp, *J Am Chem Soc*, 2012, 134, 15016-15021.
18. H. Furukawa, K. E. Cordova, M. O'Keeffe and O. M. Yaghi, *Science*, 2013, 341.
19. J.-R. Li, R. J. Kuppler and H.-C. Zhou, *Chemical Society Reviews*, 2009, 38, 1477-1504.
20. H. Li, M. Eddaoudi, M. O'Keeffe and O. M. Yaghi, *Nature*, 1999, 402, 276-279.
21. M. Kandiah, M. H. Nilsen, S. Usseglio, S. r. Jakobsen, U. Olsbye, M. Tilset, C. Larabi, E. A. Quadrelli, F. Bonino and K. P. Lillerud, *Chem. Mater.*, 2010, DOI: 10.1021/cm102601v, null-null.
22. J. Liu, L. Chen, H. Cui, J. Zhang, L. Zhang and C.-Y. Su, *Chemical Society Reviews*, 2014.
23. J. Gascon, A. Corma, F. Kapteijn and F. X. Llabrés i Xamena, *ACS Catalysis*, 2013, 4, 361-378.
24. K. F. Babu, M. A. Kulandainathan, I. Katsounaros, L. Rassaei, A. D. Burrows, P. R. Raithby and F. Marken, *Electrochemistry Communications*, 2010, 12, 632-635.
25. J.-R. Li, J. Sculley and H.-C. Zhou, *Chemical reviews*, 2011, 112, 869-932.
26. S. Ma and H.-C. Zhou, *Chem Commun (Camb)*, 2010, 46, 44-53.
27. F. A. Almeida Paz, J. Klinowski, S. M. F. Vilela, J. P. C. Tome, J. A. S. Cavaleiro and J. Rocha, *Chemical Society Reviews*, 2012, 41, 1088-1110.
28. R. Sabouni, H. Kazemian and S. Rohani, *Environmental Science and Pollution Research*, 2014, 21, 5427-5449.
29. C. Brozek and M. Dincă, *Chemical Society Reviews*, 2014.
30. S. Couck, J. F. M. Denayer, G. V. Baron, T. Remy, J. Gascon and F. Kapteijn, *J. Am. Chem. Soc.*, 2009, 131, 6326-6327.
31. J.-L. Wang, C. Wang and W. Lin, *ACS Catalysis*, 2012, 2, 2630-2640.

32. M. Nasalevich, M. A. van der Veen, F. Kapteijn and J. Gascon, *CrystEngComm*, 2014, DOI: 10.1039/C4CE00032C.
33. M. A. Nasalevich, M. G. Goesten, T. J. Savenije, F. Kapteijn and J. Gascon, *Chem Commun*, 2013, 90, 10575-10577.
34. M. Zhang, Z.-Y. Gu, M. Bosch, Z. Perry and H.-C. Zhou, *Coordination Chemistry Reviews*, DOI: http://dx.doi.org/10.1016/j.ccr.2014.05.031.
35. E. Coronado and G. Minguez Espallargas, *Chemical Society Reviews*, 2013, 42, 1525-1539.
36. M. Kurmoo, *Chemical Society Reviews*, 2009, 38, 1353-1379.
37. C. H. Hendon, D. Tiana and A. Walsh, *Physical Chemistry Chemical Physics*, 2012, 14, 13120-13132.
38. D. M. D'Alessandro, J. R. R. Kanga and J. S. Caddy, *Australian Journal of Chemistry*, 2011, 64, 718-722.
39. J. Juan-Alcaniz, J. Gascon and F. Kapteijn, *J. Mater. Chem.*, 2012, 22, 10102-10118.
40. C. Rosler and R. A. Fischer, *CrystEngComm*, 2015, DOI: 10.1039/C4CE01251H.
41. M. Nasalevich, R. Becker, E. V. Ramos Fernandez, S. Castellanos, S. L. Veber, M. V. Fedin, F. Kapteijn, J. N. H. Reek, J. I. van der Vlugt and J. Gascon, *Energy & Environmental Science*, 2014, DOI: 10.1039/C4EE02853H.
42. S. M. Cohen, *Chemical reviews*, 2011, 112, 970-1000.
43. K. K. Tanabe and S. M. Cohen, *Chemical Society Reviews*, 2011, 40, 498-519.
44. M. Zhao, S. Ou and C.-D. Wu, *Accounts of Chemical Research*, 2014, 47, 1199-1207.
45. A. Dhakshinamoorthy and H. Garcia, *Chemical Society Reviews*, 2012, 41, 5262-5284.
46. J. Lei, R. Qian, P. Ling, L. Cui and H. Ju, *TrAC Trends in Analytical Chemistry*, 2014, 58, 71-78.
47. Y. Cui, B. Chen and G. Qian, *Coordination Chemistry Reviews*, 2014, 273–274, 76-86.
48. S. Achmann, G. Hagen, J. Kita, I. Malkowsky, C. Kiener and R. Moos, *Sensors-Basel*, 2009, 9, 1574-1589.
49. T. Zhang and W. Lin, *Chemical Society Reviews*, 2014, 43, 5982-5993.
50. Y. Li, C. Chen, X. Sun, J. Dou and M. Wei, *ChemSusChem*, 2014, 7, 2469-2472.
51. J. Della Rocca, D. Liu and W. Lin, *Accounts of Chemical Research*, 2011, 44, 957-968.
52. P. Horcajada, R. Gref, T. Baati, P. K. Allan, G. Maurin, P. Couvreur, G. Férey, R. E. Morris and C. Serre, *Chemical reviews*, 2011, 112, 1232-1268.
53. G. K. H. Shimizu, J. M. Taylor and S. Kim, *Science*, 2013, 341, 354-355.
54. A. Morozan and F. Jaouen, *Energy & Environmental Science*, 2012, 5, 9269-9290.
55. J. Yang, P. Xiong, C. Zheng, H. Qiu and M. Wei, *Journal of Materials Chemistry A*, 2014, 2, 16640-16644.
56. N. Campagnol, R. Romero-Vara, W. Deleu, L. Stappers, K. Binnemans, D. E. De Vos and J. Fransaer, *ChemElectroChem*, 2014, 1, 1182-1188.
57. Y.-R. Lee, J. Kim and W.-S. Ahn, *Korean J. Chem. Eng.*, 2013, 30, 1667-1680.
58. M. G. Goesten, F. Kapteijn and J. Gascon, *CrystEngComm*, 2013, 15, 9249.
59. T. Rodenas, I. Luz, G. Prieto, B. Seoane, H. Miro, A. Corma, F. Kapteijn, F. X. Llabrés i Xamena and J. Gascon, *Nature materials*, 2015, 14, 48-55.
60. J. Klinowski, F. A. Almeida Paz, P. Silva and J. Rocha, *Dalton Transactions*, 2011, 40, 321-330.
61. M. Klimakow, P. Klobes, A. F. Thünemann, K. Rademann and F. Emmerling, *Chemistry of Materials*, 2010, 22, 5216-5221.
62. B. Liu and R. A. Fischer, *Science China Chemistry*, 2011, 54, 1851-1866.

63. C. G. Carson, A. J. Brown, D. S. Sholl and S. Nair, *Crystal Growth & Design*, 2011, 11, 4505-4510.
64. R. Ameloot, L. Stappers, J. Fransaer, L. Alaerts, B. F. Sels and D. E. De Vos, *Chemistry of Materials*, 2009, 21, 2580-2582.
65. A. Martinez Joaristi, J. Juan-Alcañiz, P. Serra-Crespo, F. Kapteijn and J. Gascon, *Crystal Growth & Design*, 2012, 12, 3489-3498.
66. A. Bétard and R. A. Fischer, *Chemical reviews*, 2011, 112, 1055-1083.
67. V. V. Guerrero, Y. Yoo, M. C. McCarthy and H.-K. Jeong, *J Mater Chem*, 2010, 20, 3938-3943.
68. N. Stock and S. Biswas, *Chemical reviews*, 2011, 112, 933-969.
69. D. Bradshaw, A. Garai and J. Huo, *Chem. Soc. Rev.*, 2011.
70. S. T. Meek, J. A. Greathouse and M. D. Allendorf, *Adv Mater*, 2011, 23, 249-267.
71. J. Gascon and F. Kapteijn, *Angew. Chem., Int. Ed.*, 2010, 49, 1530-1532.
72. U. Mueller, H. Puetter, M. Hesse and H. Wessel, Google Patents, 2005.
73. E. Biemmi, S. Christian, N. Stock and T. Bein, *Microporous and Mesoporous Materials*, 2009, 117, 111-117.
74. E. Stavitski, M. Goesten, J. Juan-Alcañiz, A. Martinez-Joaristi, P. Serra-Crespo, A. V. Petukhov, J. Gascon and F. Kapteijn, *Angew. Chem., Int. Ed.*, 2011, 50, 9624-9628.
75. C. Kasper, *Transactions of the Electrochemical Society*, 1940, 77, 353-363.
76. C. Wagner, *Electrochimica Acta*, 1967, 12, 131-136.
77. S. S.-Y. Chui, S. M.-F. Lo, J. P. H. Charmant, A. G. Orpen and I. D. Williams, *Science*, 1999, 283, 1148-1150.
78. U. Mueller, M. Schubert, F. Teich, H. Puetter, K. Schierle-Arndt and J. Pastre, *J Mater Chem*, 2006, 16, 626-636.
79. K. Schlichte, T. Kratzke and S. Kaskel, *Microporous and Mesoporous Materials*, 2004, 73, 81-88.
80. Q. M. Wang, D. Shen, M. Bülow, M. L. Lau, F. R. Fitch and S. Deng, Google Patents, 2002.
81. M. Hartmann, S. Kunz, D. Himsl, O. Tangermann, S. Ernst and A. Wagener, *Langmuir : the ACS journal of surfaces and colloids*, 2008, 24, 8634-8642.
82. R. Senthil Kumar, S. Senthil Kumar and M. Anbu Kulandainathan, *Microporous and Mesoporous Materials*, 2013, 168, 57-64.
83. M. G. Goesten, P. C. Magusin, E. A. Pidko, B. Mezari, E. J. Hensen, F. Kapteijn and J. Gascon, *Inorg. Chem.*, 2014, 53, 882-887.
84. T. R. C. Van Assche and J. F. M. Denayer, *Chem. Eng. Sci.*, 2013, 95, 65-72.
85. R. Pech and J. Pickardt, *Acta Crystallographica Section C*, 1988, 44, 992-994.
86. J. Gascon, S. Aguado and F. Kapteijn, *Microporous and Mesoporous Materials*, 2008, 113, 132-138.
87. T. R. C. Van Assche, G. Desmet, R. Ameloot, D. E. De Vos, H. Terryn and J. F. M. Denayer, *Microporous and Mesoporous Materials*, 2012, 158, 209-213.
88. N. Campagnol, T. Van Assche, T. Boudewijns, J. Denayer, K. Binnemans, D. De Vos and J. Fransaer, *Journal of Materials Chemistry A*, 2013, 1, 5827-5830.
89. S. Yadnum, J. Roche, E. Lebraud, P. Négrier, P. Garrigue, D. Bradshaw, C. Warakulwit, J. Limtrakul and A. Kuhn, *Angewandte Chemie*, 2014, 126, 4082-4086.
90. H. M. Yang, X. L. Song, T. L. Yang, Z. H. Liang, C. M. Fan and X. G. Hao, *RSC Advances*, 2014, 4, 15720-15726.
91. W. Li, J. Lu, S. Gao, Q. Li and R. Cao, *Journal of Materials Chemistry A*, 2014, DOI: 10.1039/C4TA04203D.

92. N. Campagnol, E. R. Souza, D. E. De Vos, K. Binnemans and J. Fransaer, *Chemical communications*, 2014, 50, 12545-12547.
93. K. S. Park, Z. Ni, A. P. Côté, J. Y. Choi, R. Huang, F. J. Uribe-Romo, H. K. Chae, M. O'Keeffe and O. M. Yaghi, *Proceedings of the National Academy of Sciences*, 2006, 103, 10186-10191.
94. J. Cravillon, R. Nayuk, S. Springer, A. Feldhoff, K. Huber and M. Wiebcke, *Chemistry of Materials*, 2011, 23, 2130-2141.
95. Y. Pan, Y. Liu, G. Zeng, L. Zhao and Z. Lai, *Chem Commun (Camb)*, 2011, 47, 2071-2073.
96. J. Yao and H. Wang, *Chemical Society Reviews*, 2014, 43, 4470-4493.
97. H. Bux, F. Liang, Y. Li, J. Cravillon, M. Wiebcke and J. Caro, *J. Am. Chem. Soc.*, 2009, 131, 16000-16001.
98. H. Bux, C. Chmelik, J. M. van Baten, R. Krishna and J. Caro, *Adv. Mater. (Weinheim, Ger.)*, 2010, 22, 4741-4743.
99. S. R. Venna, J. B. Jasinski and M. A. Carreon, *J Am Chem Soc*, 2010, 132, 18030-18033.
100. E. L. Bustamante, J. L. Fernández and J. M. Zamaro, *J Colloid Interf Sci*, 2014, 424, 37-43.
101. K. Kida, M. Okita, K. Fujita, S. Tanaka and Y. Miyake, *CrystEngComm*, 2013, 15, 1794-1801.
102. C. Serre, S. Bourrelly, A. Vimont, N. A. Ramsahye, G. Maurin, P. L. Llewellyn, M. Daturi, Y. Filinchuk, O. Leynaud, P. Barnes and G. Ferey, *Adv. Mater. (Weinheim, Ger.)*, 2007, 19, 2246-+.
103. D.-Y. Hong, Y. K. Hwang, C. Serre, G. Ferey and J.-S. Chang, *Adv. Funct. Mater.*, 2009, 19, 1537-1552.
104. C. Volkringer, D. Popov, T. Loiseau, G. Ferey, M. Burghammer, C. Riekel, M. Haouas and F. Taulclle, *Chem. Mater.*, 2009, 21, 5695-5697.
105. E. Haque, J. H. Jeong and S. H. Jhung, *CrystEngComm*, 2010, 12, 2749-2754.
106. R. E. Morris, *Chem Commun (Camb)*, 2009, DOI: 10.1039/b902611h, 2990-2998.
107. M. Armand, F. Endres, D. R. MacFarlane, H. Ohno and B. Scrosati, *Nat Mater*, 2009, 8, 621-629.
108. Z. Lin, D. S. Wragg, J. E. Warren and R. E. Morris, *Journal of the American Chemical Society*, 2007, 129, 10334-10335.
109. N. Campagnol, E. R. Souza, D. E. De Vos, K. Binnemans and J. Fransaer, *Chem Commun (Camb)*, 2014, 50, 12545-12547.
110. S. Yadnum, J. Roche, E. Lebraud, P. Négrier, P. Garrigue, D. Bradshaw, C. Warakulwit, J. Limtrakul and A. Kuhn, *Angew Chem Int Ed Engl*, 2014, 126, 4082-4086.
111. N. Campagnol, 2014.
112. M. Li and M. Dinca, *J Am Chem Soc*, 2011, 133, 12926-12929.
113. M. Dinca and M. Li, Google Patents, 2012.
114. M. Li and M. Dinca, *Chemical Science*, 2014, 5, 107-111.
115. H. Liu, H. Wang, T. Chu, M. Yu and Y. Yang, *Journal of Materials Chemistry C*, 2014, 2, 8683-8690.
116. S. Balakrishnan, A. J. Downard and S. G. Telfer, *J Mater Chem*, 2011, 21, 19207-19209.
117. C. Hou, J. Peng, Q. Xu, Z. Ji and X. Hu, *RSC Advances*, 2012, 2, 12696-12698.
118. R. Ameloot, L. Pandey, M. V. d. Auweraer, L. Alaerts, B. F. Sels and D. E. De Vos, *Chem Commun (Camb)*, 2010, 46, 3735-3737.
119. I. Corni, M. P. Ryan and A. R. Boccaccini, *Journal of the European Ceramic Society*, 2008, 28, 1353-1367.

120. I. Hod, W. Bury, D. M. Karlin, P. Deria, C.-W. Kung, M. J. Katz, M. So, B. Klahr, D. Jin, Y.-W. Chung, T. W. Odom, O. K. Farha and J. T. Hupp, *Advanced materials*, 2014, DOI: 10.1002/adma.201401940, n/a-n/a.

121. O. Shekhah, J. Liu, R. A. Fischer and C. Woll, *Chemical Society Reviews*, 2011, 40, 1081-1106.

122. L. Besra and M. Liu, *Progress in Materials Science*, 2007, 52, 1-61.

123. W.-w. Zhan, Q. Kuang, J.-z. Zhou, X.-j. Kong, Z.-x. Xie and L.-s. Zheng, *J Am Chem Soc*, 2013, 135, 1926-1933.

124. Y.-M. Zhu, C.-H. Zeng, T.-S. Chu, H.-M. Wang, Y.-Y. Yang, Y.-X. Tong, C.-Y. Su and W.-T. Wong, *Journal of Materials Chemistry A*, 2013, 1, 11312-11319.

125. H. Reinsch and N. Stock, *Microporous and Mesoporous Materials*, 2013, 171, 156-165.

126. A. P. Nelson, O. K. Farha, K. L. Mulfort and J. T. Hupp, *Journal of the American Chemical Society*, 2008, 131, 458-460.

127. O. K. Farha and J. T. Hupp, *Accounts of Chemical Research*, 2010, 43, 1166-1175.

128. J. L. C. Rowsell and O. M. Yaghi, *Microporous and Mesoporous Materials*, 2004, 73, 3-14.

129. A. Schaate, P. Roy, A. Godt, J. Lippke, F. Waltz, M. Wiebcke and P. Behrens, *Chemistry – A European Journal*, 2011, 17, 6643-6651.

130. T. Devic and C. Serre, *Chemical Society Reviews*, 2014, DOI: 10.1039/C4CS00081A.

131. D. J. Tranchemontagne, J. R. Hunt and O. M. Yaghi, *Tetrahedron*, 2008, 64, 8553-8557.

132. C. Volkringer, T. Loiseau, N. Guillou, G. r. Férey, M. Haouas, F. Taulelle, E. Elkaim and N. Stock, *Inorganic Chemistry*, 2010, 49, 9852-9862.

2 Synthesis of Zinc Oxide Nanorods and ZIF-8 Thin Film

A manuscript under preparation

2.1 Introduction

The combination of metal-organic frameworks with other functional materials enables the formation of multi-functional hybrid materials which benefit from the combined properties of the individual components [1]. This combination has allowed for the formation of materials with novel properties and applications in fields such as sensing [2-4], catalysis [5-7] and drug delivery [8]. Several methods have been developed to allow the formation of MOF hybrid structures. These methods include the encapsulation of nanoparticles within the pores of the MOF [9, 10], the formation of core-shell nanoparticles [11, 12] and the formation of MOF thin films on various substrates [13].

One of the most often studied MOFs is ZIF-8. Known for its remarkable stability [14] and ease of synthesis [15], this metal-organic framework has been used in the areas of sensing [16-18], catalysis [19-21], drug encapsulation [22-25], separation [26, 27] and many more. However, ZIF-8 thin films are notoriously difficult to grow due to its inherent nucleation mechanism [28] and must therefore be prepared though secondary nucleation, surface functionalization or the use of harsh and time consuming solvothermal methods [29]. It was recently shown that zinc oxide can aid the formation of ZIF-8 thin films by acting both as a nucleation site as well as a source of zinc ions [30]. Such a development allows for both the one-step formation of ZIF-8 membranes and thus the formation of hybrid materials, combining the properties of ZIF-8 and zinc oxide.

Zinc oxide is a semi-conductor with a wide bandgap of about 3.4 eV and a high exciton binding energy of 60 meV at room temperature. In recent years, zinc oxide has attracted much attention due to its biocompatibility, high electron mobility, chemical stability and ease of synthesis [31, 32]. Zinc oxide can be formed *via* gas phase deposition or wet chemical methods including hydrothermal and electrochemical deposition. The use of electrochemical deposition allows for the deposition of zinc oxide nanostructures in a short amount of time, using relatively simple equipment [33]. One of the most interesting aspects of zinc oxide is the possibility to form a large variety of nanostructures [34]. The investigation of zinc oxide and the effect of its nanomorphology in the fields of biosensing [35], photovoltaics, and electronics [36, 37] has therefore increased tremendously in recent years. However, whereas the morphology of zinc oxide has been investigated alongside synthesis and application of metal nanoparticles [38-40], quantum dots [41, 42] and enzymes [35], the exploitation of the large variety of zinc oxide morphologies alongside synthesis and application of MOFs is relatively unexplored.

Even though the use of zinc oxide is shown to facilitate the formation of ZIF-8 thin films, solvothermal methods are often still required to form ZIF-8 films [43-48]. A recent trend has been the use of solvent-free methods, relying instead on molten linkers for the formation of ZIF-8 as well as other MOFs. Whereas before, the linker was dissolved in a solvent, here the powdered linker is simply placed in contact with a metal oxide and heated to its melting point so as to form a metal-organic framework. This method is often performed using metal oxide powders with the aim of complete conversion to the desired MOF [49-51]. Ameloot *et al.* have recently used this method to form coatings of ZIF-8 on zinc oxide nanostructures [52]. The main advantages of using a molten linker for the formation of MOF thin films are the lack of solvent, the ability to re-use unreacted linker and shorter synthesis time with surface coverage being achieved in less than an hour in contrary with other methods that rely on a longer time such as a day or more [17, 43]. Furthermore, this method is green with water being the only side-product. However, the thin films synthesised by Ameloot *et al.* were inhomogeneous, with zinc oxide being fully consumed in some areas whereas others were left relatively uncovered. Furthermore, the crystals showed a wide size distribution with some crystals being as large as 1 µm in diameter, making this method unsuitable for the coating of finer structures in the nanosize regime.

Here a new method was developed for the synthesis of ZIF-8 thin films coatings electrochemically grown zinc oxide nanorod arrays. This method combines the advantages of using a molten linker for the formation of MOF thin films, allowing for the formation of ZIF-8 thin films in less than an hour using only an oven. Deposition of a thin film of the linker solution instead of using the linker powder allows for more control over the reaction and preserves the delicate nanorod morphology. Combined with electrochemical methods for the formation of the underlying zinc oxide nanorods, this method is fast, facile and inexpensive.

First, the formation of zinc oxide was optimized in order to grow uniform arrays of well-defined rods. Then, the synthesis of the ZIF-8 coating was examined with the aim of understanding the effect of the various synthesis conditions in order to optimize the growth of a uniform thin film. The effect of reaction time, the amount of linker, underlying zinc oxide morphology as well as the use of different solvents was studied. The result is the facile formation of defined zinc oxide rods, coated with a thin film of ZIF-8. The high surface area and molecular sieving abilities allow an increase in selectivity, a decrease in fouling and the ability to load ZIF-8 with additional catalyst particles [17, 53-55] The coatings prepared in this work can therefore find possible applications in catalysis, sensing and membrane technology.

2.2 Experimental

2.2.1 Chemicals and Materials

Zinc nitrate hexahydrate (99%), 2-methylimidazole (Hmin), Hexamethylenetetramine (HMT), Methanol and *N,N*-Dimethyl-formamide (DMF) were all obtained from Sigma-Aldrich. Fluorine-doped tin oxide glass (FTO) with a resistivity of ~7Ω/sq was obtained from Aldrich and cut into 1 cm x 2 cm pieces before use. Both the platinum coil counter electrode as well as the saturated Ag/AgCl reference electrode were obtained from BASi Inc.

2.2.2 Instrumentation

Samples were analysed using a JEOL JSM-6010LA scanning electron microscope and ImageJ software. X-ray diffraction analysis was performed using a Bruker D8 Advanced with a cobalt source. Electrochemical deposition was carried out using an Eco Chemie Metrohm AUT83987 Autolab potentiostat. When required, samples were heated using a Heraeus Intruments D-63450 oven.

2.2.3 Procedures and Methods

2.2.3.1 Electrochemical Deposition of Zinc Oxide Nanorod Array

Before zinc oxide deposition, pre-cut FTO glass plates were ultrasonicated in acetone, ethanol and deionized water for 10 minutes at a time. Copper tape was used to enable a connection between the potentiostat and the FTO glass. To define the surface area available for deposition, all but 1 cm^2 of FTO was masked using Teflon tape.

Zinc oxide deposition was carried out using 10 ml of an equimolar solution of zinc nitrate and HMT in deionized water. The concentrations of zinc nitrate and HMT were varied to examine their effect yet in all cases an equimolar concentration of the two precursors was used. A solution was kept at 70 °C using a water bath. A small magnetic stirrer was used to ensure uniform distribution of heat and starting materials. A three electrode setup was used with a saturated Ag/AgCl reference electrode, platinum coil counter electrode and FTO working electrode. The current was controlled using a potentiostat. Deposition was carried out for a predetermined amount of time until a specific total charge was reached. After deposition, the sample was rinsed thoroughly with de-ionized water and dried gently under nitrogen flow.

2.2.3.2 Synthesis of ZIF-8 Thin Film Coating

For the formation of ZIF-8, already grown zinc oxide rods (using 0.3 mA for 1.2 C) were used unless stated otherwise. A solution of linker with the desired concentration was obtained by dissolving Hmin in either methanol or DMF. Of this solution, 200 µL was deposited onto the zinc oxide coated FTO glass. and allowed to dry in ambient conditions. When using the pure linker, the powder was finely grounded beforehand with a mortar and pestle. In case an aluminium heating block was used, samples were placed in glass vials which were covered with a glass petri dish lid to ensure minimal loss of linker due to evaporation. When using an oven, the samples were covered with an hourglass and placed inside a closed Petri dish to reduce the risk of contamination when heating multiple samples simultaneously. The samples were then heated to a temperature of 150 °C for a designated amount of time. After ZIF-8 formation, the samples were allowed to cool before being thoroughly washed and soaked with the solvent used for linker dissolution to ensure full unreacted linker removal. Samples were then allowed to dry in air overnight.

2.2.3.3 Determination of ZIF-8 mass percentage

The mass ratios of ZIF-8 and zinc oxide were determined *via* XRD data using the PowderCell software. Quantitative results were obtained using the Rietveld refinement as described by Martin-Ramos *et al.*[56]

2.3 Results and Discussion

2.3.1 Synthesis of Zinc Oxide Nanorod Arrays

In ambient conditions, zinc oxide exists in the wurtzite crystal structure, shown in Figure 2.1. The structure can be described as alternating planes of tetrahedrally coordinated oxygen and zinc ions. The top (0002) plane is Zn^{2+} terminated and thus polar whereas the side planes are apolar [57]. The planes in the wurtzite crystal structure have a corresponding peak in the X-ray diffraction spectrum of zinc oxide, with the most important peaks corresponding to the planes shown in Figure 2.1. The relative intensity of these peaks gives information regarding the shape of the formed crystal, with an intense peak corresponding to the (0002) plane indicating increased growth in the c-axis and the formation of zinc oxide nanorods [57].

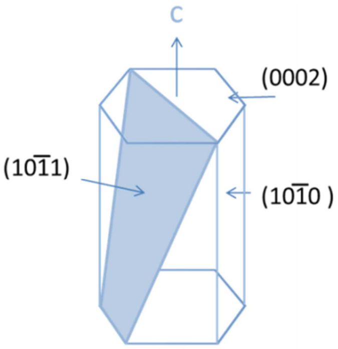

Figure 2.1. Schematic illustration of the zinc oxide crystal structure

The electrochemical synthesis of zinc oxide relies on the generation of OH^- species which react with the zinc ions in solution to form zinc hydroxide:

$$Zn^{2+} + 2OH^- \rightleftharpoons Zn(OH)_2 \qquad (1)$$

The zinc hydroxide formed is not stable at elevated temperatures and will subsequently transform into zinc oxide[57].

$$Zn(OH)_2 \overset{\Delta T}{\rightarrow} ZnO + H_2O \qquad (2)$$

Electrochemical formation of the OH^- species is carried out by the reduction of a precursor such as oxygen (O_2) and nitrates (NO_3^{2-}). The use of nitrates has the advantage that their solubility in water is higher and they can act as both the zinc and hydroxide source [57]:

$$NO_3^- + H_2O + 2e^- \longrightarrow NO_2^- + 2OH^- \quad (3)$$

The electrodeposition parameters such as current density or applied voltage chosen determine the rate of nitrate reduction and hence the rate of OH^- production. Tena-Zaera *et al.* have examined the effect of electrodeposition parameters on zinc oxide growth from nitrate solution [58]. It was found that the morphology of ZnO rods is governed by the rate of OH^-

production and two regimes have been identified. When the OH^- production rate is high, zinc oxide formation is limited by Zn^{2+} diffusion to the rods and growth along the c-axis is preferred, resulting in long, thin rods. However, when the diffusion rate of Zn^{2+} is equal to the OH^- production rate, growth both perpendicular and tangential to the substrate occurs and thicker rods are formed.

The use of equimolar concentrations of both zinc nitrate and HMT has been shown to yield long, defined rods [59, 60]. Traditionally used in hydrothermal synthesis [61-65], the role of HMT is unclear and multiple theories exist. It is known that at elevated temperatures, HMT hydrolyses to form formaldehyde and ammonia, which then yields OH^- moieties [66]:

$$(CH_2)_6N_4 + 6H_2O \rightleftharpoons 6HCHO + 4NH_3 \quad (4)$$

$$NH_3 + H_2O \rightleftharpoons NH_4^+ + OH^- \qquad (5)$$

Furthermore, HMT can also act as a pH buffer as its rate of hydrolysis slows down with increasing pH [64]. Finally, some argue the role of HMT as a non-polar chelating agent, attaching to all but the (0002)-plane and promoting growth in the c-axis [62, 67-69].

To ensure the growth of well-defined rods, zinc nitrate and HMT were used in equimolar concentrations. A constant current was used so as to control the total charge transferred during deposition. The effects of current density and total charge transfer were examined in order to understand their effect in the formation of long, well-defined, homogenous zinc oxide nanorods.

2.3.1.1 The Effect of Current Density

The current density controls the OH^- production rate and therefore plays an important role in the resulting zinc oxide morphology. If the current density is too low, thick rods with a random orientation are formed. It is therefore important to establish at which current density well-defined rods are ontained. An equimolar solution of zinc nitrate and HMT was used with a concentration of 0.01 M, The total charge transfer density was kept constant at 1.2 C. As shown in Figure 2.2, a high intensity in the peak corresponding to the (0002) plane is observed for all current densities used, indicating preferential crystal growth along the c-axis. Increase in the current density results in an increase in this preferential growth. Furthermore, the SEM images (See Figure 2.3) show the formation of thinner rods when increasing the current density. These observations are in agreement with previous reports as an increase in current density results in a higher OH^- production rate and hence thinner [58] rods with higher orientation in the c-axis [70, 71]. Interestingly, the rods grown at 0.3 mA show a more defined hexagonal morphology, with the rods grown at higher current densities being more rounded .

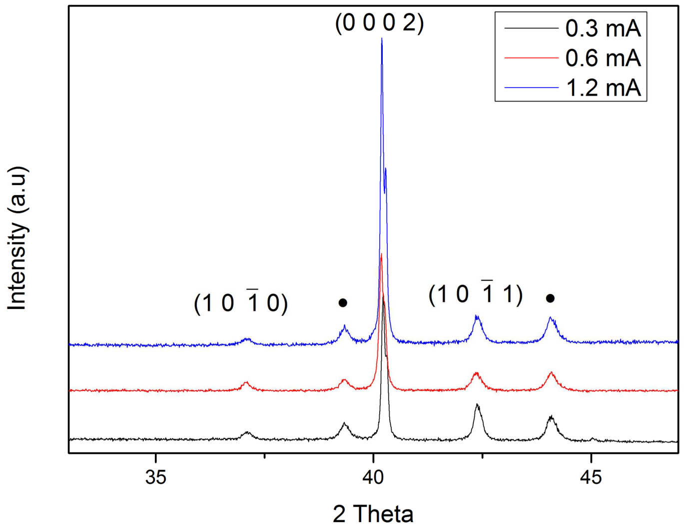

Figure 2.2. XRD data showing the effect of current density on zinc oxide crystal growth. FTO diffraction peaks are marked by •.

2.3.1.2 The Effect of Concentration

Next to current density, the concentration of zinc nitrate and hexamine also play an important role in obtaining well-defined nanorods. To understand this effect more, the total concentration of the solution was changed while keeping zinc nitrate and HMT in equimolar amounts. Having established that a current density of 0.3 mA and a total charge transfer density of 1.2 C yield well-defined, hexagonal zinc oxide nanorods, these conditions were used once more. Both the resulting XRD data (Figure 2.4) and SEM images (Figure 2.5) show that crystalline zinc oxide is barely formed at the lowest concentration (0.001 M) while increase in concentration to 0.005 M and 0.01 M results to the formation of films with similar crystal orientation in the c-axis. However, the rods formed using a precursor concentration of 0.01 M appear longer and more hexagonal when examined using SEM. Finally, using a precursor concentration of 0.05 M results in the formation of thick rods with random crystal orientations, confirmed by both XRD and SEM. Larger crystals growing in random orientations on top of the nanorods are also observed This effect was reported before and was attributed to the faster diffusion of Zn^{2+} to all sides of the zinc oxide nanorods at higher concentration resulting in the growth of thicker, more randomly oriented rods [69, 72]. From this it was established that a solution concentration of 0.01 M zinc nitrate and HMT yields the best results.

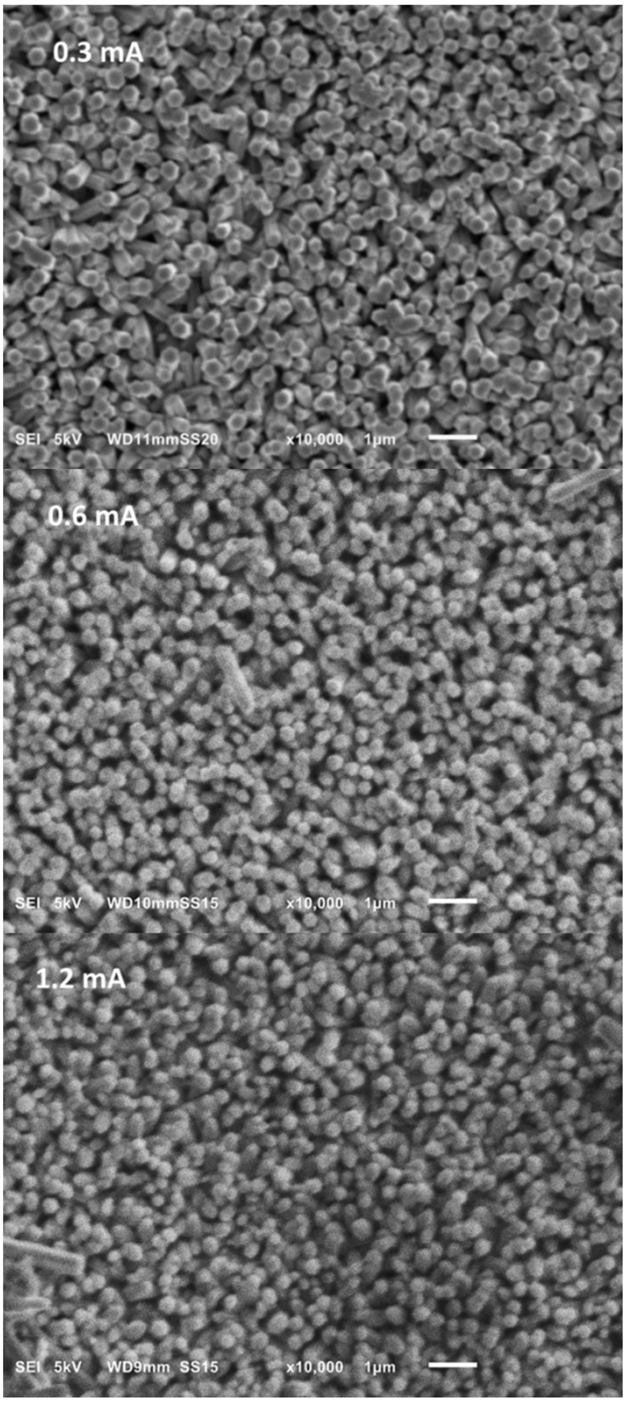

Figure 2.3. SEM images showing the effect of current density on zinc oxide morphology for 0.3 mA, 0.6 mA and 1.2 mA while the charge was kept constant at 1.2 C.

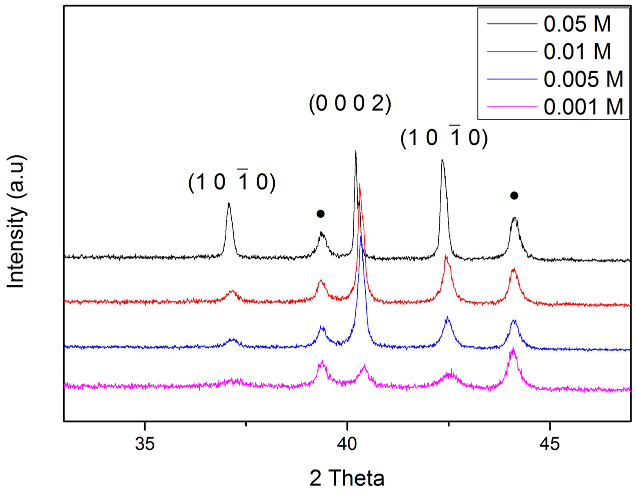

Figure 2.4. XRD data showing the effect of precursor concentration on zinc oxide crystal growth. FTO diffraction peaks are marked by •.

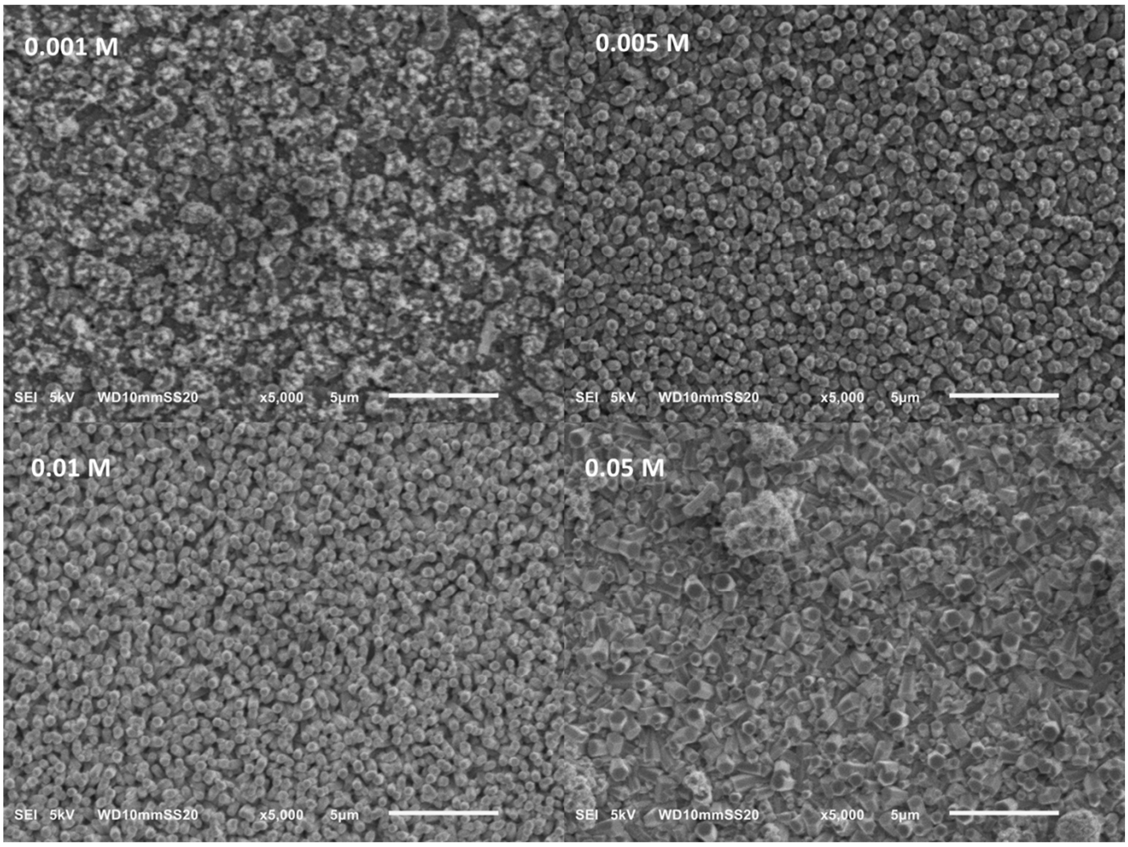

Figure 2.5. SEM images showing the effect of precursor concentration on zinc oxide morphology.

2.3.1.3 The Effect of Deposition Time

The effect of deposition time was examined in order to understand the change in rod morphology over time. Having established that an equimolar solution concentration of 0.01 M zinc nitrate and HMT yield the most well-defined rods, this concentration was used once more. Furthermore, the interesting results obtained when using a solution concentration of 0.05 M prompted further investigation into the evolution of this system over time. In order to compare the results to those obtained when varying the concentration, a current density of 0.3 mA was used. In both cases, an increase in the deposition time resulted in an increase in the crystal orientation in the (0002) plane, as shown in Figure 2.6. Interestingly, this effect seems more pronounced when using a concentration 0.05 M.

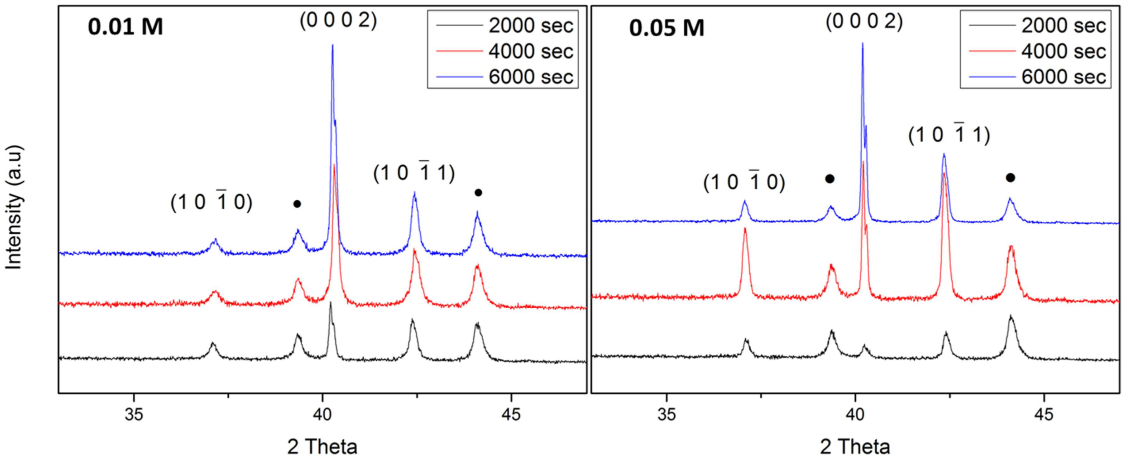

Figure 2.6. XRD data showing the effect of deposition time on zinc oxide crystal growth. FTO diffraction peaks are marked by •.

The SEM images shown in Figure 2.7 indicate the same trend as the XRD data. Furthermore it can be observed that in when using a concentration of 0.01 M, the rod diameter seems to increase only slightly over time. This observation is in agreement with the theory developed by Tena-Zaera *et al.* who showed that at high OH^- production rate, rods maintain the same diameter with increasing the deposition time as growth occurs mainly along the c-axis [58]. The case for a concentration of 0.05 M is less straightforward, with rods showing a lower nucleation density at 2000 seconds, resulting in the formation of only a few relatively large rods. As deposition time is increases, these rods grow in diameter while additional smaller rods start appearing. Finally, the larger rods cease to grow in diameter, allowing the smaller rods to 'catch up', with many rods agglomerating. Lu *et al.* observed that increase in deposition time results in a depletion of Zn^{2+} ions from solution [73]. This limits diffusion of Zn^{2+}, causing rods to elongate without increasing in diameter. Interestingly, the SEM images indicate that the smaller rods still show some increase in diameter.

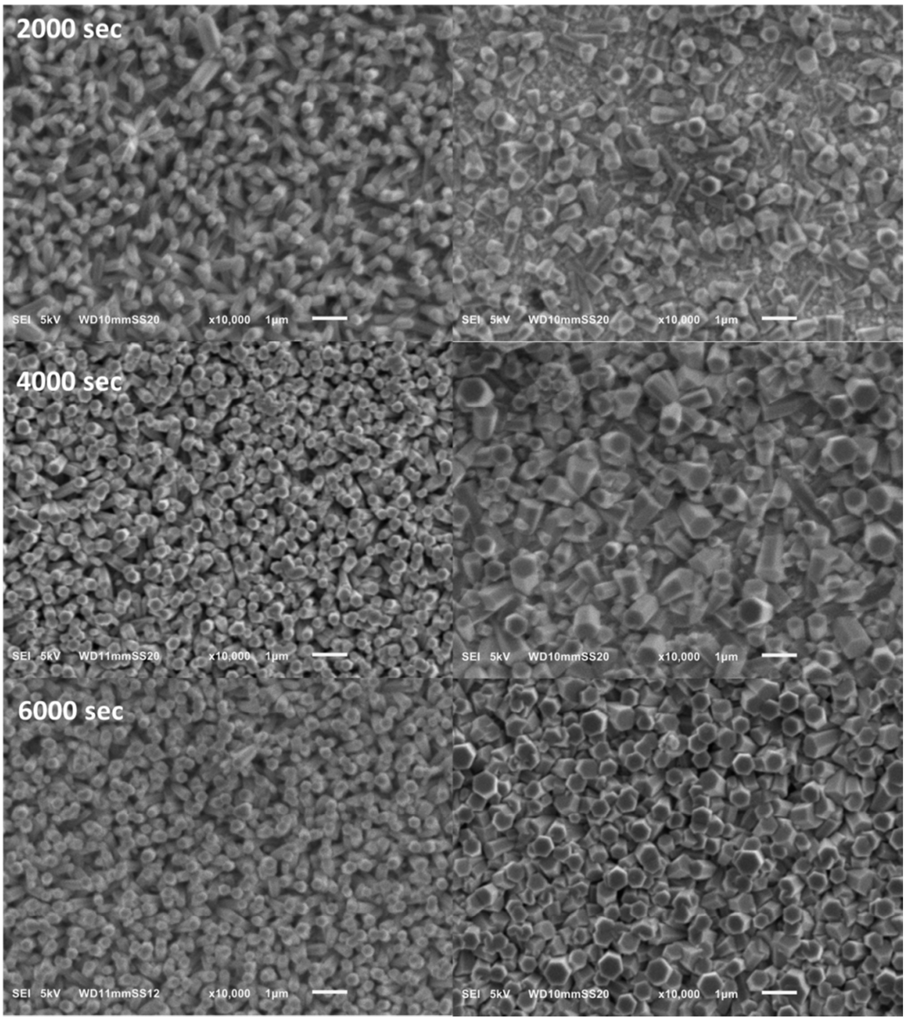

Figure 2.7. SEM images showing the effect of deposition time on zinc oxide morphology. The precursor concentrations were 0.01 M (left) and 0.05 M (right).

2.3.2 Synthesis of ZIF-8 Thin Film Coating

The formation of a ZIF-8 thin film on the zinc oxide rods depends on a reaction between zinc oxide and the molten 2-methyl imidazole (Hmin) linker. In order to control the amount of linker present during the reaction as well as ensure a more thorough coverage of the zinc oxide nanorods, a thin layer of the linker was cast on top of the formed zinc oxide rods. This was performed by dissolving the linker in either methanol or DMF and depositing a known quantity of this solution onto the zinc oxide. The solvent was then allowed to evaporate under ambient conditions in order to yield a thin layer of solid linker.

The formation of MOFs using molten linker is an emerging method. Synthesis is based on an acid-base reaction between the oxide and the linker, yielding water as the only side-product [50].

$$ZnO \ + 2\ Hmin \ \rightarrow Zn(Hmin)_2 + H_2O \quad (6)$$

Whereas theories have been presented on the nucleation behaviour of ZIF-8 in solution [28, 74-76] the nucleation behaviour of ZIF-8 in the present system has not yet been examined to such a degree. Regarding MOFs grown using oxides, Kitagawa *et al.* examined the formation of MIL-53 through alumina dissolution and recognized a coupled dissolution-precipitation mechanism [77]. Known to occur during the formation of minerals in the earth's crust, this type of reaction involves the dissolution of the solid parent phase into the liquid and subsequent precipitation of a newly formed daughter phase which catalysed further dissolution of the parent phase [78]. The result is an inward growing daughter phase. Falcaro *et al* observed this coupled dissolution-precipitation mechanism in the transformation of $Cu(OH)_2$ nanotubes into HKUST-1 and recognized three reaction phases [79]. First of all, nucleation of MOF crystals occurs through a dissolution-precipitation mechanism, resulting in a roughening of the nanotube surface. This is followed by a period of crystal growth, resulting in the appearance of larger, more defined crystals covering the surface of the nanotubes. Finally, these crystals continue to grow due to Ostwald ripening, consuming the $Cu(OH)_2$ until the nanotube morphology disappears.

Zheng *et al.* investigated the formation of ZIF-8 on zinc oxide nanorods in an solution of Hmin in DMF and water [17]. Initially, small crystals were observed on the zinc oxide surface. An increase in time resulted in the formation of a ZIF-8 film and increasingly thinner rods, indicating inward growth of the ZIF-8 thin film. This growth was shown to slow down after a certain time, indicating that the diffusion of Hmin through the pores of the formed ZIF-8 decreases. Furthermore, it was shown that by varying the DMF-to-water ratio, the zinc oxide dissolution rate and hence the ZIF-8 formation rate could be controlled. Unlike the effect of synthesis time, an increase in dissolution rate results in complete consumption of zinc oxide and the formation of large crystals as well as a dense, non-porous dia-phase instead of ZIF-8. When using the molten linker approach to form ZIF-8, Ameloot *et al.* observed that an increase in the amount of zinc oxide resulted in the formation of larger ZIF-8 crystals, implying that the amount of zinc oxide or linker available for the reaction influences the rate of zinc dissolution and hence the rate of reaction [52]. Even though the observations mentioned above were obtained for different systems, they help in understanding the formation of ZIF-8 in this work. The reaction time is important and must be long enough to grow a thin film but not so long as to lose the nanomorphology due to Ostwald ripening or the complete consumption of the zinc oxide rods. Furthermore, the reaction rate must be controlled. The amount of linker deposited onto the zinc oxide as well as the amount of zinc oxide in contact with the linker is therefore important. As mentioned before, zinc oxide has a polar top plane and apolar side planes. The use of a more apolar solvent would allow more linker to cover the sides of the nanorods, influencing the rate of reaction. Zinc oxide nanorods provide nucleation sites around which the ZIF-8 film can grow and spread [80]. Hence, the morphology of the underlying zinc oxide can influence the amount of nuclei formed and the way they spread. Finally, Román *et al.* observed that when converting zinc oxide powder into ZIF-8 using a molten linker, a high heating rate resulted in the formation of smaller, less crystalline particles [51]. These observations highlight the importance of practical aspects, such as heating rate or heating technique.

2.3.2.1 The Effect of Heating Technique

Both the rate of heating as well as heating method affected the ZIF-8 morphology. Heating rate had a more significant effect as shown in Figure 2.8 A -B. While heating the sample from room temperature to 150 ^{o}C slowly yield ZIF-8 crystals , placing the sample in a heating block already pre-heated to 150 ^{o}C yields a layer with crater-like morphology that has, to the knowledge of the authors never been observed before. Román *et al.* observed an increase in crystallinity and crystal size with lower heating rate [51], but not the formation of the craters seen in this study.

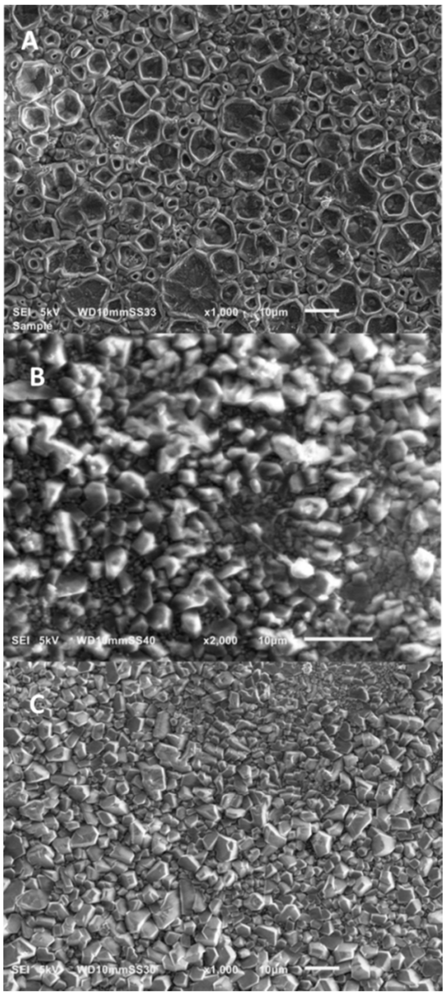

Figure 2.8. SEM inages showing the effect of heating technique on ZIF-8 morphology with heaitng in a heating block set at 150 °C beforehand (A), heating in heating block set heated to 150 °C after sample placement (B) and heating in oven set at 150 °C after sample placement (C).

The difference between using a heating block and an oven were also examined (See Figure 2.8 B-C). The use of an oven results in crystals with a more narrow size distribution. This can be explained by taking linker evaporation into account. When using a heating block, samples were placed inside vials. During ZIF-8 synthesis, a large temperature gradient develops along these vials, with the bottom being much warmer than the top. The linker will therefore evaporate and sublimate on the top of the vial, effectively being lost to the reaction. Use of an oven results in a more even temperature distribution. Furthermore, using an hourglass and petridish allow for the linker to be confined within the close vicinity of the zinc oxide (See Figure 2.9). The use of an oven was therefore maintained throughout the rest of the work.

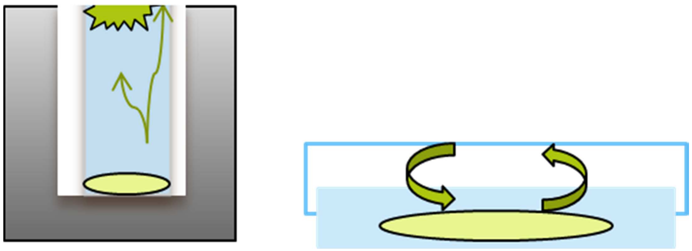

Figure 2.9. Schematic illustration of the effect of a heating block (left) and oven (right) on linker evaporation.

2.3.2.2 The Effect of Linker Amount

To preserve the nanorod morphology of the underlying zinc oxide layer, a thin layer of linker was deposited into the zinc oxide. Using a linker layer instead of pure linker powder is thought to provide a more even coverage of the nanorods as well as provide more control over the reaction. To test this theory, the use of a deposited thin layer of linker was compared to the use of pure linker powder. Furthermore, in order to optimize ZIF-8 thin film formation and understand the reaction taking place, the amount of linker deposited was varied. This was done by using linker solutions of different concentrations in methanol. The reaction time was kept at 20 minutes. The effect of the amount of linker on the crystallinity of the ZIF-8 phase formed, along with the calculated mass percentage is given in Figure 2.10. A small yet steady increase in the XRD peaks corresponding to the ZIF-8 phase was observed with increasing concentration; however the calculated weight percentage indicates that this increase is minor. It must be noted that the loss of linker due to evaporation during synthesis as well removal of larger crystals during the washing afterwards could influence the final ZIF-8 weight percentage. Also, the concentration of linker could the hydrophobicity and surface tension of the solutions used to cast the thin linker film and also affect the results. Interestingly, the pure linker powder yields the lowest weight percentage. This is thought to be due to the inhomogeneous spreading of the pure linker powder and failure of the powder to fully cover the nanorods, causing MOF formation only in some areas.

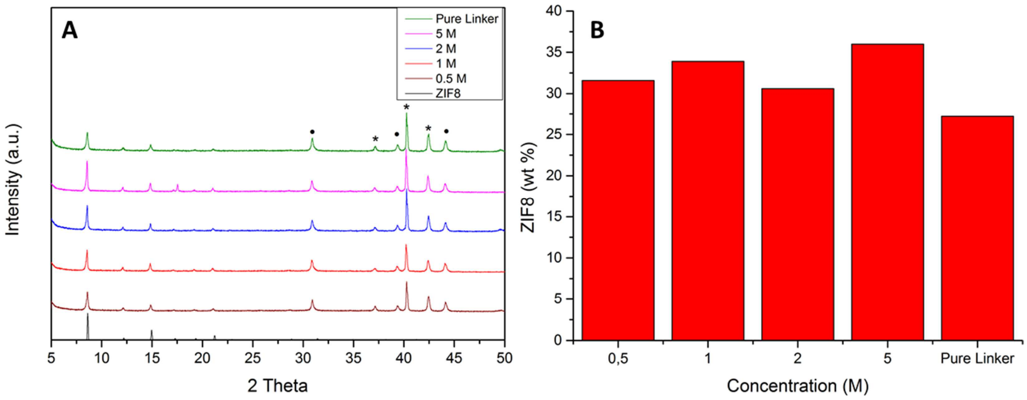

Figure 2.10. XRD spectra (A) and calculated ZIF-8 weight percentage (B) showing the effect of linker amount on ZIF-8 formation. The FTO substrate and ZnO peaks are indicated with • and *, respectively.

The SEM images shown in Figure 2.11 show a significant change between the use of a thin linker film as opposed to a pure linker powder. Pure linker powder results in a MOF film on top of the rods with inhomogeneous sized crystals, consistent with previous observations[52]. However, the use of a deposited linker film allows the nanorod morphology to be maintained, indicating the growth of a thin MOF-film. The inhomogeneity of the coating of MOF using pure linker compared to coating obtained using a 2 M linker solution is shown clearly in Figure 2.12.

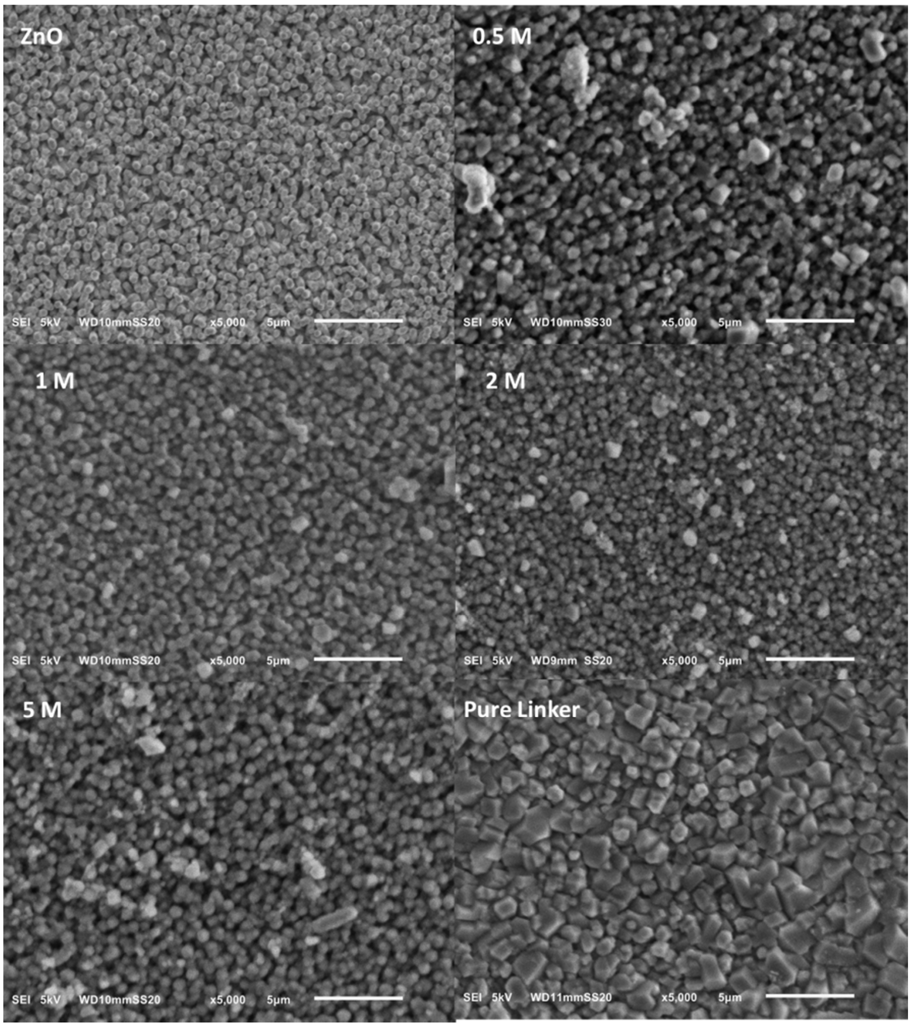

Figure 2.11. SEM images showing the effect on linker amount on ZIF-8 morphology.

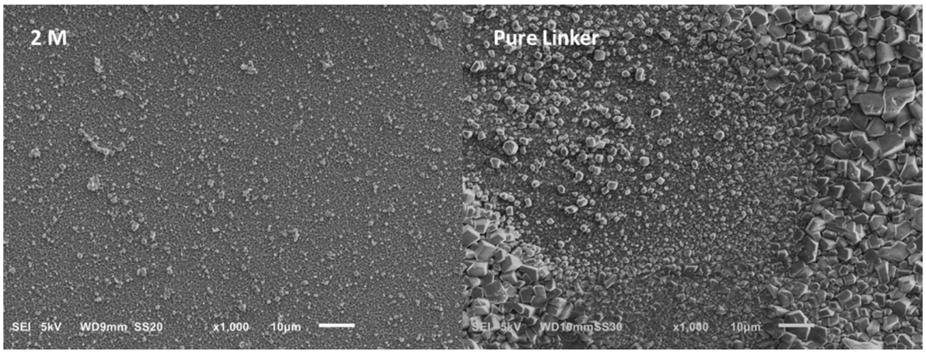

Figure 2.12. SEM image showing the inhomogeneity when using a pure linker.

2.3.2.3 The Effect of Reaction Time

The use of molten linkers for the synthesis of MOFs is relatively new. Hence, much is still unknown about the crystallisation behaviour of ZIF-8 when using this method. By examining the effect of reaction time, more insight into the crystallisation of ZIF-8 could be obtained. The effect of reaction time was examined for a linker concentration of 2 M in methanol. Figure 2.13 shows the effect of reaction time on the crystal ZIF-8 phase and weight percentage. Increase in reaction time indicates an increase in the ZIF-8 phase, with this increase being larger at lower reaction times. This behaviour has been observed before when using zinc oxide [17, 52] as well as zinc ions in a solution of linker [28, 74, 75] and has been attributed to the rapid growth of formed ZIF-8 crystal nuclei [28]. The weight percentage seems to stabilize after 20 minutes, indicating no more zinc oxide is consumed after this time.

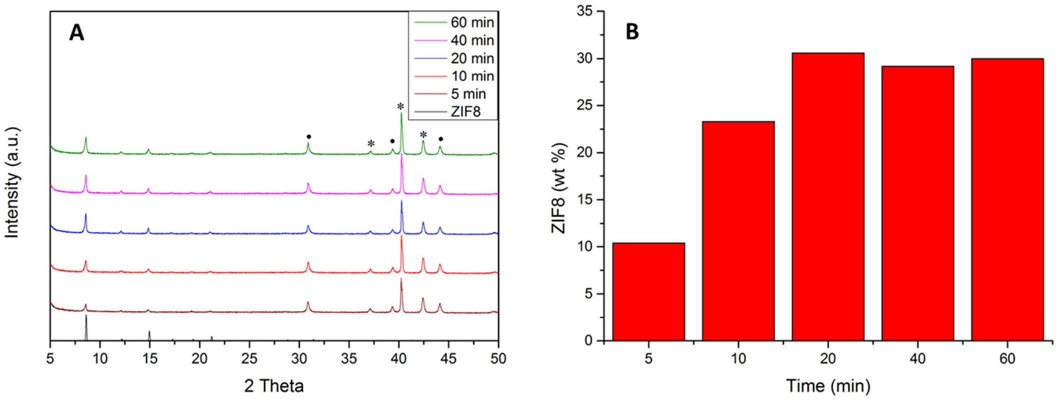

Figure 2.13. XRD spectra (A) and calculated ZIF-8 weight percentage (B) showing the effect of synthesis time on ZIF-8 formation. The FTO substrate and ZnO peaks are indicated with • and *, respectively.

The SEM images shown in Figure 2.14 indicate that nanorod morphology is maintained throughout the synthesis and appears to become more defined with increasing reaction time. Unfortunately, an increase in reaction time seems to also affect the growth of larger crystals on top. As there is almost no change in weight percentage of ZIF-8, the formation of these larger crystals can be largely attributed to Ostwald ripening.

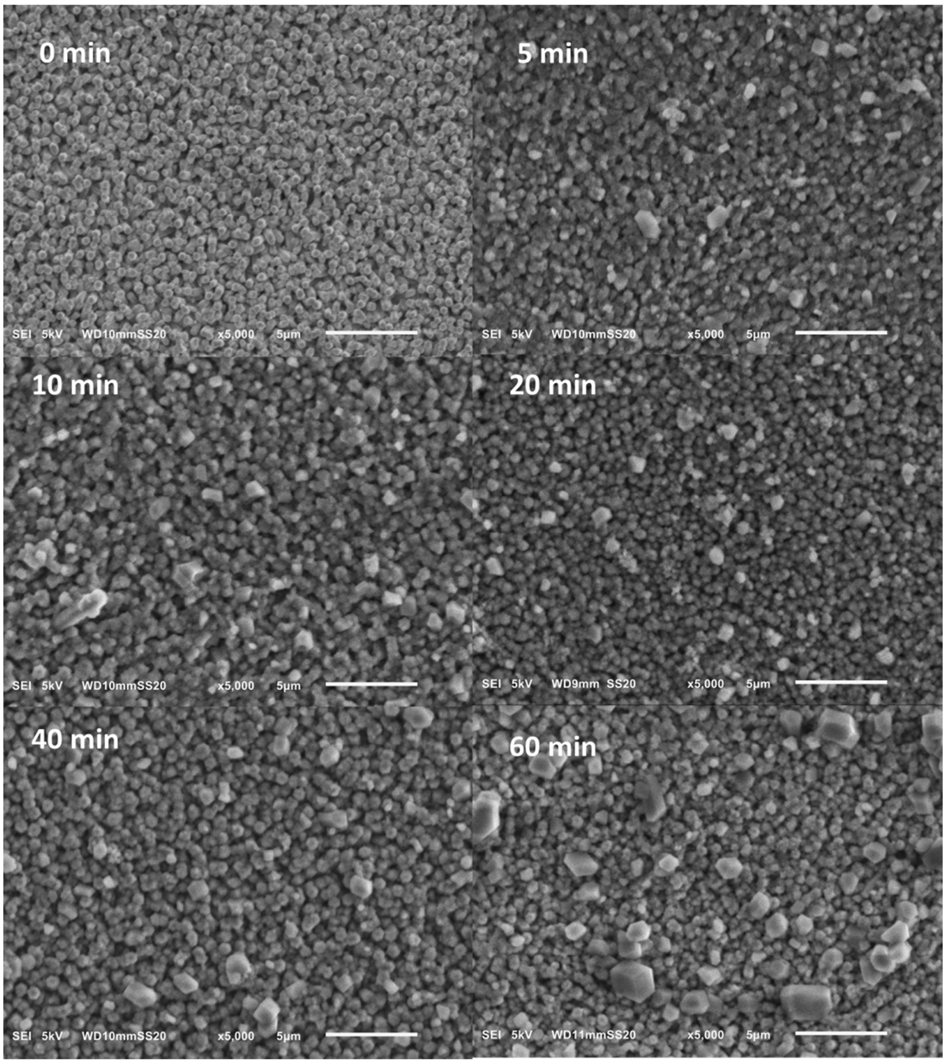

Figure 2.14. SEM images showing the effect of reaction time in ZIF-8 morphology.

TO examine the morphology of the formed ZIF-8 thin film in greater detail, FE-SEM images were obtained. Given in Figure 2.15, they reveal that after 40 minutes, the zinc oxide nanorods are fully coated with a thin film of ZIF-8. More interestingly, this film appears to extend down to the base of the zinc oxide rods, covering them completely.

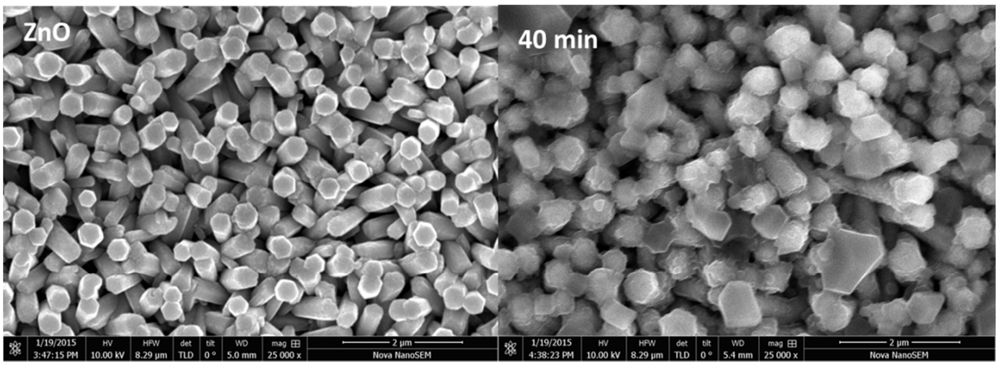

Figure 2.15. SEM images showing the zinc oxide nanorod array and the formed ZIF-8 layer after 40 minutes when using a 2 M solution in methanol.

2.3.2.4 The Effect of Solvent

It was established that a thin linker layer allows zinc oxide nanorods to be coated in a ZIF-8 thin film while maintaining their morphology. To deposit this thin layer of linker, a solution of linker in methanol was used. A small amount of this solution was deposited onto the zinc oxide nanorods and the solvent was allowed to evaporate. As mentioned before, zinc oxide possesses a polar top plane and apolar side planes, implying that the polarity of the solvent used to deposit the thin linker layer could affect the coverage the nanorods. It is known that DMF has a larger surface tension and a more apolar nature compared to methanol. Thus DMF would allow more linker to be retained onto the substrate and accordingly a more thorough coverage of the zinc oxide nanorods. To examine the effect of solvent, a 2 M solution of the linker in DMF was used. As can be seen in Figure 2.16, the effect of reaction time when using DMF is different from methanol. An increase in the ZIF-8 weight percentage at shorter synthesis times is seen in both cases. However, this increase is much less significant when using DMF and could indicate different crystal growth mechanics [75].

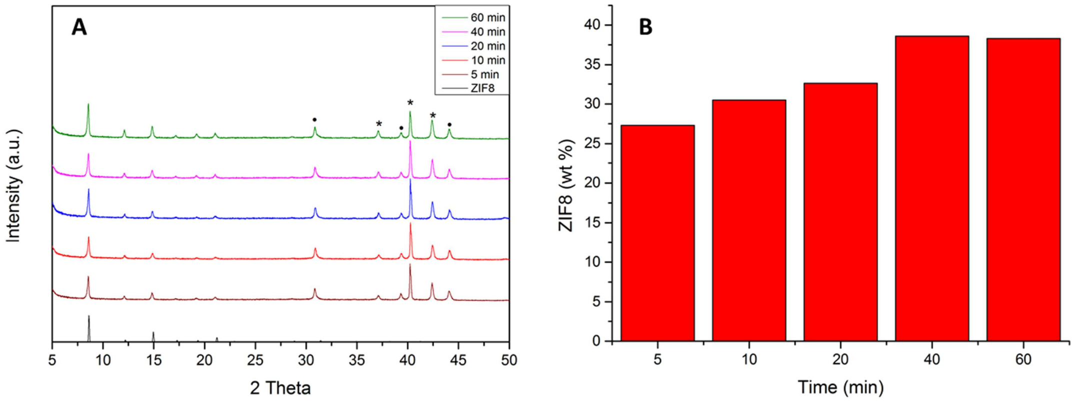

Figure 2.16. XRD spectra (A) and calculated ZIF-8 weight percentage (B) showing the effect of synthesis time on ZIF-8 formation when DMF is used for linker dissolution. The FTO substrate and ZnO peaks are indicated with • and *, respectively.

The differences in reaction progression are also clearly evident in Figure 2.17. Whereas with methanol, the nanorod morphology was maintained throughout the reaction, this is not the case when using DMF. Large crystals were observed coating the surface. The change in crystal morphology appears to be similar to previous observations [52, 74, 76], as small cubic crystals seem to grow in size and become more truncated. The increase in crystal size, coupled with a decrease in the amount of crystals indicates the presence of Ostwald ripening. However, a steady increase in ZIF-8 weight percentage indicates that crystal growth at the expense of zinc oxide still occurs until a reaction time of 40 minutes.

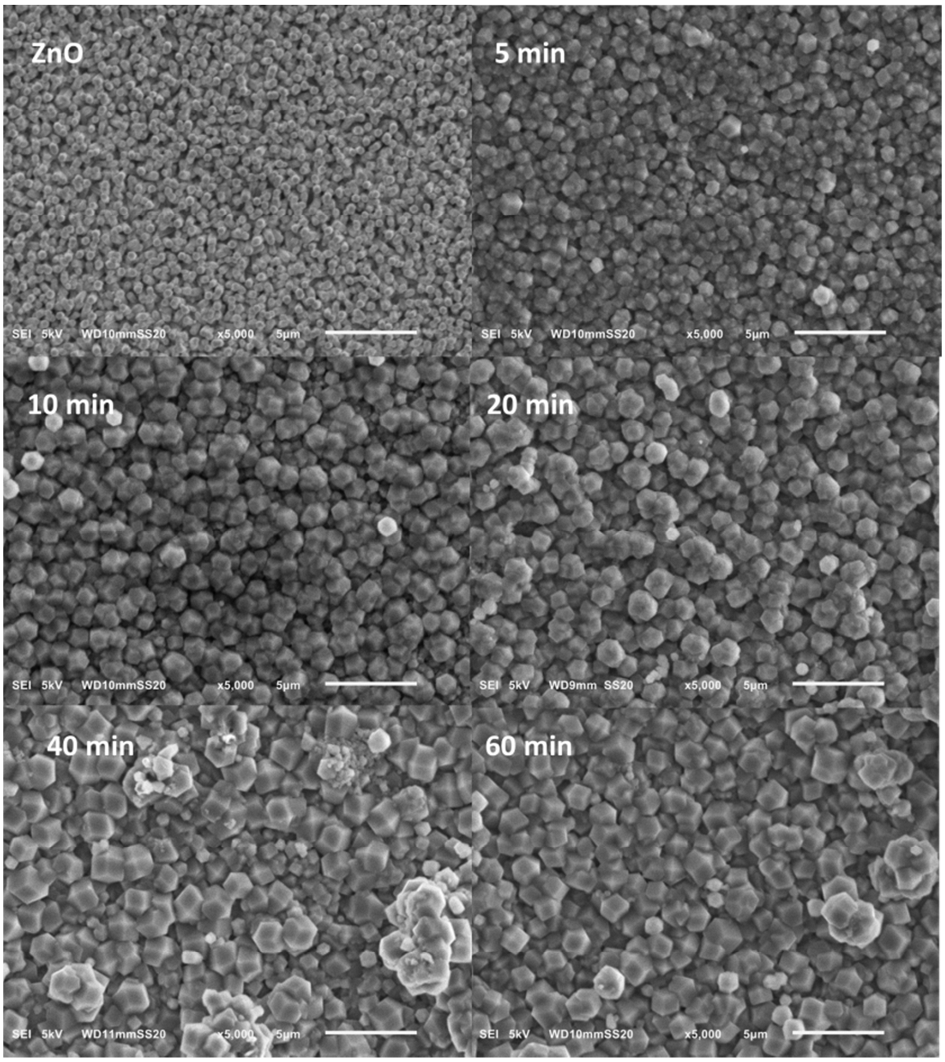

Figure 2.17. SEM images showing the effect of reaction time on ZIF-8 morphology while using DMF as a solvent. Linker concentration was 2 M.

Ameloot *et al.* observed that an increase in the film thickness of a flat zinc oxide layer resulted in the formation of larger ZIF-8 crystals on top of the layer [52]. The use of DMF could result in more linker being retained resulting in a much faster reaction and hence the growth of larger crystals. Furthermore, the incomplete removal of DMF must be taken into account. It is known that DMF itself can decompose thermally, yielding formate and dimethylamine which can act as deprotonating agents and increase the rate of ZIF-8 formation. Furthermore, DMF can also interact with both linker and metal However, it must be said that DMF decomposition is very slow with 3.3% decomposing after 33 h at 100 ˚C and the interactions of DMF mentioned are known to slow down nucleation and would result in the opposite of what is observed here [75].

To understand the observed effect more, a 0.5 M linker solution in DMF was used. The results, shown in Figure 2.18 show that at lower linker concentrations, a morphology similar to that obtained when using methanol is seen. However, an increase presence of larger crystals indicates that the properties of DMF could contribute to their formation.

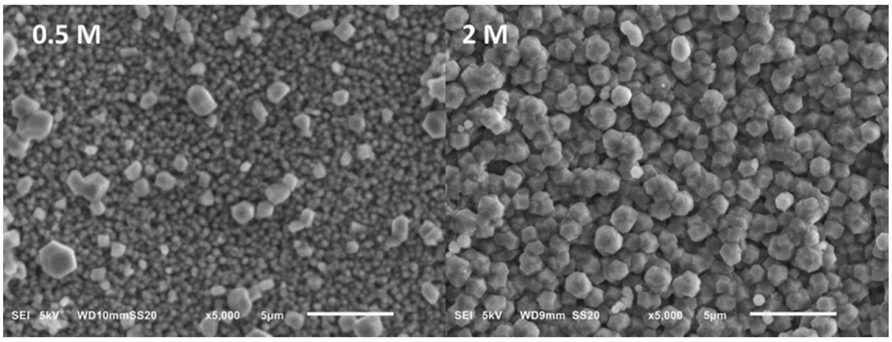

Figure 2.18. SEM images showing the effect of linker concentration in DMF on ZIF-8 morphology

2.3.2.5 The Effect of Difference in Zinc Oxide Morphology

As shown in section 2.3.1, the morphology of the zinc oxide nanorods can easily be changed by alteration of the deposition conditions. Before, zinc oxide rods were formed by using an equimolar aqueous solution of zinc nitrate and HMT with a concentration of 0.01 M and a total charge transfer density of 1.2 C. By altering these conditions, the morphology of the underlying zinc oxide can be examined. The effect of the length of the zinc oxide rods was studied by increasing the total charge transfer density to 2.4 C while keeping the concentration constant. The effect of rod diameter was investigated by increase in solution concentration to 0.05 M while keeping the total charge transfer density constant. To form ZIF-8, a 2 M methanolic linker solution was used and synthesis time was kept at 20 minutes. The results, shown in Figure 2.19 show an increase in the formation of larger ZIF-8 crystals in both cases. This is in agreement with the results obtained by Ameloot *et al.* [52] as more zinc oxide is present in both cases. However, it is interesting to note that while an increase in rod length results in the formation of larger crystals, increase in rod diameter results in a larger amount of both larger and smaller crystals. Huo *et al.* have shown that ZIF-8 nucleation occurs preferably on polar surfaces [81], being the (0002) plane in the case of zinc oxide. An increase in rod diameter and hence in the surface area of this polar plane would allow more ZIF-8 nuclei to form on the same plane, leading to an increase in the formation of small crystals. Furthermore, due to the random orientation of the rods formed at higher concentration, more surface area is exposed for reaction, also causing the formation of more and larger crystals.

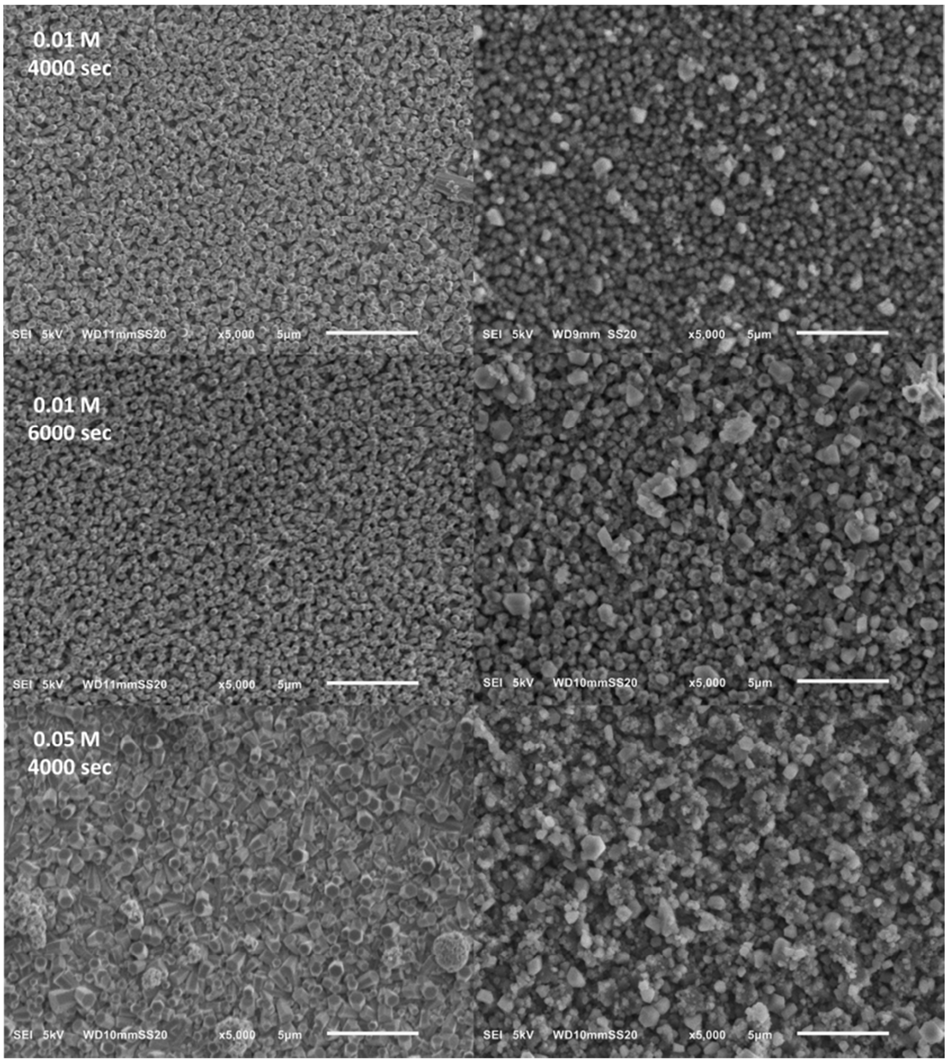

Figure 2.19. SEM images showing the effect of the underlying zinc oxide morphology (left) on the formation of ZIF-8 (right).

2.4 Conclusion and Outlook

The formation of a ZIF-8 thin layer on nanostructured zinc oxide was demonstrated using a new approach. By using a thin film of linker solution as opposed to linker powder, the morphology of the underlying zinc oxide was preserved and more control over the reaction was achieved. This new method allows for the formation of nanostructured thin films in a fast and facile manner, while minimizing the use of both solvents and linker. It was shown that the heating rate has a remarkable effect on the morphology of ZIF-8. High heating rates result in the formation of a ZIF-8 film with a novel, crater-like morphology. Furthermore, an increase in the synthesis time results in the formation of more defined ZIF-8 coated rods. However, the growth of large crystals on top of the nanorod array is also seen to increase and is thought to be due to Ostwald ripening. The use of DMF as a solvent resulted in the formation of a film consisting of ZIF-8 particles with a tuneable size and morphology. Finally, difference in the underlying zinc oxide nanorod morphology led to a change in crystallisation behaviour

The technique presented in this work is versatile and can be applied to other metal oxide nanostructures and metal organic frameworks. Furthermore, this type of hybrid material can be used in a variety of applications such as membrane technology, sensing and catalysis. However, it must be stated that this method is novel and much it still unknown regarding the crystallisation kinetics. Understanding these kinetics would not only lead to more insight into this method but could also allow for ways to reduce the growth of larger crystals on the surface of the rods. Finally, the porosity of the formed film must be examined to enable its use for further applications.

2.5 References

1. Q.-L. Zhu and Q. Xu, *Chemical Society Reviews*, 2014, **43**, 5468-5512.
2. K. Sugikawa, S. Nagata, Y. Furukawa, K. Kokado and K. Sada, *Chemistry of Materials*, 2013, **25**, 2565-2570.
3. X. Lin, G. Gao, L. Zheng, Y. Chi and G. Chen, *Anal Chem*, 2013, **86**, 1223-1228.
4. H. Hosseini, H. Ahmar, A. Dehghani, A. Bagheri, A. R. Fakhari and M. M. Amini, *Electrochimica Acta*, 2013, **88**, 301-309.
5. G. Lu, S. Li, Z. Guo, O. K. Farha, B. G. Hauser, X. Qi, Y. Wang, X. Wang, S. Han, X. Liu, J. S. DuChene, H. Zhang, Q. Zhang, X. Chen, J. Ma, S. C. J. Loo, W. D. Wei, Y. Yang, J. T. Hupp and F. Huo, *Nat Chem*, 2012, **4**, 310-316.
6. C. Wang, K. E. deKrafft and W. Lin, *Journal of the American Chemical Society*, 2012, **134**, 7211-7214.
7. Q.-L. Zhu, J. Li and Q. Xu, *Journal of the American Chemical Society*, 2013, **135**, 10210-10213.
8. F. Ke, Y.-P. Yuan, L.-G. Qiu, Y.-H. Shen, A.-J. Xie, J.-F. Zhu, X.-Y. Tian and L.-D. Zhang, *J Mater Chem*, 2011, **21**, 3843-3848.
9. C. Rosler and R. A. Fischer, *CrystEngComm*, 2015.
10. H. R. Moon, D.-W. Lim and M. P. Suh, *Chemical Society Reviews*, 2013, **42**, 1807-1824.
11. Y. Liu and Z. Tang, *Advanced Materials*, 2013, **25**, 5819-5825.
12. K. Koh, A. G. Wong-Foy and A. J. Matzger, *Chemical Communications*, 2009, 6162-6164.
13. O. Shekhah, J. Liu, R. Fischer and C. Wöll, *Chemical Society Reviews*, 2011, **40**, 1081-1106.
14. K. S. Park, Z. Ni, A. P. Côté, J. Y. Choi, R. Huang, F. J. Uribe-Romo, H. K. Chae, M. O'Keeffe and O. M. Yaghi, *Proceedings of the National Academy of Sciences*, 2006, **103**, 10186-10191.
15. Y. Pan, Y. Liu, G. Zeng, L. Zhao and Z. Lai, *Chemical communications*, 2011, **47**, 2071-2073.
16. G. Lu and J. T. Hupp, *Journal of the American Chemical Society*, 2010, **132**, 7832-7833.
17. W.-w. Zhan, Q. Kuang, J.-z. Zhou, X.-j. Kong, Z.-x. Xie and L.-s. Zheng, *Journal of the American Chemical Society*, 2013, **135**, 1926-1933.
18. S. Liu, Z. Xiang, Z. Hu, X. Zheng and D. Cao, *Journal of Materials Chemistry*, 2011, **21**, 6649-6653.
19. C. Chizallet, S. Lazare, D. Bazer-Bachi, F. Bonnier, V. Lecocq, E. Soyer, A.-A. Quoineaud and N. Bats, *Journal of the American Chemical Society*, 2010, **132**, 12365-12377.
20. U. P. Tran, K. K. Le and N. T. Phan, *ACS Catalysis*, 2011, **1**, 120-127.
21. C. M. Miralda, E. E. Macias, M. Zhu, P. Ratnasamy and M. A. Carreon, *ACS Catalysis*, 2011, **2**, 180-183.
22. I. B. Vasconcelos, T. G. da Silva, G. C. Militão, T. A. Soares, N. M. Rodrigues, M. O. Rodrigues, N. B. da Costa, R. O. Freire and S. A. Junior, *RSC Advances*, 2012, **2**, 9437-9442.
23. N. Liédana, A. Galve, C. Rubio, C. Téllez and J. Coronas, *ACS Applied Materials & Interfaces*, 2012, **4**, 5016-5021.
24. C.-Y. Sun, C. Qin, X.-L. Wang, G.-S. Yang, K.-Z. Shao, Y.-Q. Lan, Z.-M. Su, P. Huang, C.-G. Wang and E.-B. Wang, *Dalton Transactions*, 2012, **41**, 6906-6909.
25. J. Zhuang, C.-H. Kuo, L.-Y. Chou, D.-Y. Liu, E. Weerapana and C.-K. Tsung, *ACS Nano*, 2014, **8**, 2812-2819.

26. H. Bux, C. Chmelik, R. Krishna and J. Caro, *Journal of Membrane Science*, 2011, **369**, 284-289.
27. Y. Pan and Z. Lai, *Chem. Commun.*, 2011, **47**, 10275-10277.
28. S. R. Venna, J. B. Jasinski and M. A. Carreon, *Journal of the American Chemical Society*, 2010, **132**, 18030-18033.
29. J. Yao and H. Wang, *Chemical Society Reviews*, 2014, **43**, 4470-4493.
30. M. Shah, H. T. Kwon, V. Tran, S. Sachdeva and H.-K. Jeong, *Microporous and Mesoporous Materials*, 2013, **165**, 63-69.
31. Z. Fan and J. G. Lu, *Journal of nanoscience and nanotechnology*, 2005, **5**, 1561-1573.
32. Z. Li, R. Yang, M. Yu, F. Bai, C. Li and Z. L. Wang, *The Journal of Physical Chemistry C*, 2008, **112**, 20114-20117.
33. M. Willander, *Zinc Oxide Nanostructures: Advances and Applications*, CRC Press, 2014.
34. Z. L. Wang, *Materials Today*, 2004, **7**, 26-33.
35. S. K. Arya, S. Saha, J. E. Ramirez-Vick, V. Gupta, S. Bhansali and S. P. Singh, *Analytica chimica acta*, 2012, **737**, 1-21.
36. Ü. Özgür, Y. I. Alivov, C. Liu, A. Teke, M. Reshchikov, S. Doğan, V. Avrutin, S.-J. Cho and H. Morkoc, *Journal of applied physics*, 2005, **98**, 041301.
37. M. Willander, O. Nur, Q. Zhao, L. Yang, M. Lorenz, B. Cao, J. Z. Pérez, C. Czekalla, G. Zimmermann and M. Grundmann, *Nanotechnology*, 2009, **20**, 332001.
38. N. P. Herring, K. AbouZeid, M. B. Mohamed, J. Pinsk and M. S. El-Shall, *Langmuir*, 2011, **27**, 15146-15154.
39. W. Lu, S. Gao and J. Wang, *The Journal of Physical Chemistry C*, 2008, **112**, 16792-16800.
40. C. Cheng, B. Yan, S. M. Wong, X. Li, W. Zhou, T. Yu, Z. Shen, H. Yu and H. J. Fan, *ACS applied materials & interfaces*, 2010, **2**, 1824-1828.
41. H. Chen, W. Li, H. Liu and L. Zhu, *Electrochemistry Communications*, 2011, **13**, 331-334.
42. W. Lee, S. K. Min, V. Dhas, S. B. Ogale and S.-H. Han, *Electrochemistry Communications*, 2009, **11**, 103-106.
43. Y. Yue, Z.-A. Qiao, X. Li, A. J. Binder, E. Formo, Z. Pan, C. Tian, Z. Bi and S. Dai, *Crystal Growth & Design*, 2013, **13**, 1002-1005.
44. Y. Abdollahian, J. L. Hauser, I. R. Colinas, C. Agustin, A. S. Ichimura and S. R. J. Oliver, *Crystal Growth & Design*, 2014, **14**, 1506-1509.
45. Y. Liu, S. Li, X. Zhang, H. Liu, J. Qiu, Y. Li and K. L. Yeung, *Inorganic Chemistry Communications*, 2014, **48**, 77-80.
46. Y. Yue, B. Guo, Z.-A. Qiao, P. F. Fulvio, J. Chen, A. J. Binder, C. Tian and S. Dai, *Microporous and Mesoporous Materials*, 2014, **198**, 139-143.
47. E. Zanchetta, L. Malfatti, R. Ricco, M. J. Styles, F. Lisi, C. J. Coghlan, C. J. Doonan, A. J. Hill, G. Brusatin and P. Falcaro, *Chemistry of Materials*, 2014.
48. M. Drobek, M. Bechelany, C. Vallicari, A. Abou Chaaya, C. Charmette, C. Salvador-Levehang, P. Miele and A. Julbe, *Journal of Membrane Science*, 2015, **475**, 39-46.
49. M. Lanchas, S. Arcediano, A. T. Aguayo, G. Beobide, O. Castillo, J. Cepeda, D. Vallejo-Sánchez and A. Luque, *RSC Advances*, 2014, **4**, 60409-60412.
50. J.-B. Lin, R.-B. Lin, X.-N. Cheng, J.-P. Zhang and X.-M. Chen, *Chemical Communications*, 2011, **47**, 9185-9187.
51. M. Lanchas, D. Vallejo-Sanchez, G. Beobide, O. Castillo, A. T. Aguayo, A. Luque and P. Roman, *Chemical Communications*, 2012, **48**, 9930-9932.
52. I. Stassen, N. Campagnol, J. Fransaer, P. Vereecken, D. De Vos and R. Ameloot, *CrystEngComm*, 2013, **15**, 9308-9311.

53. L. H. Wee, N. Janssens, S. P. Sree, C. Wiktor, E. Gobechiya, R. A. Fischer, C. E. A. Kirschhock and J. A. Martens, *Nanoscale*, 2014, **6**, 2056-2060.
54. T. T. Isimjan, H. Kazemian, S. Rohani and A. K. Ray, *J Mater Chem*, 2010, **20**, 10241-10245.
55. F. M. Hinterholzinger, A. Ranft, J. M. Feckl, B. Ruhle, T. Bein and B. V. Lotsch, *Journal of Materials Chemistry*, 2012, **22**, 10356-10362.
56. J. Martín-Ramos, A. Cambeses, A. López-Galindo, J. Scarrow and J. Díaz-Hernández, *Pathways for quantitative analysis by X-Ray diffraction*, INTECH Open Access Publisher, 2012.
57. M. Skompska and K. Zarębska, *Electrochimica Acta*, 2014, **127**, 467-488.
58. M. R. Khajavi, D. J. Blackwood, G. Cabanero and R. Tena-Zaera, *Electrochimica Acta*, 2012, **69**, 181-189.
59. I. Y. Y. Bu, *Ceramics International*, 2014, **40**, 6345-6350.
60. J. Cui, *The Journal of Physical Chemistry C*, 2008, **112**, 10385-10388.
61. S. Baruah and J. Dutta, *Journal of Crystal Growth*, 2009, **311**, 2549-2554.
62. A. Sugunan, H. Warad, M. Boman and J. Dutta, *J Sol-Gel Sci Technol*, 2006, **39**, 49-56.
63. L. Vayssieres, *Advanced materials*, 2003, **15**, 464-466.
64. M. N. R. Ashfold, R. P. Doherty, N. G. Ndifor-Angwafor, D. J. Riley and Y. Sun, *Thin Solid Films*, 2007, **515**, 8679-8683.
65. K. Govender, D. S. Boyle, P. B. Kenway and P. O'Brien, *J Mater Chem*, 2004, **14**, 2575-2591.
66. S. Baruah and J. Dutta, *Science and Technology of Advanced Materials*, 2009, **10**, 013001.
67. X. Gao, X. Li and W. Yu, *The Journal of Physical Chemistry B*, 2005, **109**, 1155-1161.
68. F. Xu, Y. Lu, Y. Xie and Y. Liu, *J Solid State Electrochem*, 2010, **14**, 63-70.
69. Y. H. Ko, M. S. Kim and J. S. Yu, *Applied Surface Science*, 2012, **259**, 99-104.
70. T. Son, L. Top, N. Tri, H. Nhan, L. Vinh, B. Phan, S. Kim and L. Hieu, *Met. Mater. Int.*, 2014, **20**, 337-342.
71. Y. Lin, J. Yang and X. Zhou, *Applied Surface Science*, 2011, **258**, 1491-1494.
72. A. Arslan, E. Hür, S. Ilican, Y. Caglar and M. Caglar, *Spectrochimica Acta Part A: Molecular and Biomolecular Spectroscopy*, 2014, **128**, 716-723.
73. F. Xu, Y. Lu, L. Xia, Y. Xie, M. Dai and Y. Liu, *Materials Research Bulletin*, 2009, **44**, 1700-1708.
74. J. Cravillon, C. A. Schroder, H. Bux, A. Rothkirch, J. Caro and M. Wiebcke, *CrystEngComm*, 2012, **14**, 492-498.
75. P. Y. Moh, M. Brenda, M. W. Anderson and M. P. Attfield, *CrystEngComm*, 2013, **15**, 9672-9678.
76. J. Cravillon, R. Nayuk, S. Springer, A. Feldhoff, K. Huber and M. Wiebcke, *Chemistry of Materials*, 2011, **23**, 2130-2141.
77. J. Reboul, S. Furukawa, N. Horike, M. Tsotsalas, K. Hirai, H. Uehara, M. Kondo, N. Louvain, O. Sakata and S. Kitagawa, *Nature materials*, 2012, **11**, 717-723.
78. E. Ruiz-Agudo, C. V. Putnis and A. Putnis, *Chemical Geology*, 2014, **383**, 132-146.
79. K. Okada, R. Ricco, Y. Tokudome, M. J. Styles, A. J. Hill, M. Takahashi and P. Falcaro, *Advanced Functional Materials*, 2014, **24**, 1969-1977.
80. P. Y. Moh, P. Cubillas, M. W. Anderson and M. P. Attfield, *Journal of the American Chemical Society*, 2011, **133**, 13304-13307.
81. S. Li, W. Shi, G. Lu, S. Li, S. C. J. Loo and F. Huo, *Advanced materials*, 2012, **24**, 5954-5958.

3 Templated Synthesis of Praseodymium and Cerium Oxides

A manuscript under preparation

3.1 Introduction

Polymers of intrinsic microporosity (PIMs) are polymers that are unable to reside in a close-packed conformation. Most polymers posses a high degree of conformational freedom owing to their flexible polymer backbone. This allows them to pack tightly in order to maximize favourable interactions. PIMs possesss a polymer backbone with ridgid constituents, forcing them into a more 'awkward' conformation. Unable to pack tightly, space is created within the polymer, allowing for the existence of microporosity which results in a high surface area [1]. Combining the properties of organic polymers, such as solubility and ease of membrane casting with the existence of microporosity, PIMs have been investigated in areas such as separation [2, 3], gas storage [4, 5], sensing [6] and even as diodes [7]. Furthermore, they have been used as binding sites during the electrochemical deposition of paladium, resulting in the formation of lammella structures. Combined with a carbon-based structure, these materials are interesting candidates for the formation of nanostructured films through thermal methods, yet as far as the authors know, this has never been attempted before.

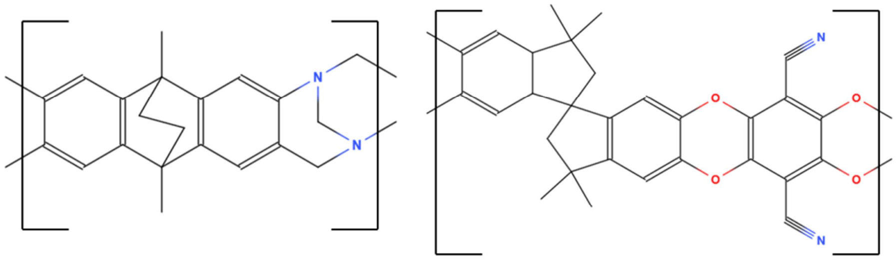

PIM-EA-TB PIM-1

Figure 3.1. Chemical structures of PIM-EA-TB and PIM-1.

Lanthanide oxides are a versatile group of compounds with potential aplications in electronics[8], catalysis[9, 10] and recently in the synthesis of metal-organic frameworks[11, 12]. Of the lanthanide oxides, praseodymium oxide has attracted increasing interest due to its favourable properties. The ability of praseodymium to exist in multiple oxidation states and hence to form different oxides has led to its traditional use as a car exhaust catalyst [13]. It also possesses an unually high conductivity, high dielectric constant, and high electron affinity[14-16]. Such interesting properties have led to of the application of praseodymium oxide in the areas of catalysis [17-21], high k-dielectrics [22-24], electrochemical sensing [25-27] and energy storage [28]. Even though it is known that the morphology of praseodymium oxide can alter its properties [14], very few morphologies of praseodymium oxide such as a homogenous thin films [25, 29], nanorods and cylinders [30-32] and nanoparticles [33] are known. The use of PIMs as templating materials allows for the formation of novel nanostructures of praseodymium oxide.

In this study two PIMs, given in Figure 3.1, were used as templates for the synthesis of praseodymium and cerium oxides on indium doped tin oxides electrodes based on the thermal oxidation approach. The use of thermal oxidation as synthesis method means both the formation of the oxide as well as the removal of the PIM in one step. This allows quick formation of the pure oxide layers. Published recently by McKeown *et.al.* PIM-EA-TB is known for both its unuasually high surface area (1028 $m^2 g^{-1}$) as well as remarkable gas selectivity, making it a very promising material for different applications such as mebrane seperation [34]. PIM-1 posseses a moderately high surface area (800 $m^2 g^{-1}$), flueorescent properties and good solubility [35]. The morphology, oxidation state and the electrochemical properties of the praseodymium oxide prepared were examined to gain more insight into the effects of synthesis conditions as well as the properties of the product. . Furthermore, to highlight the versatility of this method, cerium oxide was also synthesised using the same approach.

3.2 Experimental

3.2.1 Chemicals and Materials

Praseodymium nitrate hexahydrate, cerium nitrate hexahydrate, *N,N*-dimethylformamide (DMF) and chloroform were obtained from Sigma-Aldrich and used without further purification. Polymers with intrinsic microporosity PIM-EA-TB and PIM-1 were kindly donated by the group of Prof. Niel McKeown of the school of Chemistry at the university of Edinburgh. Indium-doped tin oxide glass plates (ITO) with a resistivity of 15 Ω/sq were obtained from Image Optics Components Ltd. The saturated calomel reference electrode was obtained from Radiometer.

3.2.2 Instrumentation

The morphology of the samples was analysed using a JEOL FESEM6301F field emission scanning electron microscopy (FE-SEM). Raman spectroscopy was performed using a Renishaw inVia system. XPS experiments were conducted using a Thermo K Alpha (Thermo Scientific) spectrometer (operating at $\approx 10^{-8} - 10^{-9}$ Torr) with a 180° double focusing hemispherical analyser running in constant analyzer energy (CAE) mode and a 128-channel detector. A monochromated Al Kα radiation source (1486.7 eV) was used. Peak fitting was conducted using XPS Peak Fit (v. 4.1) software using Shirley background subtraction. Peaks were referenced to the adventitious carbon C1s peak (284.6 eV) and peak areas were normalized to the photoelectron cross-section of the F1s photoelectron signal using atomic sensitivity factors[36]. An Elite Thermal Systems Ltd. tube furnace was used to remove the possible organic contamination on the ITO electrodes and for calcination of metal oxides. Electrochemical testing was performed using an Ecochemie Autolab PGSTAT12 potentiostat system.

3.2.3 Procedures and Methods

3.2.3.1 Formation of Metal Oxides

ITO plates were cut into 1 x 3 cm strips and cleaned by rinsing with water and ethanol, followed by calcination at 500 ^{o}C for one hour to remove possible organic contaminations. A solution of 1 mg/ml PIM in chloroform was mixed with a volumetrically equal amount of praseodymium or cerium nitrate solution of varying concentrations in DMF. From the resulting mixture, 25 µL was deposited onto a clean ITO plate and dried in an oven at 100 ^{o}C for 15 min. This deposition process was repeated for a desired number of cycles and finally followed by calcination in a stagnant air oven at 500 ^{o}C for 1 hour.

3.2.3.2 Electrochemical Testing

For electrochemical testing, a three-electrode setup was used, comprising of an saturated calomel reference electrode(SCE), platinum wire counter electrode and ITO working electrode. The electrolyte solution consisted of 0.1 M KNO_3 in double distilled water. Before testing, the electrolyte solution was purged with argon for 10 minutes to remove any dissolved oxygen.

3.3 Results and Discussion

3.3.1 Formation of Praseodymium Oxide

Praseodymium can exist in both the (III) and (IV) oxidation state with the corresponding oxides being the hexagonal Pr_2O_3 and fluorite structured PrO_2 [16], respectively. Between these so-called stoichiometric phases exist the oxygen-deficient phases, corresponding to praseodymium oxidation states between (III) and (IV). These phases also have a fluorite crystal structure and the general formula of Pr_nO_{2n-2}. The existence of these phases has an effect on both the structural as well as electrochemical properties of the oxide. Each phase is stable at a different temperature and the oxygen partial pressure. These conditions dictate which phases are formed and changing them results in changes in the oxide phase present. Surprisingly, it is not a stoichiometric phase but one of the oxygen deficient phases (Pr_6O_{11}) that is stable in ambient conditions.

The formation of praseodymium oxide can be carried out in a variety of ways. Chemical vapour deposition mostly deals with the formation of flat, non-structured films intended for use in electronics [15, 37]. Formation of praseodymium oxide *via* wet chemical methods relies on an increase of the pH by addition of a base to form praseodymium hydroxide ($Pr(OH)_3$). The oxide is then obtained through a calcination step at elevated temperatures (500 ^{o}C) [30, 38]. Finally, direct thermal oxidation of a praseodymium-containing compound is also possible and unlike the previously mentioned methods, it allows for a one-step formation of the oxide without the need for specialized equipment [39, 40].

The products obtained through thermal oxidation depend on both the precursor as well as oxidation conditions such as temperature and oxygen partial pressure [41]. Investigation into the thermal oxidation of pure praseodymium nitrate has demonstrated that Pr_6O_{11} can be formed at temperatures higher than 465 ^{o}C [42]. However, the presence of carbon can lead to different calcination behaviour. Bäumer *et al.* investigated the formation of nanostructured praseodymium through thermal oxidation using praseodymium nitrate with and without carbon-based templates [21]. By comparing different methods they found that the ratio of carbon-based template to praseodymium nitrate salt decide not only at which temperature a pure oxide was formed but also the phase of this oxide. Whereas pure praseodymium nitrate always resulted in the formation of Pr_6O_{11}, the use of a carbon template results in the formation of the monoclinic $Pr_2O_3CO_3$ at lower temperatures and in some cases Pr_2O was formed alongside the expected Pr_6O_{11}. The morphologies of the oxides formed based on carbon-based templates were not yet examined.

The use of PIMs offers the possibility of forming a structured oxide in one step, yet it also adds an extra dimension to the synthesis. The formation of multiple oxides as well as the formation of $Pr_2O_3CO_3$ are possible. It is therefore important to examine the purity and oxidation state of the product. XPS was used to assess the composition of the product as well as the identity of the oxide formed. Raman spectroscopy was used to assess if $Pr_2O_3CO_3$ was formed. The morphology of the samples was examined using FE-SEM and finally, the electrochemical properties were obtained using cyclic voltammetry.

3.3.1.1 Composition

Preaseodymium oxide was formed using two different PIMs as templates. To assess whether $Pr_2O_3CO_3$ was formed, the praseodymium oxide films were examined using XPS and Raman spectroscopy (See Figure 3.2). The XPS survey scan shows a small peak for carbon when using both PIM-EA-TB as well as the PIM-1. These could indicate the presence of $Pr_2O_3CO_3$, however lanthanide oxides are known to have a high electronegativity, allowing the oxygen terminated surface to adsorb CO_2 very easily from the atmosphere [43]. Even though very little research has been performed regarding the Raman spectra of praseodymium oxide, Popa *et al.* have shown that the presence of $Pr_2O_3CO_3$ results in a sharp peak at around a Raman shift of 367 cm^{-1} [44]. A peak between 340 and 395 cm^{-1} is expected for Pr_2O_3, with a broadening of the band being related to the existence of praseodymium atoms in both oxidation states. The lack of a peak at 367 cm^{-1} and the existence of a wide peak around 390 cm^{-1} show that pure praseodymium oxide was formed.

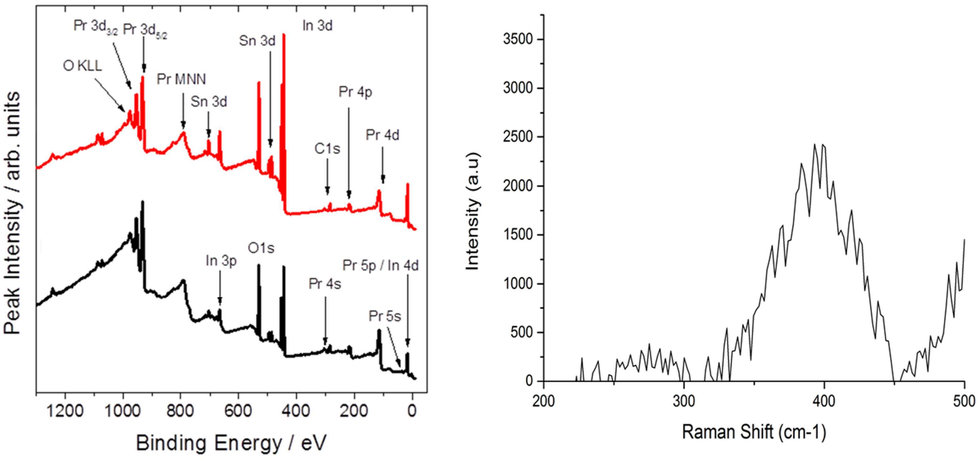

Figure 3.2. XPS survey scan showing the composition of the formed films PIM-1 (red) and PIM-EA-TB (black) after 10 deposition cycles(left) and Raman spectrum of oxide obtained using PIM-EA-TB after 10 deposition cycles (right).

3.3.1.2 Effect of Mass Ratios

After ensuring that only pure praseodymium oxide was formed, the structure of this oxide was examined using different of praseodymium nitrate-to-PIM mass rations. PIM-EA-TB was used as it is more porous and has a higher surface area. All samples have undergone 10 deposition cycles before oxide formation.

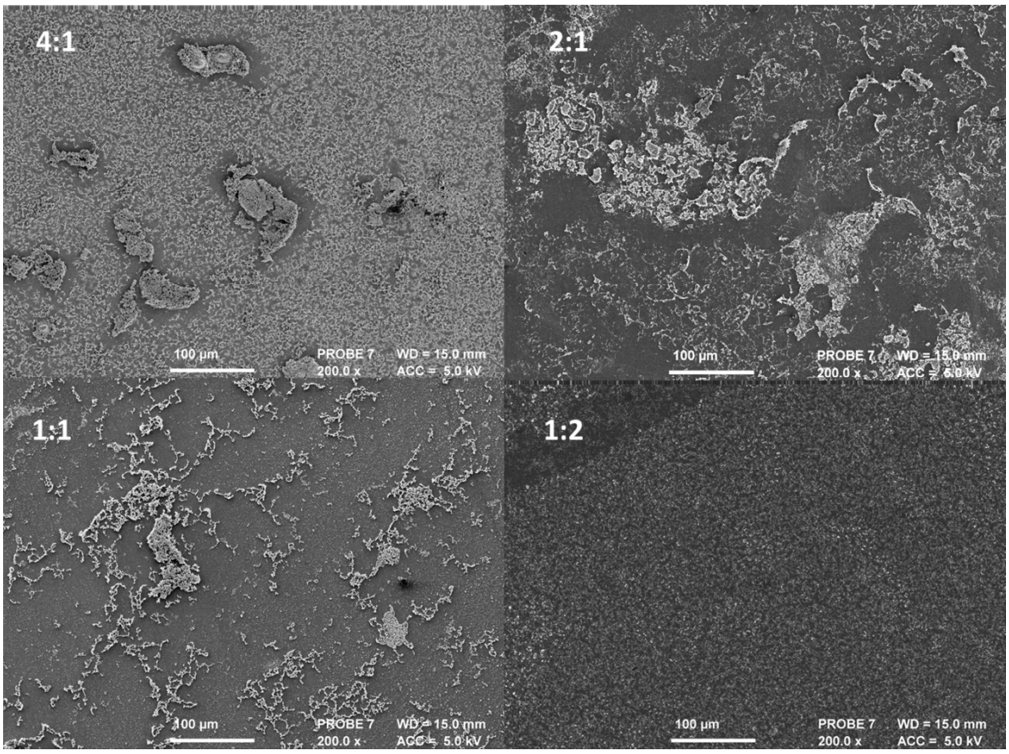

Figure 3.3. SEM images showing the effect of PIM-to-praseodymium-mass-ratio after 10 deposition cycles.

Figure 3.3 illustrates how both the thickness and the coverage of the layer depend on the ratio of praseodymium to PIM. At the lowest ratio (1:2), one can see that the coverage is uniform and results in the formation of very small size structures. Increasing the ratio to 1:1 results in the formation of big clusters on an otherwise bare ITO surface. At a ratio of 2:1, smaller structures grow around these big clusters and finally at a ratio of 4:1, these small structures surround the large clusters and cover the entire ITO surface.

A more detailed view of the resulting structures is shown Figure 3.4. As can be seen, in all but the lowest ratio an oxide structure with a distinct, porous morphology is formed. The structure consists of spheres, connected by tubes whose size and density increase with increasing praseodymium content.

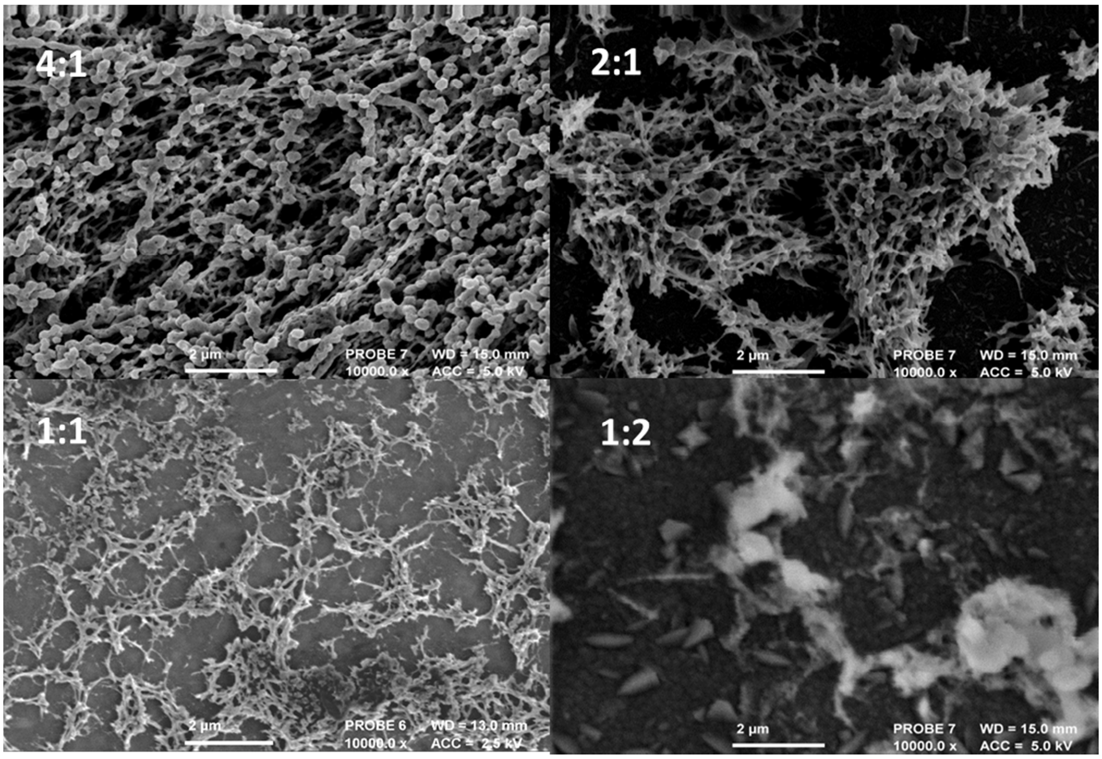

Figure 3.4. SEM images showing the effect of PIM-to-praseodymium-mass-ratio after 10 deposition cycles.

Figure 3.5 gives a more detailed picture of the morphologies obtained with mass ratios of 4:1 and 1:1. As can be seen, the structures increase in size with increasing amount of praseodymium nitrate used. However, it is interesting to note that while at a mass ratio of 1:1, the structures appear hollow and fine, this is no longer the case at a mass ratio of 4:1. It is suspected that at higher mass ratios, agglomeration takes place, resulting in the formation of a coarser structure (See Figure 3.6).

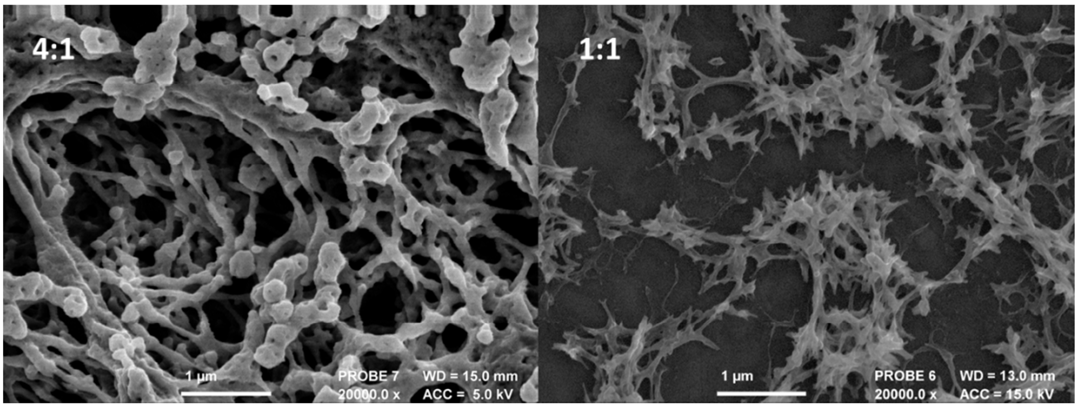

Figure 3.5. More detailed SEM image of the 4:1 and 1:1 mass ratios after 10 deposition cycles.

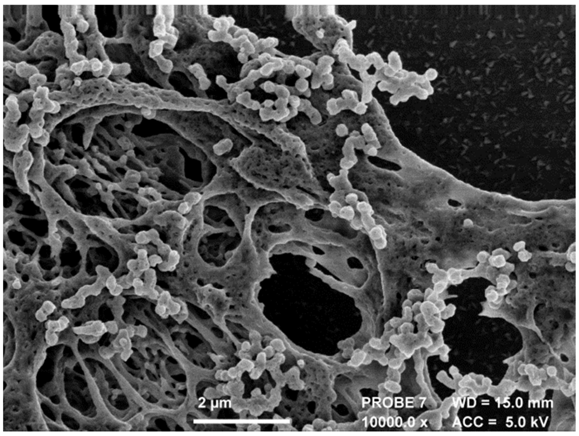

Figure 3.6. SEM image showing the loss of fine structure due to agglomeration at a mass ratio of 4:1.

3.3.1.3 The Effect of Deposition Cycles

Whereas increasing the ratio of praseodymium to PIM resulted in an increase in coverage, the delicate structure of the oxide was partially lost. It was therefore interesting to see if an increase in deposition cycles would give the same result. The effect of the number of deposition cycles was investigated using a mixture with a praseodymium nitrate-to-PIM mass ratio of 1:1. Figure 3.7 shows that increasing the deposition cycles from 10 to 20 results in the formation of larger clusters. Unlike when increasing the mass ratio however, this does not lead to the formation of coarser structures, allowing the fine hollow-like morphology to be maintained.

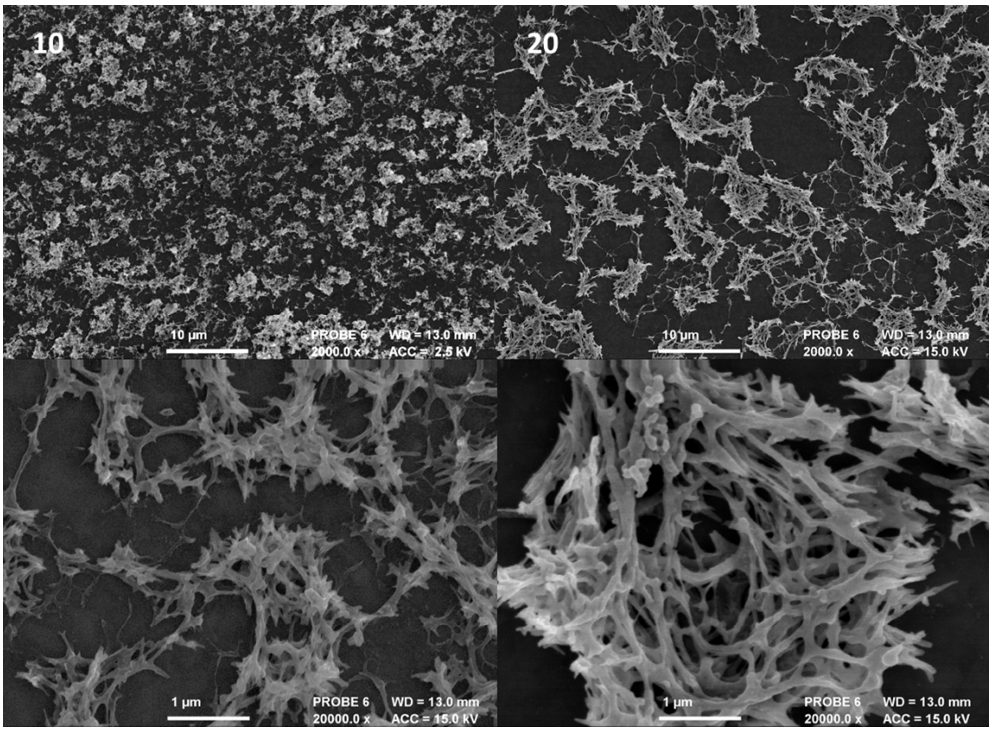

Figure 3.7. SEM images showing the effect of the number of deposition cycles on the coverage (upper) and structure (lower) of the formed oxide. PIM-EA-TB was used with a mass ratio of 1:1.

However, an increase of the praseodymium nitrate-to-PIM-ratio as well as the amount of deposition cycles result in a decreased attachment to the ITO surface as evident in Figure 3.8.

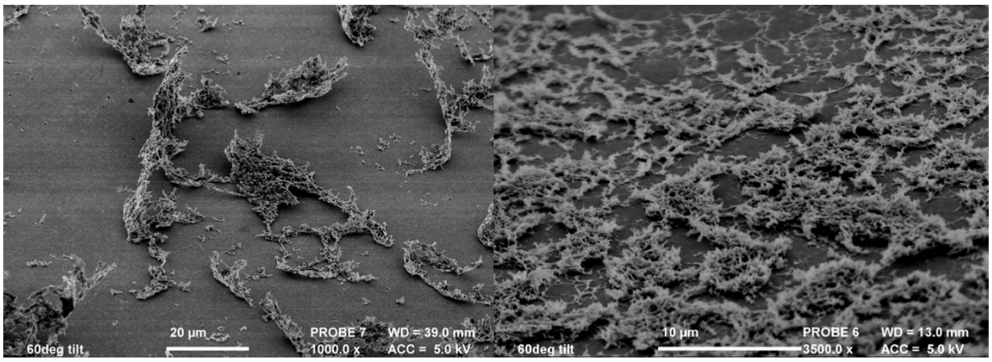

Figure 3.8. SEM images at a 60 ˚ tilt showing peeling of the layer at a 4:1 mass ratio (left) and 20 deposition cycles (right).

3.3.1.4 The Effect of a Different PIM

To ascertain whether the structure of the oxide is due to the choice of polymer, PIM-1 was used as a templating agent. The differences in coverage and structure are given in Figure 3.9. The use of PIM-1 results in a more homogenous and denser coverage which can be attributed to the difference in resulting structure. While PIM-EA-TB gives long, branch-like structures, PIM-1 gives more fine, sponge-like structures. These results indicate that the choice of the PIM as a templating agent affects the morphology and thus, the formation of different praseodymium oxide structures.

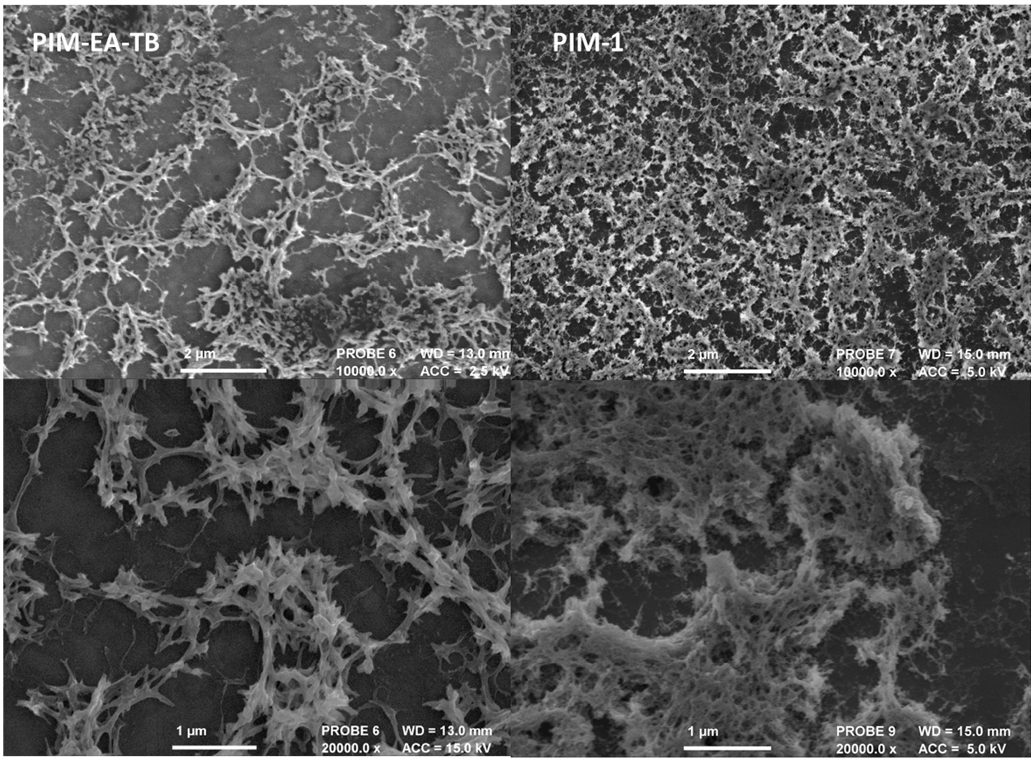

Figure 3.9. SEM images showing the difference in coverage (upper) and structure (lower) between PIM-EA-TB and PIM-1 with a mass ratio of 1:1 and 10 deposition cycles.

To determine the oxidation state of the praseodymium , XPS analysis was performed. The XPS core level and surface spectra for the most important peaks for characterising praseodymium oxide (O1s and $Pr3s_{5/2}$) are given in Figure 3.10.

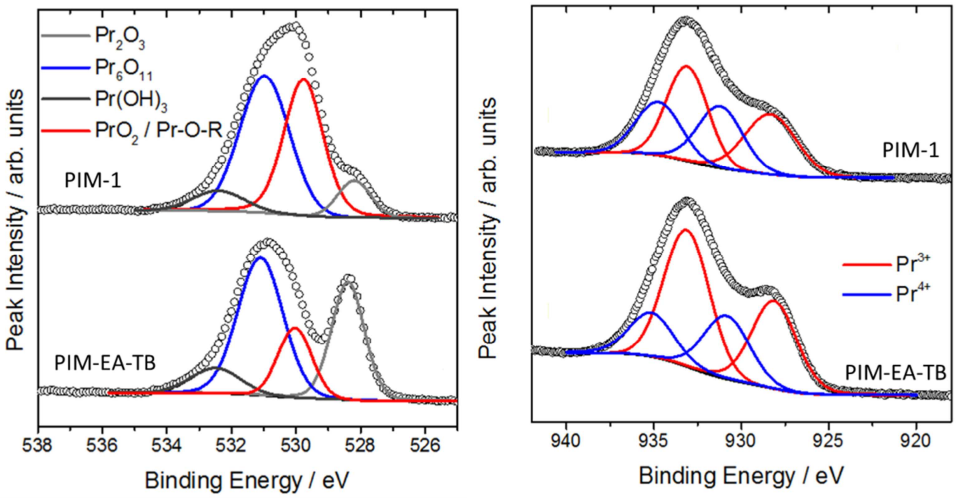

Figure 3.10. XPS core level and survey spectra for O1s (left) and $Pr3d_{5/2}$ (right).

Wolffram *et al.* [45] have studied thin Pr_xO_y films made from Pr_6O_{11} targets and their work is used here as the primary basis for fitting the O1s spectra. Four peaks were required to curve fit the O1s spectra, corresponding to different praseodymium oxide species. The two main components at ≈ 528.5 eV and ≈ 531 eV most likely belong to Pr_2O_3 and Pr_6O_{11} , respectively. Lütkehoff *et al.* [46] indicate that the signal at ≈ 532 eV can be ascribed to Pr-based hydroxides, such as $Pr(OH)_3$, which would be expected from the breakdown of Pr_6O_{11} in the presence of water, eventually leading to PrO_2 formation[45]. The feature at ≈ 529.5 eV could be either indicative of the presence of PrO_2 [47] or be related to surface adsorbates in the form of Pr-O-R [47, 48]; both species have O1s signal known to overlap with the Pr_6O_{11} O1s signal. As seen in Table 3.1, the Pr_6O_{11} and Pr-hydroxide content seems independent of the employed PIM. However, the use of PIM-EA-TB favours the additional formation of Pr_2O_3 (Pr^{3+}), whilst the use of PIM-1 favours the formation of PrO_2 (Pr^{4+}) and surface adsorbates. This could be explained by the finer structure and hence higher surface area formed when using PIM-1.

Table 3.1. Oxygen composition in as-prepared Pr_6O_{11}

	% O1s Composition	
Species	PIM-EA-TB	PIM-1
Pr_2O_3	29.2	8.2
PrO_2 \adsorbates	16.7	39.2
Pr_6O_{11}	45.3	45.8
hydroxides	8.8	6.9

Furthermore, Wolffram *et al.* [45] note that unambiguous fitting of the Pr3d core levels is difficult and remains controversial. Again using the above reference as a model, 4 chemical environment curves were fitted. The line pair at higher binding energy (≈ 931 eV and ≈ 935 eV) is ascribed to

Pr^{4+}species (e.g. Pr_6O_{11} and PrO_2). Assuming that they reflect chemical environments at the surface and are not satellites [46, 48], the line pair at lower binding energy (≈ 928 eV and ≈ 933 eV) originate from Pr^{3+}(e.g. Pr_2O_3 and $Pr(OH)_3$). The ratios of Pr^{3+}: Pr^{4+} species are 2.0 and 1.3 for PIM-EA-TB and PIM-1, respectively. Notwithstanding the different chemical states, the O:Pr ratios are 4.6 and 2.64 for PIM-EA-TB and PIM-1, respectively. These ratios are quite high as the stoichiometric and expected O:Pr ratios for Pr_2O_3 (Pr^{3+}) and Pr_6O_{11} (Pr^{4+}) are 1.5 and 1.8, respectively. This may indicate that the O1s signal is influenced by other sources of oxygen, other than the Pr-oxides (e.g. hydroxides, water, etc.). One expects an O:Pr ratio of less than 2:1 for the Pr-based oxides[48]. It is clear from Table 2 that PIM-EA-TB has a higher Pr^{3+}composition than PIM-1, and *vice versa* in the case of Pr^{4+}species.

Table 3.2. The Pr3d binding energy and corresponding Pr oxidation states

	$Pr3d_{5/2}$ Binding Energy (eV)				**Pr3d composition (%)**	
	928	931	933	935	Pr^{3+}	Pr^{4+}
PIM-EA-TB	27.0	19.2	39.8	14.0	66.8	33.2
PIM-1	25.9	23.1	31.5	19.5	57.4	42.6

3.3.1.5 Electrochemical Testing

The electrochemical properties of the obtained films were analysed using cyclic voltammetry (CV) with the aim of determining the capacitance. The results indicate a higher capacitance for the praseodymium oxide deposited using PIM-1. This could be due to the increased surface coverage or the higher surface area owning to the finer structures. Furthermore, an increase in capacitance is observed when the amount of depositions is increased. However, even with twice as many deposition cycles, the capacitance of the PIM-EA-TB templated oxide still possess a lower capacitance than the PIM-1 templated oxide.

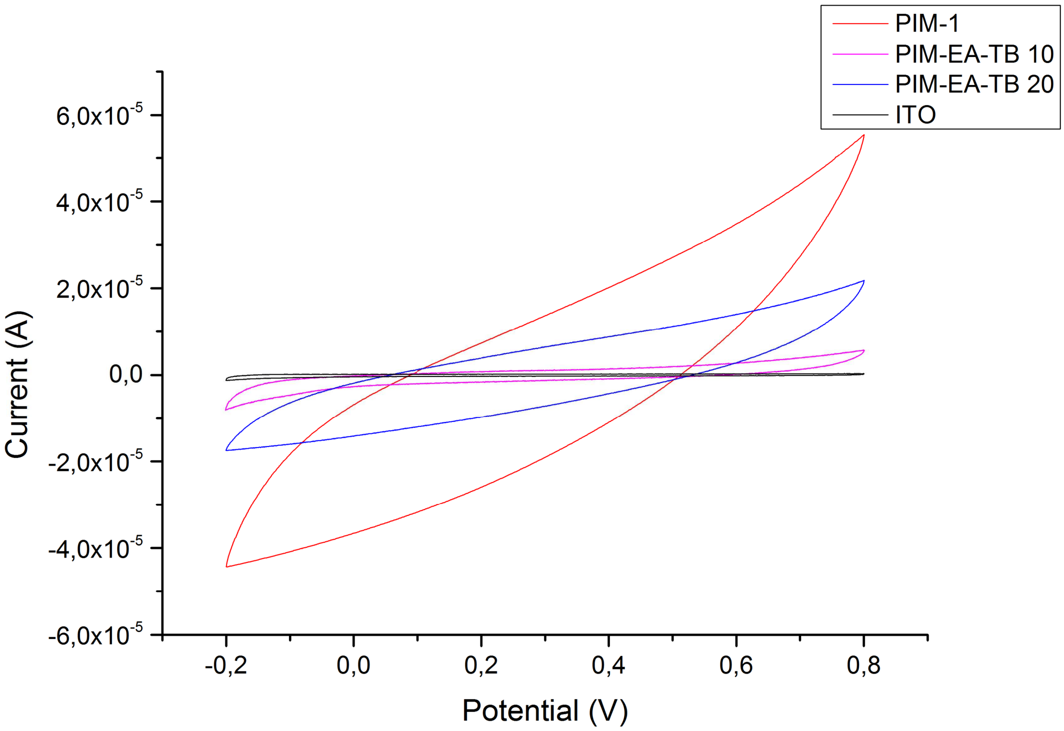

Figure 3.11. CV spectra of the obtained praseodymium oxide oxides. The deposition cycles used are 10 for PIM-1 and 10 and 20 for PIM-EA-TB 10 and PIM-EA-TB 20, respectively. Scan rate was 200 mV/s Applied potential is given versus SCE.

3.3.1.6 The Synthesis of Cerium Oxide

The ability to form other nanostructured metal oxide using PIMs was explored by the formation of cerium oxide. PIM-EA-TB was used as it resulted in the formation of a very characteristic nanostructures for praseodymium oxide. The mass ratio of cerium nitrate to PIM-EA-TB was kept at 1:1, with 10 deposition cycles used. As can be seen in Figure 3.12, the use of cerium results in a lower coverage and the formation of larger clusters similar to those observed when higher praseodymium nitrate-to-PIM mass ratios were used. However, a closer inspection shows that while cerium oxide has a coarser structure, the structures of the two oxides are remarkably similar. These results indicate that the templating effect of the PIM is preserved when different metal oxides are used.

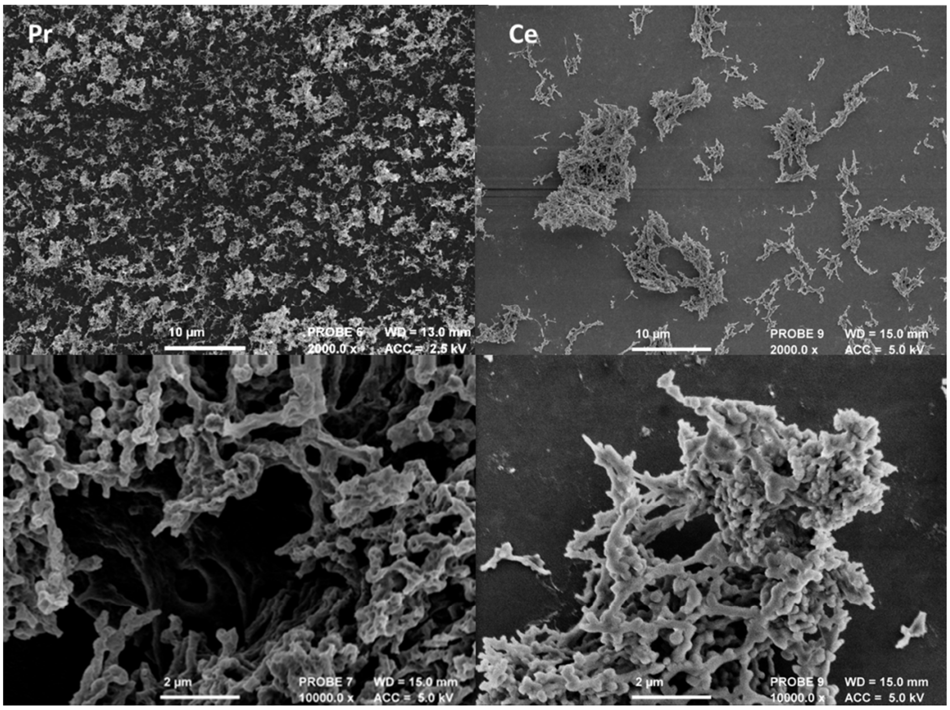

Figure 3.12. SEM images comparing the praseodymium oxide (left) and cerium oxide (right) structures obtained using the same method. PIM-EA-TB was used with a mass ratio of 1:1 for 10 deposition cycles.

3.4 Conclusion and Outlook

Polymers of intrinsic microporosity were used as templates for the synthesis of metal oxides for the first time. The use of these polymers allows for the synthesis of novel structures with a high degree of porosity and a large surface area. The effects of metal salt to polymer mass ratios as well as the amount of deposition cycles were examined. The technique is versatile, allowing the formation of different oxides with the same structure. Furthermore, while deposition here was carried out on ITO surfaces, this can be extend to other substrates. The high surface area of the oxides, coupled with the versatility of this technique make its use in the fields of sensing, electronics and catalysis very attractive.

3.5 References

1. N. B. McKeown and P. M. Budd, *Macromolecules*, 2010, **43**, 5163-5176.
2. P. Gorgojo, S. Karan, H. C. Wong, M. F. Jimenez-Solomon, J. T. Cabral and A. G. Livingston, *Advanced Functional Materials*, 2014, **24**, 4728-4728.
3. S. Kim and Y. M. Lee, *Progress in Polymer Science*.
4. J. Germain, J. M. J. Fréchet and F. Svec, *Small*, 2009, **5**, 1098-1111.
5. Y. Luo and B. Tan, in *Porous Materials for Carbon Dioxide Capture*, eds. A.-H. Lu and S. Dai, Springer Berlin Heidelberg, 2014, pp. 143-180.
6. N. B. McKeown and P. M. Budd, *Chemical Society Reviews*, 2006, **35**, 675-683.
7. E. Madrid, Y. Rong, M. Carta, N. B. McKeown, R. Malpass-Evans, G. A. Attard, T. J. Clarke, S. H. Taylor, Y.-T. Long and F. Marken, *Angewandte Chemie*, 2014, **126**, 10927-10930.
8. R. Gillen and J. Robertson, *Microelectronic Engineering*, 2013, **109**, 72-74.
9. C. M. Lousada, M. Yang, K. Nilsson and M. Jonsson, *Journal of Molecular Catalysis A: Chemical*, 2013, **379**, 178-184.
10. A. Ashcroft, A. Cheetham, J. Foord, M. Green, C. Grey and A. Murrell, 1990.
11. N. Campagnol, E. R. Souza, D. E. De Vos, K. Binnemans and J. Fransaer, *Chemical Communications*, 2014, **50**, 12545-12547.
12. X. Zhang, L. Fan, Z. Sun, W. Zhang, W. Fan, L. Sun and X. Zhao, *CrystEngComm*, 2013, **15**, 4910-4916.
13. T. Bunluesin, R. J. Gorte and G. W. Graham, *Applied Catalysis B: Environmental*, 1997, **14**, 105-115.
14. M. Shamshi Hassan, M. Shaheer Akhtar, K.-B. Shim and O. B. Yang, *Nanoscale Res Lett*, 2010, **5**, 735-740.
15. H. C. Aspinall, J. Gaskell, P. A. Williams, A. C. Jones, P. R. Chalker, P. A. Marshall, J. F. Bickley, L. M. Smith and G. W. Critchlow, *Chemical Vapor Deposition*, 2003, **9**, 235-238.
16. V. Thangadurai, R. Huggins and W. Weppner, *J Solid State Electrochem*, 2001, **5**, 531-537.
17. K. Asami, K.-i. Kusakabe, N. Ashi and Y. Ohtsuka, *Applied Catalysis A: General*, 1997, **156**, 43-56.
18. A. M. Gaffney, C. A. Jones, J. J. Leonard and J. A. Sofranko, *Journal of Catalysis*, 1988, **114**, 422-432.
19. P. X. Huang, F. Wu, B. L. Zhu, G. R. Li, Y. L. Wang, X. P. Gao, H. Y. Zhu, T. Y. Yan, W. P. Huang, S. M. Zhang and D. Y. Song, *The Journal of Physical Chemistry B*, 2006, **110**, 1614-1620.
20. R. J. H. Voorhoeve, J. P. Remeika, P. E. Freeland and B. T. Matthias, *Science*, 1972, **177**, 353-354.
21. Y. Borchert, P. Sonström, M. Wilhelm, H. Borchert and M. Bäumer, *The Journal of Physical Chemistry C*, 2008, **112**, 3054-3063.
22. R. Lo Nigro, R. G. Toro, G. Malandrino, V. Raineri and I. L. Fragalà, *Advanced Materials*, 2003, **15**, 1071-1075.
23. T.-M. Pan, F.-J. Tsai, C.-I. Hsieh and T.-W. Wu, *Electrochemical and solid-state letters*, 2007, **10**, G21-G24.
24. A. Fissel, H. J. Osten and E. Bugiel, *Journal of Vacuum Science & Technology B: Microelectronics and Nanometer Structures*, 2003, **21**, 1765-1772.
25. S. Shrestha, F. Marken, J. Elliott, C. Yeung, C. Mills and S. Tsang, *Journal of the Electrochemical Society*, 2006, **153**, C517-C520.

26. S. Shrestha, C. M. Y. Yeung, C. E. Mills, J. Lewington and S. C. Tsang, *Angewandte Chemie International Edition*, 2007, **46**, 3855-3859.
27. S. Shrestha, C. E. Mills, J. Lewington and S. C. Tsang, *The Journal of Physical Chemistry B*, 2006, **110**, 25633-25637.
28. X. Wang, C. Yang, T. Wang and P. Liu, *Electrochimica Acta*, 2011, **58**, 193-202.
29. S. Shrestha, C. M. Y. Yeung, F. Marken, C. E. Mills and S. C. Tsang, *Sensors and Actuators B: Chemical*, 2007, **123**, 400-406.
30. A. Dodd, *Journal of Colloid and Interface Science*, 2013, **392**, 137-140.
31. N. Krishna Chandar and R. Jayavel, *Materials Research Bulletin*, 2014, **50**, 417-420.
32. S. Shrestha, C. M. Y. Yeung, C. Nunnerley and S. C. Tsang, *Sensors and Actuators A: Physical*, 2007, **136**, 191-198.
33. S. Zinatloo-Ajabshir and M. Salavati-Niasari, *Ceramics International*, 2015, **41**, 567-575.
34. M. Carta, R. Malpass-Evans, M. Croad, Y. Rogan, J. C. Jansen, P. Bernardo, F. Bazzarelli and N. B. McKeown, *Science*, 2013, **339**, 303-307.
35. P. M. Budd, B. S. Ghanem, S. Makhseed, N. B. McKeown, K. J. Msayib and C. E. Tattershall, *Chemical Communications*, 2004, 230-231.
36. C. D. Wagner, L. E. Davis, M. V. Zeller, J. A. Taylor, R. H. Raymond and L. H. Gale, *Surface and Interface Analysis*, 1981, **3**, 211-225.
37. H. C. Aspinall, J. Gaskell, P. A. Williams, A. C. Jones, P. R. Chalker, P. A. Marshall, L. M. Smith and G. W. Critchlow, *Chemical Vapor Deposition*, 2004, **10**, 83-89.
38. L. Ma, W. Chen, J. Zhao, Y. Zheng, X. Li and Z. Xu, *Materials Letters*, 2007, **61**, 1711-1714.
39. B. M. Abu-Zied and S. A. Soliman, *Thermochimica Acta*, 2008, **470**, 91-97.
40. B. A. A. Balboul, *Journal of Analytical and Applied Pyrolysis*, 2010, **88**, 192-198.
41. B. Treu, W. Fahrenholtz and M. O'Keefe, *Inorganic Materials*, 2011, **47**, 974-978.
42. G. A. M. Hussein, B. A. A. Balboul, M. A. A-Warith and A. G. M. Othman, *Thermochimica Acta*, 2001, **369**, 59-66.
43. M. P. Rosynek, *Catalysis Reviews*, 1977, **16**, 111-154.
44. J. M. Calderon Moreno, V. G. Pol, S.-H. Suh and M. Popa, *Inorganic Chemistry*, 2010, **49**, 10067-10073.
45. D. Wolfframm, M. Ratzke, M. Kappa, M. J. Montenegro, M. Döbeli, T. Lippert and J. Reif, *Materials Science and Engineering: B*, 2004, **109**, 24-29.
46. S. Lütkehoff, M. Neumann and A. Ślebarski, *Physical Review B*, 1995, **52**, 13808.
47. M. Sawangphruk and J. S. Foord, *Diamond and Related Materials*, 2010, **19**, 885-888.
48. D. Wolfframm, M. Ratzke, M. Kappa, M. Montenegro, M. Döbeli, T. Lippert and J. Reif, *Materials Science and Engineering: B*, 2004, **109**, 24-29.

Appendix A

A.1 Evaluation of Crater Morphology with Reaction Time

When using a preheated aluminum heating block for the synthesis of ZIF-8 on zinc oxide, a crater-like morphology was observed. The evolution of this morphology with reaction time is given using two different magnifications.

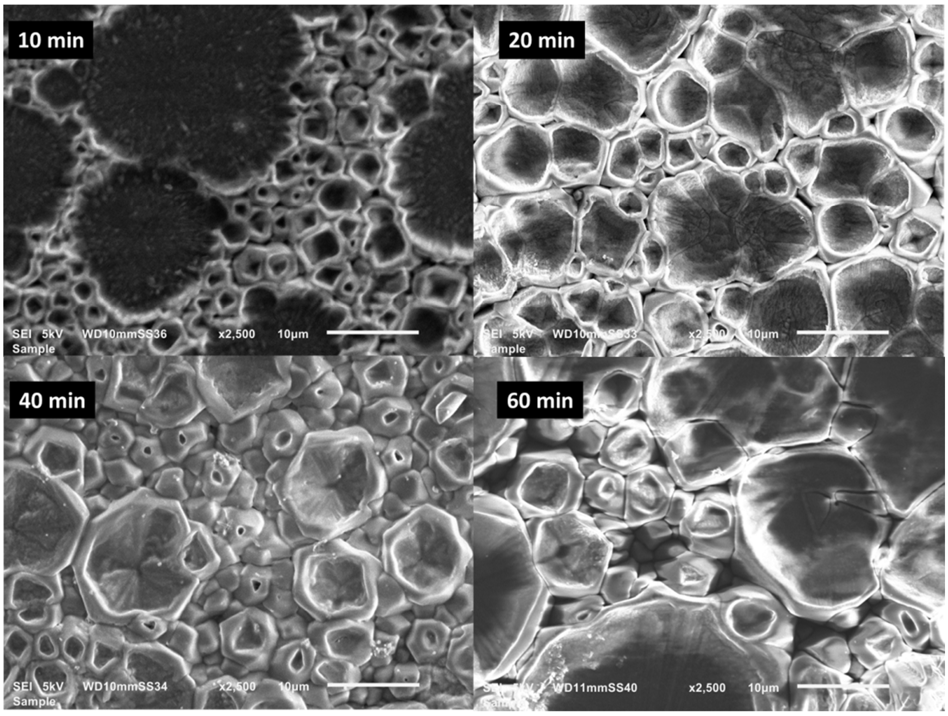

A1 SEM images showing the evolution of ZIF-8 with crater-like morphology with time as 2500x magnification. Pure linker was used

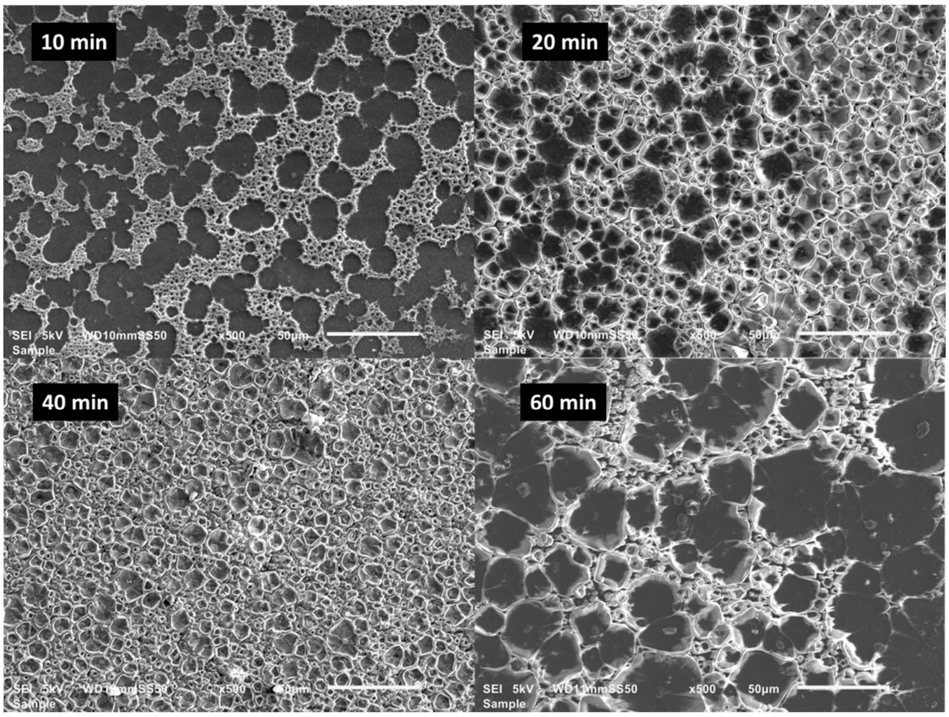

A2 SEM images showing the evolution of ZIF-8 with crater-like morphology with time as 500x magnification. Pure linker was used

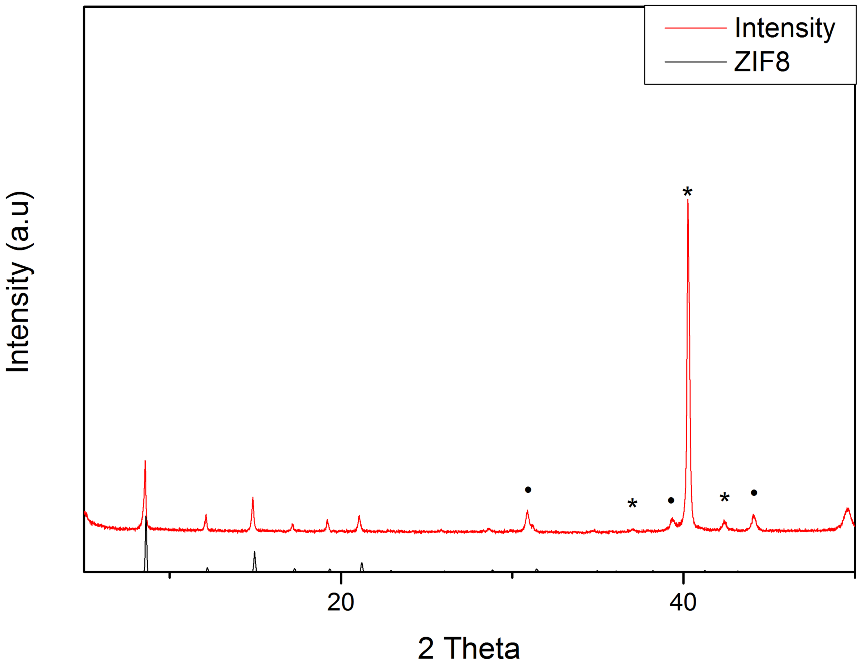

A3. XRD spectrum of crater-like ZIF-8 formed using a pre-heated heating block (fast) after 60 minutes reaction time compared to known ZIF-8 peaks (ZIF8). Pure linker powder was used

Appendix B

B.1 Formation of praseodymium oxide without PIM

As a blank, praseodymium synthesis was carried out without the use of a PIM. A mixture of 1 mg/ml praseodymium nitrate in DMF and pure chloroform without PIM was used. The amount of deposition cycles was 10 and thermal oxidation conditions were the same as used before.

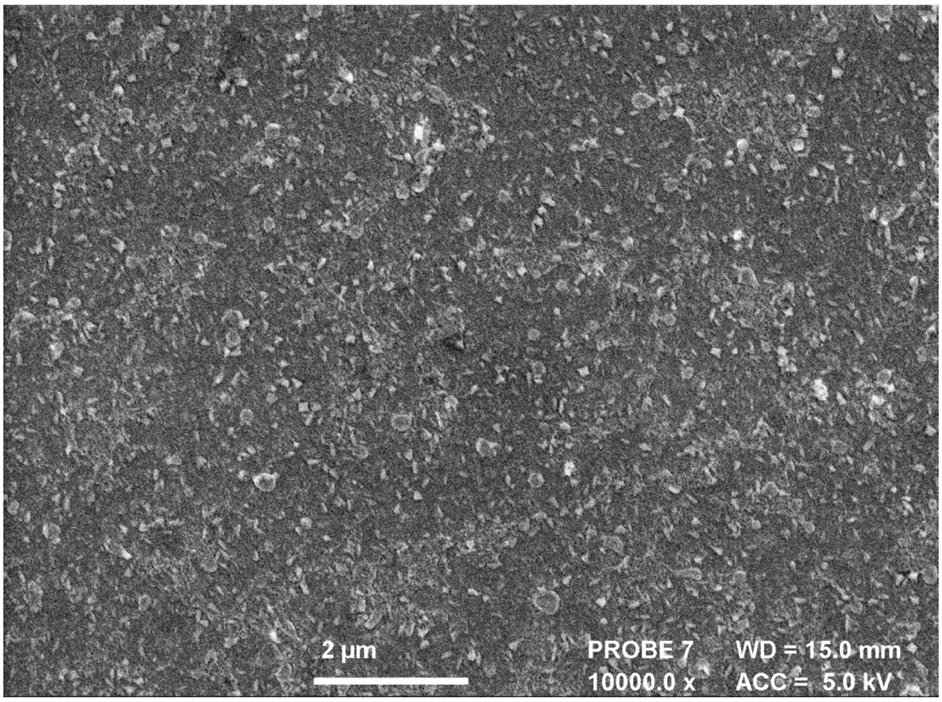

Figure B1 SEM image of praseodymium formation without PIM

B. 2 XRD Spectra of Praseodymium Oxide

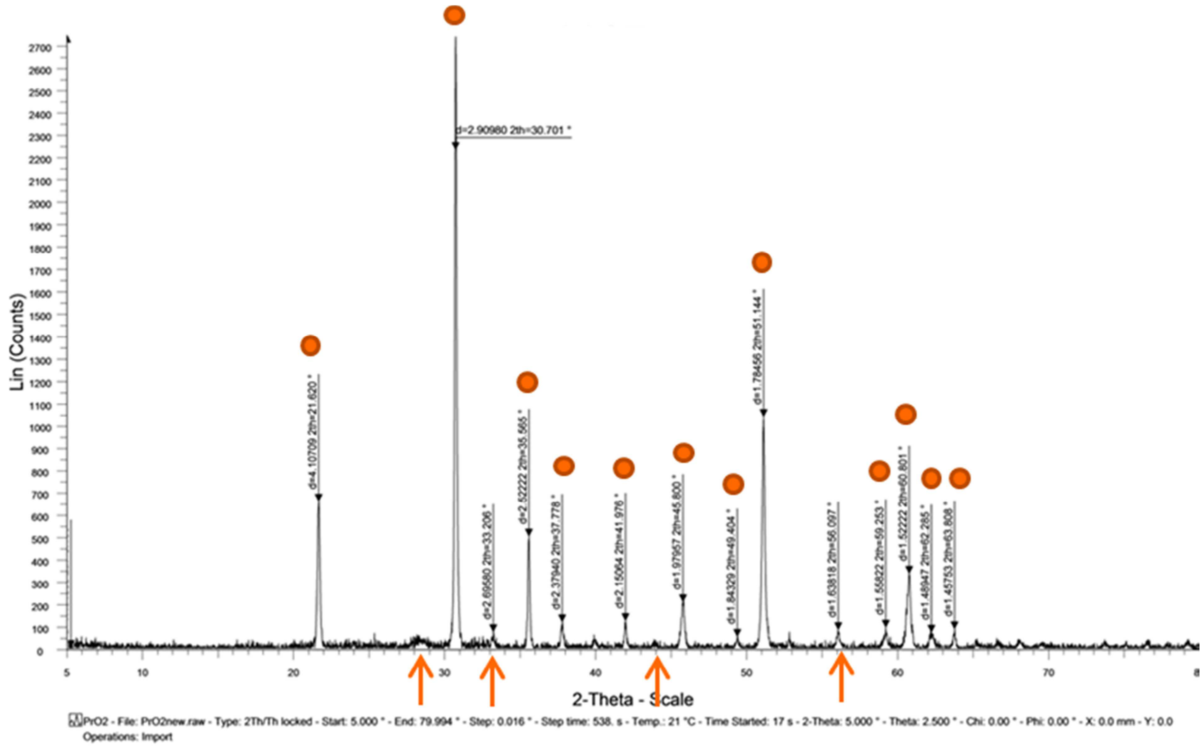

B2. XRD spectrum for praseodymium oxide formed using PIM-EA-TB with a mass ratio of 1:1 and 20 deposition cycles. The circles represent ITO peaks, while the arrows are correspond to Pr_6O_{11} peaks

B.3 EDX Spectra of Praseodymium Oxide

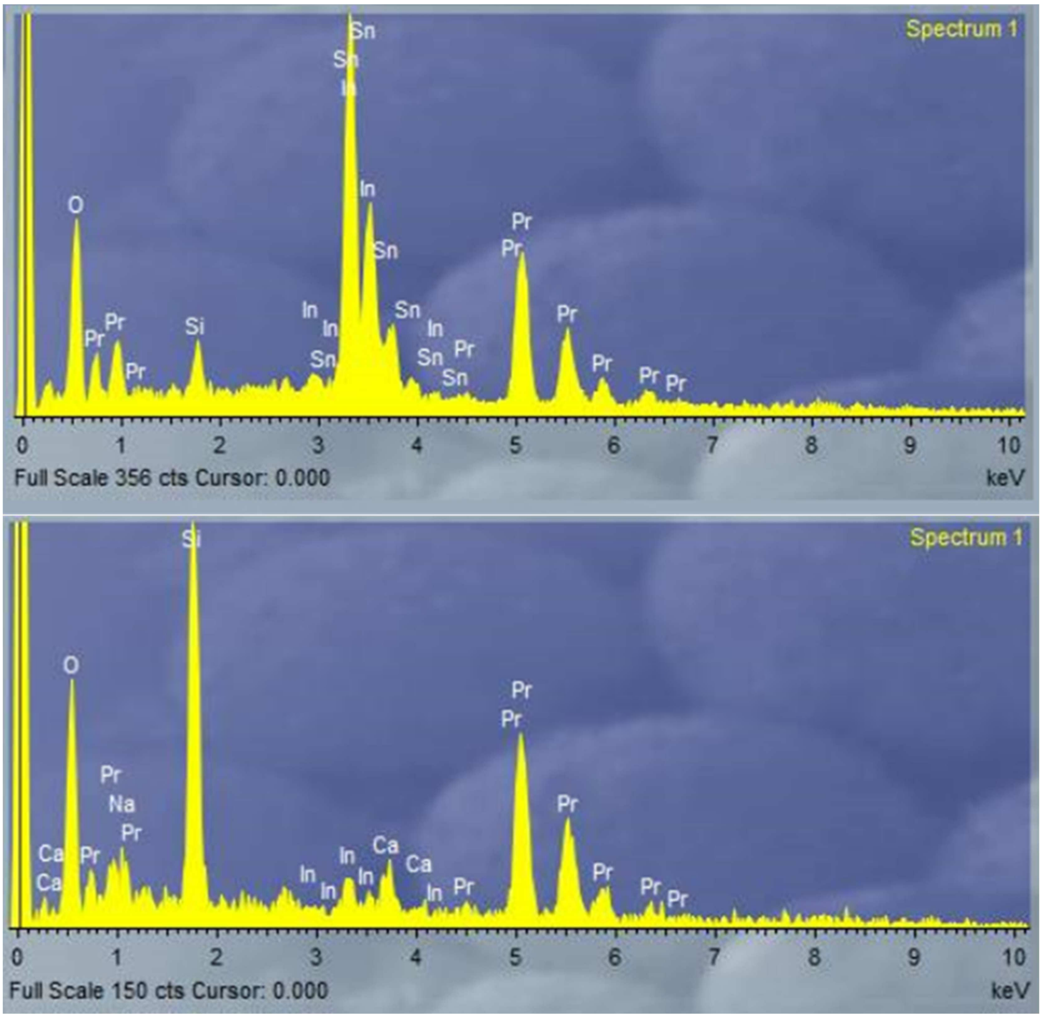

A.

B3. EDX spectra of praseodymium oxide films formed using PIM-EA-TB with a mass ratio of 1:1. Deposition cycles were 10 (above) and 20 (below)

B.4 CVs at Different Scan Rates and Normalized CVs

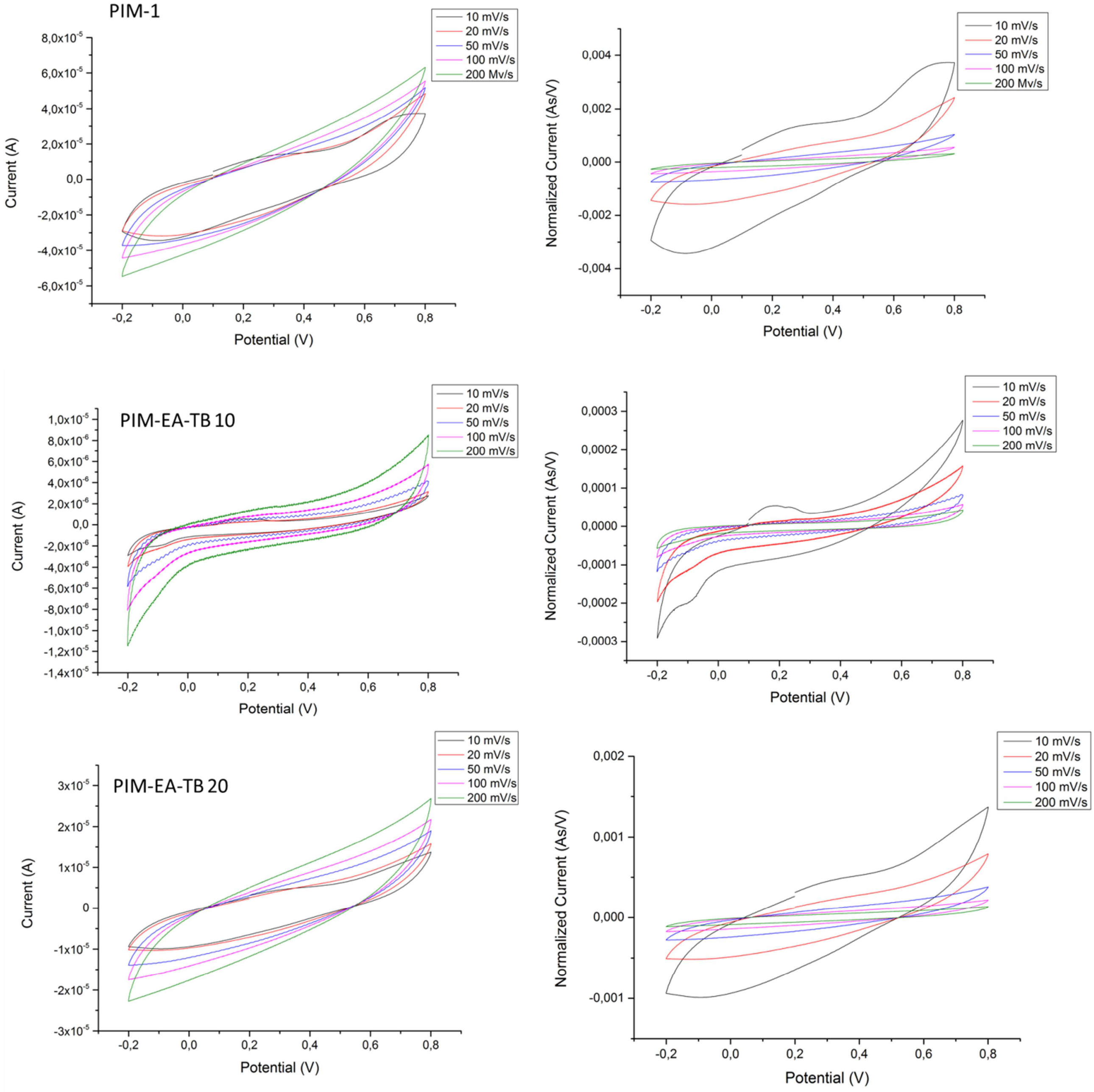

B4.CVs (left) and normalized CVs (right) of PIM-1 after 10 depositions, PIM-EA-TB after 10 and 20 depositions

The normalized CVs were obtained by dividing the current (A) by the scan rate (V/s)